frontiers | Frontiers in Earth Science

TYPE Original Research
PUBLISHED 04 January 2023
DOI 10.3389/feart.2022.1073075

OPEN ACCESS

EDITED BY
Benedict Reinardy,
Royal Institute of Technology, Sweden

REVIEWED BY
Daniel Nývlt,
Masaryk University, Czechia
Yuribia Munoz,
University of Houston, United States

*CORRESPONDENCE
Stephen J. Roberts,
sjro@bas.ac.uk

SPECIALTY SECTION
This article was submitted to Quaternary Science, Geomorphology and Paleoenvironment, a section of the journal Frontiers in Earth Science

RECEIVED 18 October 2022
ACCEPTED 06 December 2022
PUBLISHED 04 January 2023

CITATION
Heredia Barión PA, Strelin JA, Roberts SJ, Spiegel C, Wacker L, Niedermann S, Bentley MJ, Pearson EJ, Czalbowski NTM, Davies SJ, Schnetger B, Grosjean M, Arcusa S, Perren B, Hocking EP and Kuhn G (2023), The impact of Holocene deglaciation and glacial dynamics on the landscapes and geomorphology of Potter Peninsula, King George Island (Isla 25 Mayo), NW Antarctic Peninsula. *Front. Earth Sci.* 10:1073075. doi: 10.3389/feart.2022.1073075

The impact of Holocene deglaciation and glacial dynamics on the landscapes and geomorphology of Potter Peninsula, King George Island (Isla 25 Mayo), NW Antarctic Peninsula

Pablo A. Heredia Barión[1,2,3], Jorge A. Strelin[3,4], Stephen J. Roberts[5]*, Cornelia Spiegel[2], Lukas Wacker[6], Samuel Niedermann[7], Michael J. Bentley[8], Emma J. Pearson[9], Nadia T. Manograsso Czalbowski[10,11], Sarah J. Davies[11], Bernhard Schnetger[12], Martin Grosjean[13], Stephanie Arcusa[13], Bianca Perren[5], Emma P. Hocking[14] and Gerhard Kuhn[1,2]

[1]Alfred-Wegener-Institut Helmholtz-Zentrum für Polar und Meeresforschung Geosciences Division, Bremerhaven, Germany, [2]Department of Geosciences, University of Bremen, Bremen, Germany, [3]Centro de Investigaciones en Ciencias de la Tierra (CONICET-UNC), Córdoba, Argentina, [4]Instituto Antártico Argentino, Convenio MREC—Universidad Nacional de Córdoba, Córdoba, Argentina, [5]British Antarctic Survey (BAS), Natural Environmental Research Council (NERC), Cambridge, United Kingdom, [6]Laboratory of Ion Beam Physics, ETH Zürich, Zürich, Switzerland, [7]Deutsches GeoForschungsZentrum GFZ, Potsdam, Germany, [8]Department of Geography, Durham University, Durham, United Kingdom, [9]School of Geography, Politics and Sociology, Newcastle University, Newcastle upon Tyne, United Kingdom, [10]Instituto Antártico Argentino (IAA), Buenos Aires, Provincia de Buenos Aires, Argentina, [11]Department of Geography and Earth Sciences, Aberystwyth University, Aberystwyth, United Kingdom, [12]Institute for Chemistry and Biology of the Marine Environment (ICBM), Oldenburg, Germany, [13]Institute of Geography and Oeschger Centre for Climate Change Research, University of Bern, Bern, Switzerland, [14]Department of Geography, Northumbria University, Newcastle upon Tyne, United Kingdom

The timing and impact of deglaciation and Holocene readvances on the terrestrial continental margins of the Antarctic Peninsula (AP) have been well-studied but are still debated. Potter Peninsula on King George Island (KGI) (Isla 25 de Mayo), South Shetland Islands (SSI), NW Antarctic Peninsula, has a detailed assemblage of glacial landforms and stratigraphic exposures for constraining deglacial landscape development and glacier readvances. We undertook new morphostratigraphic mapping of the deglaciated foreland of the Warszawa Icefield, an outlet of the Bellingshausen (Collins) Ice Cap on Potter Peninsula, using satellite imagery and new lithofacies recognition and interpretations, combined with new chronostratigraphic analysis of stratigraphic sections, lake sediments, and moraine deposits. Results show that the deglaciation on Potter Peninsula began before c. 8.2 ka. Around c. 7.0 ka, the Warszawa Icefield and the marine-facing Fourcade Glacier readvanced across Potter Peninsula and to the outer part of Potter Cove. Evidence of further readvances on Potter Peninsula was absent until the

Warszawa Icefield margin was landward of its present position on three occasions: c. 1.7–1.4 ka, after c. 0.7 ka (most likely c. 0.5–0.1 ka), and by 1956 CE. The timing of Holocene deglaciation and glacier fluctuations on Potter Peninsula are broadly coeval with other glacier- and ice-free areas on the SSI and the northern AP and likely driven by interactions between millennial–centennial-scale changes in solar insolation and irradiance, the southern westerlies, and the Southern Annular Mode.

KEYWORDS

deglaciation, geomorphological mapping, radiocarbon dating, South Shetland islands, stratigraphy, glacier readvance

1 Introduction

The average annual temperature of the northern Antarctic Peninsula (AP) and South Shetland Islands (SSI) region (Figure 1A) has increased by almost 3°C (from −2.5°C) since the middle of the last century (Vaughan et al., 2003; Meredith and King, 2005; Turner et al., 2016), exceeding average global warming by ~1.5°C–1.8°C (Sánchez-Lugo et al., 2018; Kaufman et al., 2020), leading to enhanced ice sheet thinning, glacier retreat, and permafrost thawing (Steig et al., 2009; Serrano et al., 2012; Bockheim et al., 2013; Osmanoğlu et al., 2013; Vaughan et al., 2013).

Past ice sheet, ice cap, and outlet glacier behavior provides an important long-term context for recent changes and allows for assessments of whether the current rates of change are beyond the range of natural variability (Bentley et al., 2014). During the global Last Glacial Maximum [g-LGM; 23–19 cal. ka BP, calibrated radiocarbon age in thousands of years before present (Hughes et al., 2013)], the AP ice sheet extended toward the shelf edge, and a secondary, smaller ice cap covered the northwest AP/SSI region, reaching the outer continental shelf ~50 km north of its present location in the inner fjords of the Maxwell Bay, King George Island (KGI), SSI (Figures 1B, C) (John and Sugden, 1971; Curl, 1980; Ó Cofaigh et al., 2014; Nývlt et al., 2020). Deglaciation on KGI began broadly after 15.4 ± 2.5 ka (Seong et al., 2008), and Maxwell Bay was deglaciated between c. 14.8 and 14.1 cal. ka BP as the LGM ice sheet decoupled from the sea floor (Simms et al., 2011) and became ice-free by 9.1 cal. ka BP (Simms et al., 2011; Watcham et al., 2011). On land, lakes formed in deglaciated ice-free areas above the Holocene marine limit at ~16 m above present mean sea-level (henceforth, m a.s.l.) on Fildes and Barton Peninsula provide minimum age constraints on deglaciation at, or before, c. 8.1 ka (Watcham et al., 2011; Oliva et al., 2019).

While the deglaciation of the AP and SSI by Termination 1 [the start of the Holocene at 11,700 years b2k—before CE 2000 (Gibbard and Head, 2020)] has been broadly established (Ó Cofaigh et al., 2014), more field data from glacier-free terrestrial areas of the northern AP continental margin are required to assess how natural warming during the transition into the current (Holocene) interglacial drove further local-regional deglaciation and how millennial–centennial-scale changes in climate during the Holocene impacted glacier dynamics (Spada et al., 2013; Bentley et al., 2014). Furthermore, an evaluation of the sensitivity of small ice caps and outlet glaciers of the AP and SSI to smaller-scale amplitude atmospheric and oceanographic forcing during the Holocene is of particular importance for constraining past rates of grounding-line retreat and relative sea level (RSL) change (Hall, 2007; Bentley et al., 2014; Johnson et al., 2022).

Changes in the behavior of the Bellingshausen (Collins) Ice Cap (BIC) on KGI /Isla 25 de Mayo (KGI), the largest island and ice cap in the SSI archipelago, can be constrained using field evidence from its deglaciated peninsulas, such as Potter Peninsula (Figures 1C, 2). Detailed geomorphological mapping and establishing robust chronologies for geomorphological landforms, stratigraphic sections, and lake sediments from glacier- and ice-free areas on these peninsulas can help refine existing models of AP and SSI continental margin deglaciation and allow us to examine the impacts and underlying mechanisms of post-LGM deglaciation and outlet/tidewater glacier readvance(s).

In common with other deglaciated peninsulas bordering Maxwell Bay (Oliva et al., 2019; Oliva et al., 2020) and across the northern AP (Ruiz-Fernández et al., 2019), Potter Peninsula is covered by till and other glacial, periglacial, proglacial, and paraglacial morphostratigraphic deposits, containing datable organic remnants (Sugden and John, 1973; Birkenmajer, 1998; Ballantyne, 2002; Ruiz-Fernández et al., 2019). Fourcade (1960), González-Ferrán and Katsui (1970), John and Sugden (1971), Sugden and John (1973), and Birkenmajer (1998) undertook pioneering work on Potter Peninsula, published geomorphological sketch maps, and reconstructed its glacial history, yet no comprehensive and up-to-date geomorphological synthesis exists. Moreover, in recent decades, the retreat of BIC glacier outlets has exposed new coastlines, landforms, and stratigraphic exposures, and a new assessment of the landform assemblages and their chronologies is now required.

We present a new geomorphological synthesis for Potter Peninsula comprising the first comprehensive geomorphological map constructed using satellite imagery and digital mapping

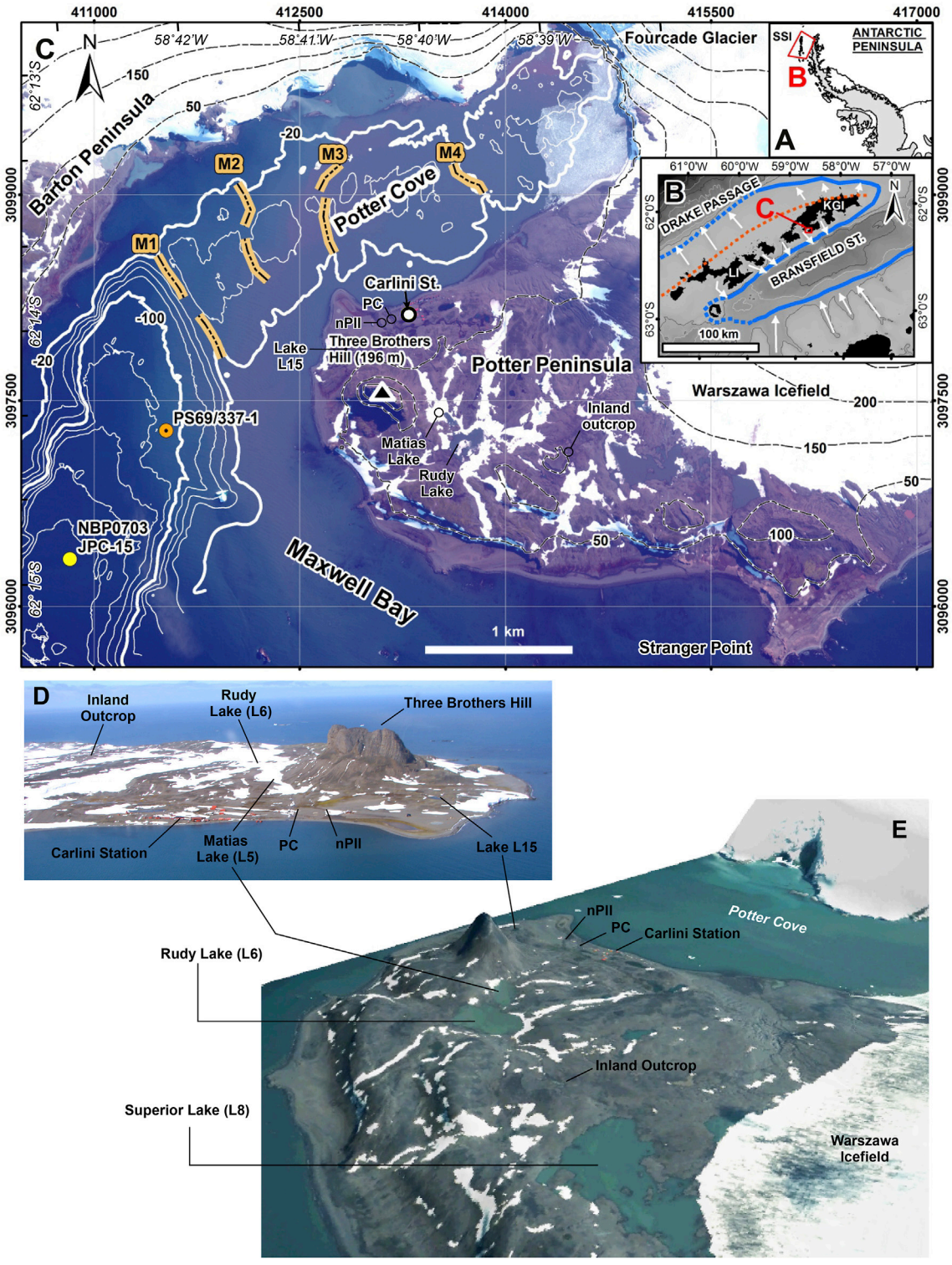

FIGURE 1
Location and geographic context of the study area. **(A)** Location of the South Shetland Islands (SSI) and **(B)** King George Island (KGI) and Livingston Island (LI). Bathymetric contours are every 500 m (Weatherall et al., 2015). Note the extension of the LGM ice cap (blue full and dotted line) and its axis (red dotted line; after Simms et al., 2011). **(C)** Location and topography of Potter Peninsula and bathymetry of Potter Cove (adapted from Deregibus et al., 2015) and the positions of sedimentary cores and moraine complexes (NBP0703_JPC-15, Majewski et al., 2012; PS69/337-1, Wölfl et al., 2016). Moraine complex M4 represents the position of Fourcade Glacier in 1956 (Wölfl et al., 2016). The position of the ice front on land in
(*Continued*)

FIGURE 1 (Continued)
1956 CE is also shown in Figures 2, 3. New stratigraphic sections excavated in this study are nPII, PC, and the "Inland Outcrop"; new lakes cored are Matias Lake (L5) and Lake L15. Projection used is an equal area/distance UTM coordinate system based on the WGS84 ellipsoid (zone 21E) to minimize distortion over short distances. **(D)** Oblique view of Potter Peninsula looking toward Three Brothers Hill (image taken in 02/2008 by Peter Fretwell). **(E)** 3D-DEM drape of the satellite image looking approximately west from the Warszawa Icefield across the deglaciated landscape of Potter Peninsula (scene ID: 1010010004C1B200; pixel resolution .67 m; Maxar Products. Quickbird satellite image acquired 16/01/2006 © 2022 Maxar technologies). The positions of the new stratigraphic sections nPII, PC, and the "Inland Outcrop" and lakes L5 (Matias Lake) and L15 examined in this study are shown. Superior Lake (L8) and Rudy Lake (L6) are also shown for orientation.

techniques and new chronological data from sediment-landform assemblages recording glacier fluctuation on Potter Peninsula (Figures 2, 3). We test the hypothesis that Holocene deglaciation on Potter Peninsula from offshore LGM limits was a continuous process and combine all available evidence to answer the following questions: 1) When did the deglaciation of Potter Peninsula begin? 2) Did readvances from the Warszawa Icefield occur and what was their extent? 3) What were the wider regional–global drivers and impact of deglaciation and glacier readvance(s) on Potter Peninsula and the SSI?

To provide samples for dating, we excavated a new, deeper stratigraphic section in a similar location to del Valle et al. (2007), close to Mirounga Point on the outer Peninsula (nPII in Figure 2, Location 1 in Figure 3). We also excavated a river section on Potter Peninsula that cuts through the same moraine sampled by Sugden and John (1973) (PC in Figure 2; Location 2 in Figure 3) and a new "Inland outcrop" ~700 m from the active glacier front, recently exposed (2013 CE) by the deglaciation of the glacier foreland (Figure 2, Location 3 in Figure 3). Results from these records were compared with ^{3}He cosmogenic nuclide exposure dating of boulders from the Three Brothers Hill moraine system and data from new lake sediment records extracted from Matias Lake (ML in Figure 2), located outside the 1956 CE glacier limit of the Warszawa Ice Field, and Lake L15 (L15 in Figures 2, 3; Supplementary Figure S2), the furthest permanent water body from the active glacier front of the Warszawa Icefield.

2 Geology, climate, and glaciological setting of Potter Peninsula

2.1 Study area and geology

Potter Cove is an inner fjord of Maxwell Bay bordering the Fourcade Glacier, a marine-terminating glacier located on the northeastern side of the fjord (Figure 1C). The Warszawa Icefield to the south of the Fourcade Glacier defines the eastern border of the deglaciated Potter Peninsula (Figure 1C). Both glaciers are outlets of the BIC (Collins Ice Cap) that covers approximately 90% of the surface of KGI, to a maximum thickness of about 400 m (Blindow et al., 2010). Aerial and satellite imagery shows that the Warszawa Icefield and the Fourcade Glacier retreated rapidly between 1956 and 2013 CE, with ~40% of the present-day deglaciated area of Potter Peninsula becoming ice-free during that time (Figure 3).

Lava flows, pyroclastic rocks, and related hypabyssal intrusives are exposed on Potter Peninsula, and the basalts of the peninsula have been potassium-argon dated at 49 ± 1 to 42 ± 1 Ma (Smellie et al., 1984; Kraus and del Valle, 2008a, b). Three Brothers Hill (196 m a.s.l.), an andesitic plug with transverse faults and columnar jointing formed during the final stages of a Palaeogene stratovolcano, is the most prominent topographic feature on Potter Peninsula (Figures 1D, E) (Birkenmajer 1998).

2.2 Climate

The mean annual air temperature on KGI between 1948 and 2011 CE was −2.5°C, with Austral summer temperatures often above zero (Kejna et al., 2013). A warming trend observed since the 1950s has paused, with a slight cooling occurring between 1999 and 2015 CE (Oliva et al., 2017). In contrast to the high interior atmospheric pressure of the West and East Antarctic plateau, the climate of the northern AP and SSI is influenced by the mid-latitude and/or the polar atmospheric cells (Bentley et al., 2009). Atmospheric cells and the Southern Hemisphere Westerly winds (SHW) bring warm and moist air masses formed at lower latitudes over the surrounding oceans and ~1,000 mm yr^{-1} of precipitation (Turner et al., 2002; Bentley et al., 2009; Falk et al., 2018), which drives snow accumulation, glaciofluvial erosion, and surface- and groundwater discharge into Potter Cove (Falk and Silva-Busso, 2020). Potter Peninsula becomes largely snow-free during the Austral spring/summer, but ephemeral snow patches persist well into late summer. The wind flow in Potter Cove is predominantly from SW to NW, with a mean annual wind speed of ~15 m s^{-1} and weaker katabatic component (Falk et al., 2018).

Between 1996 and 2005 CE, increased cyclonic activity in the Drake Passage, associated with more poleward-focused SHW and an increasingly more positive phase of Southern Annular Mode (SAM), drove sea ice poleward, increasing the advection of warm air across southern Patagonia, the northern AP, and SSI during winter (Kaplan et al., 2016, 2020; Marshall et al., 2017; Oliva et al., 2017; Reynhout et al., 2019). Conversely, between 2006 and 2015 CE, colder winters pushed sea ice north, increasing snowfall across the northern AP and doubling

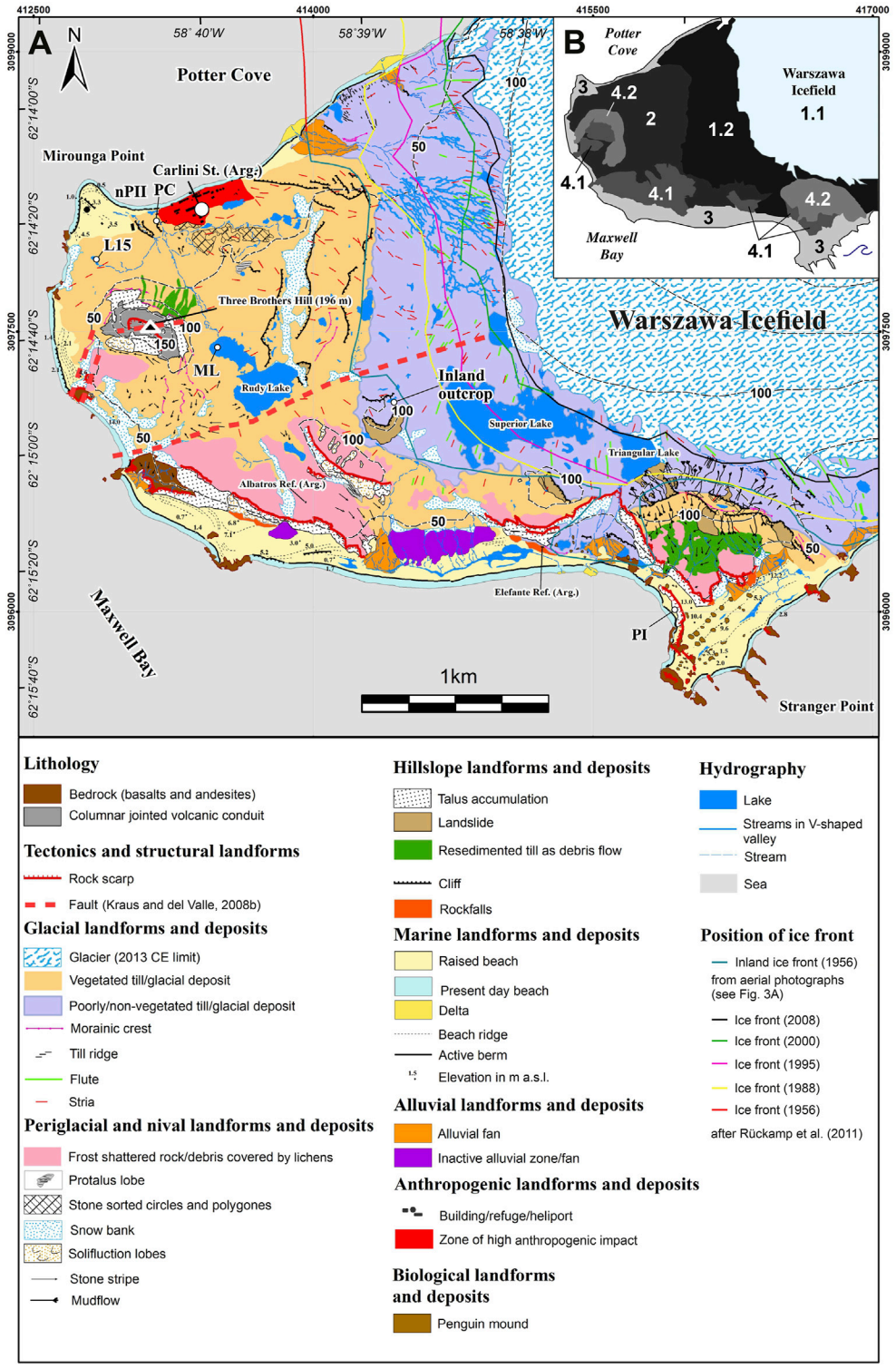

FIGURE 2
(A) Geomorphological map of Potter Peninsula showing landform assemblages in the main text and the location of key sites in this study: nPII, new Pingfo II section; PC, Potter Cove section (Sugden and John, 1973) and new Potter Cove section; L15, Lake L15; ML, Matias Lake, connected to Rudy Lake; PI is the Pingfo I section (del Valle et al., 2002). **(B)** Summary map of landform assemblage zones 1–4, subdivided as follows: 1.1) glacier and snow assemblage; 1.2) active glacial and proglacial sediment landform assemblage (deglaciated since 1956 CE); 2) moss and lichen vegetated inactive glacial landforms and deposits, including till deposits and inactive glaciofluvial fans, deglaciated before 1956 CE; 3) paraglacial
(*Continued*)

FIGURE 2 (Continued)
assemblage: glaciomarine and glaciofluvial landforms and deposits, including raised beaches, deltas, and active (proglacial) glaciofluvial fans; 4.1) periglacial assemblage, nival landforms, and deposits; 4.2) hillslope landforms and deposits, including redeposited till. These zones are referred to in the results section and Table 1. The geomorphological map of Potter Peninsula was constructed by comparing geomorphological features identified and interpreted in the field with the study of a high-resolution WorldView2, DigitalGlobe satellite image shown in Figure 3B (scene ID: 103001001F612100; pixel resolution 0.5 m; Maxar Products. Quickbird satellite image acquired 07/03/2013 © 2022 Maxar technologies). Topography is based on the King George Island digital elevation model (KGI-DEM) with a spatial resolution of 3 m pixel-1 (Kraus and del Valle, 2008b), with georeferenced landforms mapped from their surveyed localities. The mapping projection used in **(A)** was an equal area/distance UTM coordinate system based on the WGS84 ellipsoid (zone 21E), which minimizes distortion over short distances within a single UTM zone at the poles.

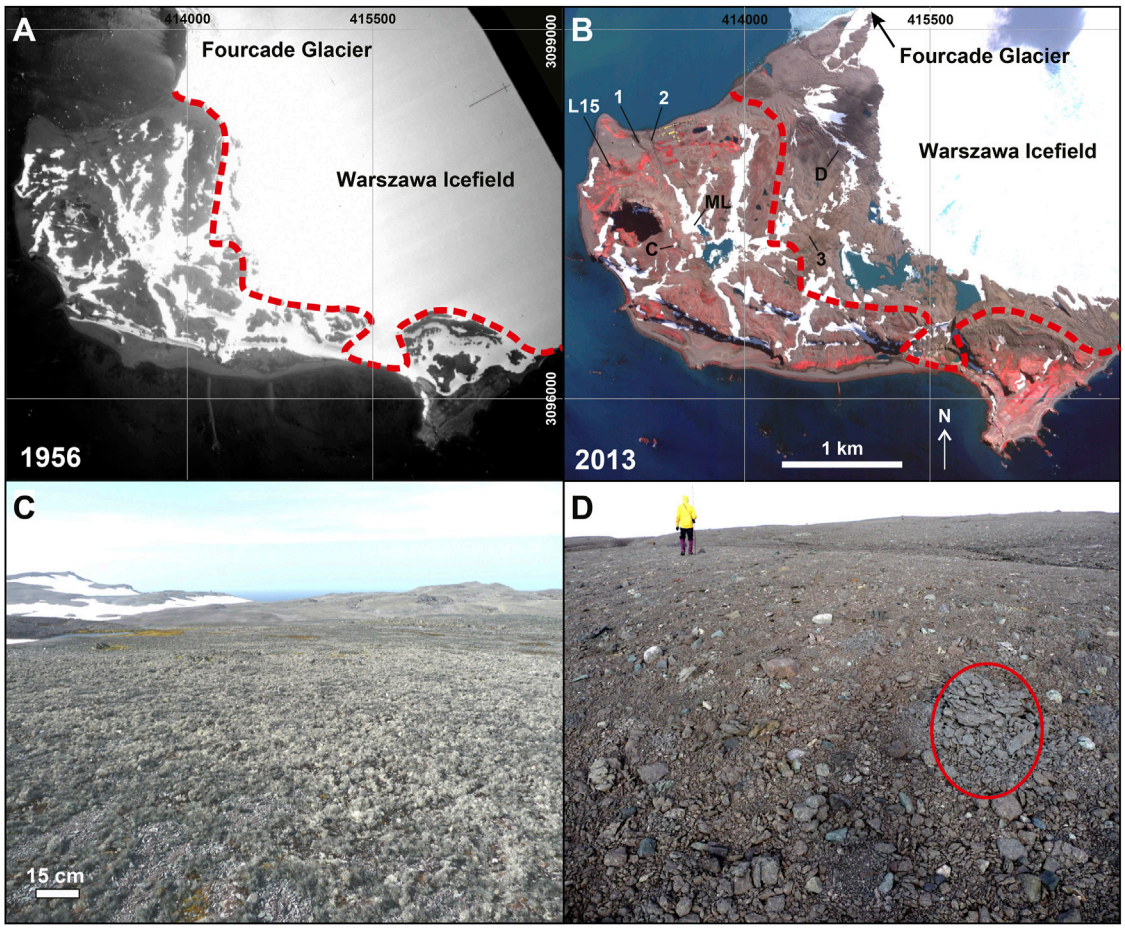

FIGURE 3
(A) Comparison between the positions of the tidewater Fourcade and inland Warszawa glaciers in 1956 CE (aerial photograph) and **(B)** 2013 CE (satellite image). Due to the extended snow cover season, locating the position of the terrestrial glacier margin is challenging, and retreat limits (red dotted lines) should be viewed as maxima. **(B)** Composite satellite image (NIR-G-B) of Potter Peninsula in 2013 with red areas reflecting the vegetation cover (mostly lichens). **(C,D)** Vegetated and recently deglaciated glacial deposits, respectively, of the glacial landform assemblages. Note the action of freeze-thaw processes causing laminated cracking in pyroclastic lithologies (red circle in D). **(A,B)** Stratigraphic sections and new lake records are labeled as follows: 1, new Pingfo II; 2, new "Potter Cove" section; 3, Inland glacial deposits; L15, Lake L15; ML, Matias Lake. See Figures 5–7 for stratigraphic profiles. The locations of photographs shown in Panels **(C,D)** are marked. To infer the area deglaciated in recent decades, we used an orthorectified panchromatic aerial image of 1956 CE in **(A)** (Falkland Island Dependency Aerial Survey Expedition, FIDASE; image ID X26FID0039076; pixel resolution 0.9 m; acquired 1956/12/20) and a WorldView2, DigitalGlobe satellite image in **(B)** (scene ID: 103001001F612100; pixel resolution 0.5 m; Maxar Products. Quickbird satellite image acquired 07/03/2013 © 2022 Maxar technologies).

snow cover on some SSI islands between 2009 and 2014 CE (de Pablo et al., 2013; Oliva et al., 2017).

The SAM is the primary mode of interannual and decadal to centennial-scale atmospheric circulation variability in the Southern Ocean and reflects the zonal mean sea level pressure difference between Antarctica (>65°S) and the mid-latitudes (40°S) (Marshall, 2007; Moreno et al., 2018; Kaplan et al., 2020). The SAM index is a measure of the longitudinal mean SHW strength, with positive phases characterized by stronger and poleward-shifted SHW (Marshall, 2007; Charman et al., 2018; Kaplan et al., 2020). Negative phases are characterized by generally colder and, in some places, more humid conditions and weaker (and/or more diffuse), possibly equatorward-shifted, SHW (Marshall, 2007).

Interactions between the SAM and a deepening Amundsen Sea low during positive SAM phases can also bring warmer air from the Atlantic and north-easterly winds with cooler air from the Weddell Sea gyre, leading to colder/wetter conditions on the northern AP and low-lying SSI and increased glacier mass (Liu et al., 2005; Thomas et al., 2008; Goodwin et al., 2016; Oliva et al., 2017; Falk et al., 2018; Kaplan et al., 2020). These processes are intensified further in the Pacific sector that feeds the AP by interactions between SAM and the (sub)decadal-scale El Niño Southern Oscillation (ENSO). Positive (enhanced) phases of ENSO (El Niño) drive warmer interannual global mean temperature variability and negative phases of the SAM (Wang and Cai, 2013; Turner et al., 2016). Decadal scale variability in temperature measured at stations on the AP and SSI has been linked to changes in ENSO (Oliva et al., 2017).

2.3 Glaciological setting

Observations, numerical simulations, and ground-penetrating radar data indicate that the BIC is a partly temperate ice cap, with cold ice at higher elevations and temperate ice at lower elevations (Blindow et al., 2010; Rückamp et al., 2010, 2011). The Warszawa Icefield margin is a polythermal, debris-covered glacier, and ice-cored and thrusted moraines can be found at Stranger Point (Figure 2A). Increased precipitation on the western AP over the last 5 decades (Thomas et al., 2008; Goodwin et al., 2016) has resulted in a slightly positive glacier mass balance on northern AP islands and the SSI overall (Oliva et al., 2017). From 1970 to 1990 CE, the BIC had a stable to slightly negative glacier mass balance and an equilibrium line altitude (ELA) at ~ 150 m a.s.l. (Curl, 1980; Turner et al., 2002; Bentley et al., 2009; Falk et al., 2018). By 2015 CE, the ELA had risen to ~260 m a.s.l., and glacier flow rates had accelerated (Falk et al., 2018). Across the SSI, permafrost is discontinuous between 0 and 30 m a.s.l. Colder conditions between ~30 and 50 m a.s.l. favor the formation of continuous permafrost. Above 50 m a.s.l., permafrost dominates periglacial processes, but permafrost is less common above 90 m a.s.l. (Serrano et al., 2012; Oliva et al., 2020).

The deglaciation of Potter Peninsula left behind numerous glacial landforms. Inland moraines are surrounded by a coastal environment with older (Holocene-age) raised beaches and marine deposits (John and Sugden, 1971; Lindhorst and Schutter, 2014; Heredia Barión et al., 2019). Holocene RSL curves for the SSI are more complex than in other locations on the AP, and several different curves have been constructed (Pallàs et al., 1997; Bentley et al., 2005; Hall, 2010; Roberts et al., 2011; Watcham et al., 2011; Simms et al., 2012, 2021; Johnson et al., 2022). Bentley et al. (2005) (and Johnson et al. (2022)) proposed an early-mid Holocene marine limit of ~16–18 m a.s.l. for the SSI. Based on the ages of marine-freshwater transitions and the altitude of isolation basins on nearby Fildes Peninsula, Watcham et al. (2011) built on the pioneering work of Mäusbacher et al. (1989) and refined this to a more conservative estimate of ~16 m a.s.l. On Potter Peninsula, del Valle et al. (2002) constrained the onset of the deglaciation and raised beach formation between 17.1 and 14.4 m a.s.l. at Stranger Point (Pingfo-I, PI in Figure 2) with a minimum age of 5.5–5.4 cal. ka BP from elevated coastal sediments, although Fretwell et al. (2010) and Lindhorst and Schutter (2014) later revised the maximum raised beach altitude on Potter Peninsula to 12.2 m a.s.l.

There are several low-altitude sedimentary sections close to the present-day sea level along the south side of Potter Cove are ~200 m west of the Argentinian Carlini station, ~2 km from the front of the modern glacier terminus, and ~1 km from its 1956 CE position (Figures 2, 3). They are composed of marine intertidal sands with remnants of algae and marine mollusks, bivalves, and the bones of penguins, seals, and cetaceans, deposited in an ice-free environment, and capped by a till that represents the last time a local glacier readvanced over the outer part of Potter Cove/Peninsula (Sugden and John, 1973).

Radiocarbon dating of the deepest buried shells and seaweed in these sections provides a maximum age constraint for deglaciation (Strelin et al., 2014). By analogy with observations from modern beaches on Potter Peninsula, seaweed was probably deposited as large trash, subfossil deposits close to the high tide level (Fretwell et al., 2010; Strelin et al., 2014). Sugden and John (1973) first dated shells from a 2.5 m thick stratigraphic section of the "Potter Cove section" (located close to PC in Figure 2) and proposed the oldest age for the onset of the deglaciation and marine transgression from the outer part of Potter Peninsula of 9,670 ± 230 ^{14}C years, or 9,570 ± 650 cal. a BP (S&J Birm-48a in Table 2, recalibrated in this study). Del Valle et al. (2007) used these ages to constrain the age of a stratigraphic

TABLE 1 Summary descriptions of landform assemblages and local geomorphological units identified in this study on Potter Peninsula.

Assemblage	Landforms and moraine systems	Characteristics, distribution, dimension landforms, and geomorphological features	General observations and interpretations
1. Glacier ice and snow, active glacial sediment-landform assemblage	Polished and striated blocks	Linear and continuous glacial scratches and polish on boulder surfaces, distributed across different volcanic lithologies	• Transverse structures recently revealed at the snout of the Warszawa Icefield follow the ice margin, with longitudinal foliation showing radial ice flow patterns (Figures 2, 4A, C). They are associated with glacial debris, suggesting a structural control (e.g., englacial thrusts) and melt-out debris release (Figures 2, 4B, C, E)
	Till ridges (squeeze-crevasse-ridges)	Aligned longitudinal diamicton ridges, ~0.3 m high and ~15–50 m long	• Mudflows reworking the unconsolidated glacial sediments exist at the contact between ice-core/permafrost and the active layer
	Moraine ridges	Linear and curvilinear ridges with gentle lee-flanks and steep stoss flanks	• The recently deglaciated area bordering the Warszawa Icefield is waterlogged and composed of glacial deposits and till without vegetation cover (Figures 2, 3B, 4A)
	Deltas	Fan-shaped features resulting from the discharge of proglacial streams carrying sediments to the sea. 70 m long and 200 m wide. Supraglacial streams aligned with radial structures were visible during warm summer days when snow had melted (Figure 4D). Numerous snowbanks are present in the lee of rock scarps and hill slopes, feeding ephemeral streams flowing on warm summer days (Figure 2)	Interpretation: The Warszawa Icefield is an active glacier with structural glaciological controls on landform and sediment development, typical of polythermal glaciers in wet high-latitude maritime environments (Glasser and Bennett, 2004; Hambrey and Glasser, 2012)
	Lakes	Semi-permanent intra-moraine water bodies. Triangular Lake has an outflow toward the south. Infilled hollows with water source from snowpacks, thawing of permafrost/ice core and seasonal proglacial streams. Many lakes in this zone have developed in the last few decades as the glacier front retreated (Figure 3B)	
	Alluvial fans	Fan-shaped deposits of decametric dimensions built from sediment discharge in proglacial streams and connected to deltas downstream	
	Landslides	Erosive scars and convex accumulation of debris triggered by water saturation of the active layer resting on permafrost. 225 m wide, 70 m long	
2. Glacial assemblage: inactive glacial landforms, deposits, and moraine systems	Lakes	Intra-moraine water bodies. There are also infilled hollows whose water source is from snowpacks; water also comes from mass movements after the degradation of moraines	
	Stone-sorted circles and polygons	Features on gentle surfaces (3°–5°) with thick-grained (i.e., cobbles) sediments toward the periphery. Mainly developed in water-saturated areas along streams	• Vegetated glacial deposits, containing predominantly mosses and lichens, occupy the western and southeast sectors of the peninsula, which have been ice-free since at least 1956 CE (Figures 2, 3B, C, 4G)
	Stone stripes	Features with classified sediments of several cm widths and several meter lengths. Developed in slopes up to 10° and between 20 and 50 m a.s.l.	• Large polished and striated boulders of coarse-grained pyroclastic lithologies and andesitic and basaltic blocks are common in these deposits (Figure 8E)
	Inactive protalus lobe	Feature with tongue-like form conformed of angular boulders. 75 m long, 70 m wide. Located at	• At the east of Rudy Lake, debris flows have developed on the interface between the active layer and permafrost/ice core

(Continued on following page)

TABLE 1 (*Continued*) Summary descriptions of landform assemblages and local geomorphological units identified in this study on Potter Peninsula.

Assemblage	Landforms and moraine systems	Characteristics, distribution, dimension landforms, and geomorphological features	General observations and interpretations
		30 m a.s.l., vegetation implies these landforms are inactive	(Figure 4F). In some areas, partially vegetated bedrock plateau surfaces are still relatively fresh and exhibit polished surfaces and striae
	Landslides	Erosive scars and shallow convex accumulation of debris triggered by water saturation of the active layer of permafrost	• Several till ridges are located along the north coast of Potter Peninsula, between two alluvial fans, former deltas, nourished by glacial-lateral meltwater channels (Figure 2)
	Flutes	Streamlined, attenuated, lineal hills, associated or not with bedrock obstacles and boulders. Length: width, from 20:1 to 10:1	• Recent ice retreat has exposed fluted glacial deposits (flutings) (Figures 2, 4H, I). On the north of the peninsula, flutes are oriented NW-SE, whereas west of Superior Lake, they are oriented NNE-SSW, and toward Stranger Point N-S and NW-SE orientations dominate
	Striated and polished blocks and bedrock	Linear, continuous glacial polish and scratches on some bedrock outcrops and boulder surfaces. Present in mostly basaltic and andesitic lithologies	• Moraine ridges of 80 m length are located southeast of the till ridges. Intensely polished and striated cobbles and boulders of coarse-grained pyroclastics and basaltic and andesitic lithologies are dominant
	Stranger point moraine system, SE Potter Peninsula	• North of Stranger Point a moraine ~200 m from the ice margin, rises to ~105 m a.s.l. and over 1.25 km long and elevated ~40 m above the adjacent bedrock plateau. Its eastern flank descends smoothly toward the present-day beach, whereas the western side descends to 50 m a.s.l. bordering Triangular Lake. A discontinuous moraine borders the ice on its northern flank directly on the bedrock plateau and is exposed to the south	Interpretation: The Stranger Point moraine system has many features typically associated with ice-cored moraines. The ice-proximal slope of the moraine is covered with flutings, indicative of glacier overriding and deformation (Evans and Hiemstra, 2005). These features were most likely formed through proglacial or englacial thrusting and pushing of polythermal ice at the glacier margin. On Potter Peninsula, these features largely manifest as landslides, superficial debris flows, steep slopes, and scars showing permafrost as well as stratified glacier ice, thrusts, a pond bordered by asymmetric ridges and striated boulders and clasts (Figures 8A–E, cf. Davies et al., 2013)
		• At Stranger Point, a moraine rests up to ~25 m above relict raised beaches ~5–12 m a.s.l. Relatively few morainic crests are preserved due to slumping and debris flows, but the two most prominent morainic ridges enclose a small pond (Figures 2, 8B). The moraine is composed of unconsolidated, matrix-supported, basaltic, and andesitic gravels and boulders. Some boulders show striae and polished surfaces (Figure 8D). Coarse-grained volcanics (pyroclastics) are generally intensely cracked (reworked) by cryoturbation processes, generating stone-sorted polygons and stone stripes several meters long (Figures 4G,J)	As mudflows and landslides are generated at the contact between the permafrost (upper frozen till) and the active layer (Figures 4F, 8A), the permafrost table acts as the sliding surface for the downslope mobilization of the water-saturated overlying sediments (Oliva and Ruiz-Fernández, 2017). Landslides are triggered by the water saturation of the active layer. Melting of ice-cored moraines observed in this and other studies provides sufficient meltwater to trigger debris flows (Figures 4F, 8A) (John and Sugden, 1971; Sugden and John, 1973; Hochschild, 1995; Davies et al., 2013)
		• The northern morainic ridges are highly degraded by debris flows, which have redeposited unconsolidated moraine sediments downslope. The northern, ice-facing slope of the Stranger Point moraine declines toward the glacier at ~20°. More sunshine on the northern slope means snow does not accumulate, and the active layer thaws deeper and faster. For this	

(Continued on following page)

TABLE 1 (*Continued*) Summary descriptions of landform assemblages and local geomorphological units identified in this study on Potter Peninsula.

Assemblage	Landforms and moraine systems	Characteristics, distribution, dimension landforms, and geomorphological features	General observations and interpretations
		reason, periglacial mass movement processes (mudflows and landslide) are reworking unconsolidated sediments faster on the northern slopes (Figure 2)	
	Three Brothers Hill moraine system, central Potter Peninsula	• The Three Brothers Hill moraine system is located between 100 and 10 m a.s.l. It is partly vegetated by lichens and mosses and has a similar bedrock composition to the Stranger Point moraine (Figure 2). Its topography is most pronounced around the northern flank (up to 40°N–NW slope inclination). In contrast, the south–eastern flank only has a slope of 5°S-SE, with gently sloping moraine ridges spaced more than 100 m apart (Figure 2)	Flutes formed parallel to the ice flow are the product of combined erosional and depositional processes of subglacial origin in a water-saturated (warm-based) bed of deformable till (Glasser and Bennett, 2004; Benn and Evans, 2010). Till ridges resemble crevasse-squeeze ridges formed by pressing saturated basal till during stagnation phases transverse to glacial flow (Benn and Evans, 2010), especially on inter-ice stream ridges (Klages et al., 2013). Till ridges emerging on the glacier front were also most likely formed by ice-thrusting (Figure 4B)
		• Talus accumulations and rock falls from frost action weathering on Three Brothers Hill partially cover preserved morainic ridges on the northern side (Figure 2). Centimeter-scale stone stripes have formed on the surface of the southern sector, which is heavily degraded	As morainic ridges surround Three Brothers Hill (Figure 2), these moraines are most likely formed by ice pushing against the hill. Degraded and re-deposited morainic till has been reworked by solifluction on inclined surfaces, creating stone stripes at the Stranger Point and Three Brothers Hill moraine systems
3.1 Paraglacial, proglacial landforms, and moraine systems	Kettle lakes	Water-filled hollow created by water of seasonal snowpacks and fusion of ice core or active table	General observations: Several meltwater channels and related deposits (glaciofluvial fans) resting on the coast are a product of the discharge of moraine sediments from debris flows and sediments transported by snow and ice-melting streams on raised beaches. For example, discharge from Triangular Lake to the sea has formed an alluvial fan and a small delta between its southern outlet and the beach (Figure 2). Inactive glaciofluvial fans cover raised beaches, which terminate against a lagoon on the south coast of the peninsula, next to the "Elefante Refugee" (Figure 2)
	Polished and striated blocks	Linear and continuous glacial scratches and polishing on boulder surfaces	NW of Warszawa Icefield, meltwater channels from its glacier front cut steep interfluves up to 4 m high into the fluted glacial deposits and run parallel to the axes of the flutes (Figure 4H) and discharge into the cove, forming two glaciofluvial fans and deltas (Figure 2). The Rudy–Matias Lake system developed within these deposits and has an outflow into Potter Cove that cuts through the moraine in which the Potter Cove and Pingfo II sections are located
	Stone-sorted circles/ polygons	Features on gentle surfaces (3°–5°) with coarse-grained (i.e., cobbles) sediments toward the periphery. Located at 90 m a.s.l.	
	Landslides	Accumulation of debris triggered by water saturation of the active layer resting on permafrost and ice-cored moraines. Distributed on the slopes of the moraine, 20/80 m width, 120/180 m length	Interpretation: Clast-supported, rounded, and sub-rounded cobbles facing the northern flank of Three Brothers Hill were originally interpreted by John and Sugden (1971) as pockets of *in situ* beach material composed of prolate to spheroid clasts. These "residual beaches" were deposited by

(Continued on following page)

TABLE 1 (*Continued*) Summary descriptions of landform assemblages and local geomorphological units identified in this study on Potter Peninsula.

Assemblage	Landforms and moraine systems	Characteristics, distribution, dimension landforms, and geomorphological features	General observations and interpretations
			glaciomarine and/or glaciofluvial processes in a previous (Pleistocene) interglacial or interstadial period but subsequently overridden by ice. Alternatively, they could be interpreted as early Holocene kame terrace deposits
	Stone stripes	Features with classified sediments of several cm in width and several meters in length. Developed on slopes up to 10°, located between 20 and 70 m a.s.l.	
	Mudflows/slumps	Rapid mass movements of variable size in fine-grained sediments transporting material down-valley onto the Stranger Point moraine system. The sliding surface corresponds to the limit of the active layer in contact with the permafrost table. More abundant on the northern (sun-facing) slope of the Stranger Point moraine	
	Clast-supported, rounded, and sub-rounded cobbles	Deposits of clast-supported, rounded, and sub-rounded cobbles facing the northern flank of Three Brothers Hill at ~110 m a.s.l. have diameters up to 30 cm and are protected from falling scree by an overhanging cliff	
	Resedimented till as debris flows	Degraded moraines surrounding Three Brothers Hill with slopes of 22°–27° reworked into several channelized shallow debris flows. On moraines, slopes of 12°, the debris flows are not channelized and are wider with stone stripes developed on top	
3.2 Paraglacial landforms. Raised beaches, present-day beaches, and proglacial/glaciofluvial landforms	Raised beaches	The highest raised beaches are found at Stranger Point at ~12 m a.s.l. Their elevation and their surface grain-size decrease along the south coast in the direction of Potter Cove to the PDB east of Carlini Station. Beach ridges are well developed, and most are poorly vegetated, except for those next to inactive lagoons and those at Stranger Point	Interpretation: The southern and west coast of the peninsula is occupied by a series of raised beaches composed of gravel beach-ridge systems that developed on top of a prograding strand plain (Lindhorst and Schutter, 2014). The northern coast exhibits modern gravel ridges up to 2 m a.s.l., gently sloping seawards. The rest of the coastline is composed of beach ridge systems at ~11.5, 9.5, 7.5, and ≥5.5 m a.s.l. (Lindhorst and Schutter, 2014), with a well-developed spit system at Mirounga Point in the mouth of Potter Cove (Heredia Barión et al., 2019) (Figure 2).
	Present-day beach (PDB)	The PDB surrounds the Peninsula, with an active berm mean elevation range of 2.4 m a.s.l. at Stranger Point to up to 1 m a.s.l. at Mirounga Point. There is biological activity (penguins, sea lions, elephant seals, and stranded algae)	At Stranger Point, numerous abandoned and still populated penguin rookeries are situated on top of the penguin-formed pebble mounds, which are up to 35 m in diameter and up to 2 m higher than underlying raised beach ridges at 12.2 m a.s.l. (Fretwell et al., 2010). The present-day beach is ~2 m a.s.l., depending on exposure to prevailing waves (Fretwell et al., 2010; Lindhorst and Schutter, 2014)
	Deltas	Features resulting from the discharge of fluvial sediments in the sea. Up to 50 m long and 70 m wide	
	Alluvial fans	Fan-shaped deposits of decametric dimensions. Built up from moraine material, basically through debris flow and sediments transported by snow-melting streams	

(Continued on following page)

TABLE 1 (*Continued*) Summary descriptions of landform assemblages and local geomorphological units identified in this study on Potter Peninsula.

Assemblage	Landforms and moraine systems	Characteristics, distribution, dimension landforms, and geomorphological features	General observations and interpretations
	Inactive alluvial zone/fans	Deposits of debris of alluvial origin are no longer active. They cover raised beaches	
	Penguin mounds	Approximately circular, dome-shaped features up to 20–25 m in diameter and 3 m in height. Principally distributed in raised beaches of Stranger Point and next to the present-day beach along the southeast coast	
	Lake/lagoon	Permanent water body distributed in flat areas present between a series of raised beaches and the active berm	
4. Periglacial and Hillslope landforms	Polished bedrock (striae)	Linear and continuous scratches and polish of glacial origin on bedrock surfaces	General observations: • Active periglacial processes, such as frost cracking and freeze-thaw, occur in some cobbles and boulders of coarse-grained pyroclastic lithologies (Figure 3D), while large boulders of the same lithologies are more resistant to such processes and remain intensely polished and striated
	Talus accumulations	Located from sea level up to 100 m a.s.l. on Potter Peninsula, these accumulations of coarse sediments at the foot of rock cliffs have been intensely affected by frost shattering. Poorly lichenized sediments suggest they are active or recently dynamic, an exception being around Three Brothers Hill	• Basaltic lithologies are generally more resistant to periglacial processes. Two tilted bedrock plateaus landward of the south coast of the peninsula between 40 and 95 m a.s.l. and a near-horizontal plateau at Stranger Point at ~45–50 m a.s.l. are intensely gelifracted and frost-shattered (Figure 4J)
	Solifluction lobes	Generally, solifluction lobes are densely covered by vegetation and located between 80 and 40 m a.s.l. on the bedrock plateaus without vegetation cover. Their width depends on whether they are associated with rock scarps or located on the plateau. They appear as step-like landforms at Three Brothers Hill on south-facing talus slopes, often with the concentration of clasts in the risers varying from 30 cm up to 1 m in lobes, which appear as tongue-like features ~5 m width in slopes of up to 20°	• In some areas, the bedrock is relatively fresh and exhibits polished surfaces and striae. One of the tilted plateaus has a slope of 10°, and solifluction processes have evacuated debris by frost shattering and creep to form stone stripes
	Rock falls	Accumulation of large blocks fallen from the margin of bedrock outcrops adjacent to sea level up to 14 m a.s.l.	• Protalus lobes, solifluction lobes, and talus accumulations at the foot of rock scarps of the bedrock plateaus descend to raised beaches (Figure 2A)
	Stone stripes	Features with classified sediments of several cm in width and several meters in length. Developed on slopes up to 10°	• Vegetated solifluction lobes in the shade on the south side of the Three Brothers Hill and a small-sized protalus lobe at 30 m a.s.l. several hundred meters away, southeast of Carlini Station, have been overprinted by sorted polygons and stone stripes deposits (Figure 2A)
	Frost shattered rock/ debris/lichens	Highly gelifracted and vegetated bedrock plateaus between 45 and 90 m a.s.l.	
	Protalus lobes	Feature with tongue-like form at 50 m a.s.l., composed of angular boulders, ~120 m long, 50 m wide. The vegetation cover on the protalus lobes and the absence of a basal talus imply they are inactive	Interpretation: Protalus lobe landforms move down-slope through frost creep and have been associated with deglaciation and transition from a glacial to a periglacial environment on the SSI (Serrano and López-Martınez, 2000). The vegetation cover on the protalus lobes and the absence of a basal talus imply they are inactive (Serrano and López-Martı´nez, 2000; Kääb, 2007)

profile named "Pingfo II" (Location 1 in Figure 3B) 60 m to the west in the same moraine, but the ages obtained by Sugden and John (1973) have not been replicated.

3 Methods

3.1 Geomorphological mapping

Detailed geomorphological mapping is an essential first step in assessing the deglacial history of continental margins around Antarctica (Figures 2, 3). Using a glacial landsystems approach (e.g., Davies et al., 2013), we distinguished landforms and sediment exposures associated with glacier advance and retreat to understand how the landscape on Potter Peninsula evolved during the Holocene (Table 1). Mapping was undertaken in ARC-GIS v.2.5, with final layouts achieved in Adobe Illustrator v. 26.2.1 or CorelDRAW v. 2020.

3.2 Stratigraphic profile, sampling, and lithofacies analysis

Morphostratigraphic descriptions and sampling for radiocarbon dating were undertaken at an outer peninsula stratigraphic profile site excavated in a similar location to the "Pingfo II" profile (del Valle et al., 2007) (Table 2). We refer to the new profile as "new Pingfo II" (nPII in Figure 2 and Location 1 in Figure 3). We also excavated, described, and radiocarbon dated a new river section adjacent to the "Potter Cove section" sampled by Sugden and John (1973). Henceforth, we refer to this as the "new Potter Cove section." Both sections are located at "PC" in Figure 2 and Location 2 in Figure 3. Following recommendations in Björck et al. (1991c), we also radiocarbon dated terrestrial moss samples embedded in a recently exposed "Inland outcrop" ~700 m from the active glacier front and inside the 1956 CE limit to constrain glacier readvance(s) on the inner peninsula area (Figure 2 and Location 3 in Figure 3B). Depositional units in the stratigraphic sections were characterized using lithofacies textural (grain size and fabric), composition, sedimentary structures, and stratigraphic relationship criteria (Supplementary Material for additional methods). Summary results were digitized in Figures 5, 6 using SedLog 3.0 (Zervas et al., 2009), and grain size data are shown in Supplementary Table S1.

3.3 Lake sediment analysis

After mapping, classifying, and assessing the suitability of the numerous lakes on Potter Peninsula for sediment coring (Supplementary Figure S2), we cored and present here summary results from two foreland lake basins: Matias Lake (ML in Figures 2, 3B; Lake L5 in Supplementary Figure S2); and Lake L15 (aka GPS Lake).

Matias Lake (Lake L5, Figures 2, 3B; 62.2450°S, 58.6655°W) is a small lake sub-basin up to ~6 m deep (del Valle et al., 2004) formed in the moraine deposits of the glacier foreland, adjacent and connected to Rudy Lake (Lake L6) in the mid-foreland area (Figure 2; Supplementary Figure S2). Located on the eastern, glacier-facing side of Potter Peninsula at the base of, and shaded by Three Brothers Hill, lake-ice often persists into January or February. In contrast, Rudy Lake and Lake L15 are largely free of lake ice by November–December. The southern basin, Rudy Lake, is a larger but shallower basin, ~4 m at its deepest point (del Valle et al., 2004). Both lakes (L5 and L6) are located outside of the 1956 CE glacier limit of the Warszawa Ice Field (Figures 1, 2), ~500 m NW of the "Inland outcrop." Following a ground penetrating radar (GPR) survey to locate the depocentre in Matias Lake, 13 sediment cores were extracted from a solid lake-ice platform in November 2011 using a 50 mm wide, 1 m long Livingston corer and a 50 mm wide, 0.5 m long Russian corer.

Lake L15 (62.24056°S S, 58.67757°W) is a small shallow bedrock basin (<1–2 m deep) inland from the new Pingfo II section (L15 in Figures 2, 3). It is a seasonally lake-ice-free basin and the furthest permanent water body from the active glacier front on Potter Peninsula (Figures 1, 2; Supplementary Figure S2). Eight cores were taken from a lake-ice platform over the depocentre using a 50 mm wide, 1 m long Livingston corer and a 50 mm wide, 0.5 m long Russian corer.

Livingston cores were split, and all cores were described in the laboratory. Non-destructive ITRAX (Cox Analytical) X-ray fluorescence (XRF) core scanning (XRF-CS) and Bartington Magnetic Susceptibility High-Resolution Surface Scanning Sensor (MS2E) measurements were undertaken at Aberystwyth University and on a Geotek® multi-sensor core logger (MSCL) at Durham University following standard procedures (Gunn and Best, 1998; Davies et al., 2015; Roberts et al., 2022). Contiguous bulk, wet sediment geochemical Energy Dispersive XRF-CS (Energy Dispersive Spectroscopy) data were obtained using a chromium (Cr) X-ray tube (X-radiography image settings: 40 kV, 40 mA, 200 m; XRF-CSCr settings: 30 kV, 40 mA, dwell time of 10 s, at 100 µm (MAT1) and 2 mm (L15-H2, L15-H16) intervals). Machine and sample calibration were undertaken using a synthetic glass standard and XRF fused glass discs of sediment samples from the nearby Yanou Lake and Ardley Lake records on Fildes Peninsula at the start and end of each analytical phase. Raw count per second (cps) data were analyzed using the Cox Analytical Q-spec software.

To account for downcore variations in count rate, density, water, and organic content, XRF-CS data are presented as relative changes in percentages of the total scatter normalized ratio sum (%TSN, equivalent to the %cps sum—Saunders et al., 2018; Roberts et al., 2022) and as natural log ratios and centered log ratios (clr). Log ratios have been shown to produce similar downcore patterns to more traditional and fully quantitative

10.3389/feart.2022.1073075

TABLE 2 Radiocarbon dating results. Samples 1–21 are from the new Pingfo II section (62.2389°S, 58.6729°W), samples 22–25 from the new "Potter Cove" section (62.23895°S, 58.67113°W), 26–27 from the inland outcrop (62.2473°S, 58.6466°W), and 28–30 from the uppermost freshwater subaquatic moss-dominated Unit 3 in the Lake L15-H16 sediment record (62.2405°S, 58.6772°W).

No.	Lab ID	Material dated	Section or core depth (m)	Unit	$\delta^{13}C$ (‰)	AMS ^{14}C age (^{14}C years)	Calibrated age (cal. a BP)		Max.–Min.	2σ %	Mean ± 2σ	Median	Matrix dated, context, interpretation
							Max.–Min.	1σ %					
1	Beta-441402	Bone (penguin)	1.50	4	−21.6	7,860 ± 40	7,590–7,400	68.3	7,680–7,280	95.4	7,490 ± 200	7,490	Fine seds. below till; max. readvance age
2	Beta-441403	Bone (penguin)	1.55	4	−22.2	7,890 ± 40	7,610–7,420	68.3	7,710–7,310	95.4	7,520 ± 200	7,520	Fine seds. below till; max. readvance age
3	ETH-67269	Bivalve shell	1.60	4	−1.6	8,010 ± 85	7,760–7,500	68.3	7,910–7,400	95.4	7,630 ± 250	7,630	Fine seds. below till; max. readvance age
4	ETH-67267	Bivalve shell	1.70	4	.0	7,805 ± 85	7,560–7,320	68.3	7,670–7,180	95.4	7,440 ± 240	7,440	Fine seds. below till; max. readvance age
5	Beta - 431964	Bone (penguin)	1.85	3-4	−23.1	7,780 ± 30	7,510–7,320	68.3	7,610–7,220	95.4	7,410 ± 190	7,420	Fine seds. below till; max. readvance age
6	ETH-67270	Bivalve shell	2.05	3	−1.3	8,170 ± 85	7,920–7,660	68.3	8,030–7,520	95.4	7,780 ± 250	7,780	Fine seds. below till; max. readvance age
7	ETH-67272	Bivalve shell	2.10	3	−13.4	8,115 ± 80	7,850–7,600	68.3	7,970–7,490	95.4	7,730 ± 250	7,730	Fine seds. below till; max. readvance age
8	ETH-71994	Bivalve shell	2.56	3	2.0	7,920 ± 20	7,630–7,450	68.3	7,740–7,350	95.4	7,540 ± 190	7,540	Fine seds. below till; max. readvance age
9	ETH-67268	Bivalve shell	2.70	3	−13.6	7,705 ± 80	7,470–7,230	68.3	7,580–7,090	95.4	7,340 ± 250	7,350	Fine seds. below till; max. readvance age
10	ETH-67273	Bivalve shell	2.95	1	−4.4	8,005 ± 85	7,750–7,500	68.3	7,900–7,400	95.4	7,630 ± 250	7,630	Fine seds. below till; max. readvance age
11	ETH-67275	Bivalve shell	3.05	1	−12.1	7,950 ± 70	7,680–7,450	68.3	7,810–7,340	95.4	7,570 ± 230	7,570	Fine seds. below till; max. readvance age
12	ETH-67274	Seaweed trash layer	3.05	1	−2.3	8,020 ± 90	7,770–7,510	68.3	7,920–7,410	95.4	7,640 ± 260	7,640	Fine seds. below till; max. readvance age
13	ETH-67276	Bivalve shell	3.10	1	−10.5	8,145 ± 70	7,880–7,640	68.3	7,990–7,530	95.4	7,760 ± 230	7,760	Fine seds. below till; max. readvance age
14	ETH-72000	Bivalve shell	3.11	1	1.3	8,015 ± 20	7,730–7,540	68.3	7,830–7,440	95.4	7,630 ± 200	7,630	Fine seds. below till; max. readvance age
15	ETH-67277	Bivalve shell	3.30	1	−1.0	8,300 ± 75	8,030–7,770	68.3	8,170–7,660	95.4	7,910 ± 260	7,910	Fine seds. below till; max. readvance age

(Continued on following page)

10.3389/feart.2022.1073075

TABLE 2 (*Continued*) Radiocarbon dating results. Samples 1–21 are from the new Pingfo II section (62.2389°S, 58.6729°W), samples 22–25 from the new "Potter Cove" section (62.23895°S, 58.67113°W), 26–27 from the inland outcrop (62.2473°S, 58.6466°W), and 28–30 from the uppermost freshwater subaquatic moss-dominated Unit 3 in the Lake L15-H16 sediment record (62.2405°S, 58.6772°W).

No.	Lab ID	Material dated	Section or core depth (m)	Unit	$\delta^{13}C$ (‰)	AMS ^{14}C age (^{14}C years)	Calibrated age (cal. a BP)		Max.–Min.	2σ %	Mean ± 2σ	Median	Matrix dated, context, interpretation
							Max.–Min.	1σ %					
16	ETH-71996	Bivalve shell	3.41	1	2.9	8,005 ± 20	7,720–7,520	68.3	7,820–7,430	95.4	7,620 ± 200	7,620	Fine seds. below till; max. readvance age
17	ETH-71997	Bivalve shell	3.46	1	0.8	7,995 ± 20	7,700–7,510	68.3	7,810–7,420	95.4	7,610 ± 190	7,610	Fine seds. below till; max. readvance age
18	Beta - 441404	Bone	3.50	1	−23.8	8,100 ± 40	7,820–7,610	68.3	7,930–7,510	95.4	7,720 ± 210	7,720	Fine seds. below till; max. readvance age but possible transport by birds
19	ETH-67278	Bivalve shell	3.50	1	−9	8,090 ± 75	7,830–7,580	68.3	7,950–7,470	95.4	7,710 ± 240	7,710	Fine seds. below till; max. readvance age
20	ETH-72001	Bivalve shell	4.00	1	2.1	7,995 ± 65	7,730–7,500	68.3	7,860–7,400	95.4	7,620 ± 230	7,620	Fine seds. below till; max. readvance age
21	ETH-71995	Bivalve shell	4.47	1	8.0	8,195 ± 25	7,910–7,710	68.3	8,000–7,600	95.4	7,800 ± 200	7,800	Fine seds. below till; max. readvance age
22	SUERC-14413	Seaweed trash layer	2.79#	-	−25.3	7,831 ± 39	7,570–7,370	68.3	7,660–7,260	95.4	7,460 ± 200	7,460	Fine seds. below till; max. readvance age
23	SUERC-14414	Seaweed trash layer	2.79#	-	−25.6	7,883 ± 39	7,610–7,420	68.3	7,700–7,300	95.4	7,510 ± 200	7,510	Fine seds. below till; max. readvance age
24	SUERC-14416	Shell fragment	2.79#	-	1.4	7,853 ± 38	7,580–7,390	68.3	7,670–7,280	95.4	7,480 ± 200	7,480	Fine seds. below till; max. readvance age
25	SUERC-14417	Shell fragment	2.79#	-	0.2	7,842 ± 37	7,570–7,380	68.3	7,660–7,270	95.4	7,470 ± 200	7,470	Fine seds. below till; max. readvance age
S&J	Birm-23	Seaweed trash layer	2.50	C	-	7,863 ± 86	7,460–7,200	68.3	7,570–7,060	95.4	7,320 ± 260	7,330	Fine seds. below till; max. readvance age
S&J	Birm-48a	Shells	2.50	A-B	-	9,670 ± 230	9,900–9,240	68.3	10,220–8,950	95.4	9,570 ± 650	9,560	Fine seds. below till; max. readvance age
26	Beta-441400	Terrestrial moss	2.20	1	−20.9	1,880 ± 30	1,820–1,770	47.4	1,870–1,860	1.8	1,770 ± 80	1,780	Reworked moraine seds.; max. readvance age
	Beta-441400						1,750–1,730	20.8	1,840–1,700	93.7			
27		Terrestrial moss	2.20	1	−22.1	1,850 ± 30	1,810–1,770	23.2	1,830–1,700	84.4	1,740 ± 110	1,740	

(Continued on following page)

10.3389/feart.2022.1073075

TABLE 2 (*Continued*) Radiocarbon dating results. Samples 1–21 are from the new Pingfo II section (62.2389°S, 58.6729°W), samples 22–25 from the new "Potter Cove" section (62.23895°S, 58.67113°W), 26–27 from the inland outcrop (62.2473°S, 58.6466°W), and 28–30 from the uppermost freshwater subaquatic moss-dominated Unit 3 in the Lake L15-H16 sediment record (62.2405°S, 58.6772°W).

No.	Lab ID	Material dated	Section or core depth (m)	Unit	$\delta^{13}C$ (‰)	AMS ^{14}C age (^{14}C years)	Calibrated age (cal. a BP)		Max.–Min.	2σ %	Mean ± 2σ	Median	Matrix dated, context, interpretation
							Max.–Min.	1σ %					
	Beta-441401												Reworked moraine seds.; max. readvance age
	Beta-441401						1,750–1,700	45.1	1,660–1,610	11.1			
28	Beta-384259	Lake L15 Freshwater subaquatic moss	0–.01	2	−22.6	−1,017±21	−43.2–44.4	66.9	−45.1–42.9	66.6	−44.0 ± −1.1	−44.0	Freshwater subaquatic moss in lake seds.
	Beta-384259						−9.1–9.5	26.0	−9.6–9.1	21.2	−9.3 ± −0.3	−9.3	
29	Beta-384260	Lake L15 Freshwater subaquatic moss	0.035–0.04	2	−20.2	−1,213±28	−39.2–41.1	69.5	−38.3–43.1	92.4	−40.7 ± 2.4	−40.7	Freshwater subaquatic moss in lake seds.
	Beta-384260						−9.7–9.8	4.1	−9.9–9.6	4.0	−9.8 ± −0.1	-9.8	
30	Beta-386311	Lake L15 Moss fragments	0.06-0.065	2	*	710 ± 40	660–630	33.6	670–560	95.4	620 ± 70	610	Freshwater subaquatic or littoral moss in lake seds.
	Beta-386311						600–570	34.7					

Samples labeled S&J are from Sugden and John (1973); * indicates data not measurable due to small sample size; # indicates an average depth value. Data output produced in Oxcal v. 4.4 using Marine20 and ShCal20 calibration curves (see Methods) (Bronk Ramsey, 2009).

TABLE 3 Sampling information for cosmogenic ^{3}He nuclide surface exposure dating samples collected around Three Brothers Hill, Potter Peninsula, KGI. All surfaces were dipping less than 10°. Sample 01-Potter, a cobble sitting on top of a morainic crest facing Three Brothers Hill, was taken in its entirety (Supplementary Figure S1). This sample and 05-Potter have a striated, more weathered upper surface, suggesting that it was glacially transported and preserved *in situ*. Samples 02–05-Potter have boulder shapes, sizes, and positions that suggest that a recent turnover would be highly unlikely. Topographic shielding of each sample was measured with a clinometer and compass.

Sample ID	Sample type	Latitude (°S)	Longitude (°W)	*x* (UTM21)	*y* (UTM21)	Elevation (m a.s.l.)[1]	Dimensions (l; w; h) (m)[2]	Thickness (cm)	Topographic shielding correction[3]
01-Potter	Cobble	62.2430	58.6715	413,154	3,097,633	96.6	0.15; 0.25; 0.06	5.6	0.887
02-Potter	Boulder	62.2435	58.6767	412,887	3,097,567	60.8	0.90; 0.50; 0.30	1.7	0.970
04-Potter	Boulder	62.2435	58.6766	412,887	3,097,567	60.9	1.00; 0.45; 0.35	2.2	0.970
05-Potter	Boulder	62.2420	58.6758	412,927	3,097,729	35.0	0.70; 0.70; 0.30	1.3	0.974

TABLE 4 Results of helium measurements at GFZ Potsdam in pyroxene separates from the Three Brothers Hill samples. ^{4}He concentrations are in units of cm^{3} STP g^{-1}, ^{3}He concentrations in atoms g^{-1}; all error limits are 2σ. Erosion rate of 0 and rock density of 2.7 g cm^{-3} were assumed.

Sample ID	Weight (g)[4]	Weight (g)[5]	$^{4}He_{heat}$ (10^{-8})[6]	$^{3}He/^{4}He_{crush}$ (10^{-6})	$^{3}He/^{4}He_{heat}$ (10^{-6})[6]	$^{3}He_{cosmo}$ (10^{6})[7]	Exposure age (ka)[8]	Internal uncertainty (ka)	External uncertainty (ka)
01-Potter	0.827	0.526	45.8 ± 1.6	0.97 ± 0.12	0.129 ± 0.008	1.25 ± 0.32	9.4	2.4	2.6
02-Potter	0.509	0.282	76.4 ± 1.8	0.47 ± 0.03	0.318 ± 0.015	5.96 ± 0.48	41.2	3.3	5.6
04-Potter	0.511	0.426	78.3 ± 2.7	0.44 ± 0.06	0.261 ± 0.015	4.91 ± 0.62	34.1	4.3	5.7
05-Potter	0.985	0.656	38.6 ±1.3	1.62 ± 0.26	0.283 ± 0.016	2.64 ± 0.29	18.6	2	2.9

TABLE 5 Data for each heating step. The total $^{3}He_{cosmo}$ concentrations have been calculated by summing the ^{3}He excesses from all heating steps. [1]Altitudes were measured with a Differential GPS Trimble Pathfinder ProXH. Accuracy of 10 cm in all axes. [2]The height (h) of the sample means cm above the moraine surface. [3]Calculated using the online geometric shielding calculator v1.1 (http://hess.ess.washington.edu/math/general/skyline_input.php; Balco et al., 2008). [4]99% of the weight of the separates was pyroxenes. The rest is composed of olivine grains. [5]Weight of the samples used for stepwise heating extraction. [6]Sum of all heating steps in (C). [7]Calculated from $^{3}He_{cosmo} = {}^{4}He_{heat} \times ({}^{3}He/{}^{4}He_{heat} - {}^{3}He/{}^{4}He_{rad})$, assuming $^{3}He/^{4}He_{rad} = (0.028 \pm 0.028) \times 10^{-6}$. See the text for an explanation of the calculation method. [8]Obtained using the online calculator CRONUScalc v2.0 (http://cronus.cosmogenicnuclides.rocks/2.0/; Marrero et al., 2016), using the primary calibration dataset for ^{3}He in pyroxene (Borchers et al., 2016) and the time-dependent Lal (1991)/Stone (2000) scaling model (Lm) and SLHL scaled production rate of 122 ± 13 atoms g^{-1} yr^{-1} (Borchers et al., 2016).

Sample ID	T°C	$^{4}He_{heat}$ (10^{-8})	$^{3}He/^{4}He_{heat}$ (10^{-6})	$^{3}He_{cosmo}$ (10^{6})	$^{4}He_{heat}$ (10^{-8}) Total	$^{3}He/^{4}He_{heat}$ (10^{-6}) Total	$^{3}He_{cosmo}$ (10^{6}) Total
01-Potter	900	39.9 ± 1.6	0.106 ± 0.008	0.84 ± 0.31			
	1,750	5.93 ± 0.24	0.288 ± 0.034	0.41 ± 0.07	45.8 ± 1.6	0.129 ± 0.008	1.25 ± 0.32
02-Potter	600	30.9 ± 1.2	0.195 ± 0.016	1.39 ± 0.27			
	900	29.9 ± 1.2	0.385 ± 0.028	2.87 ± 0.34			
	1,750	15.62 ± 0.63	0.433 ± 0.038	1.70 ± 0.21	76.4 ± 1.8	0.318 ± 0.015	5.96 ± 0.48
04-Potter	900	67.6 ± 2.7	0.244 ± 0.016	3.93 ± 0.60			
	1,750	10.71 ± 0.43	0.367 ± 0.036	0.98 ± 0.14	78.3 ± 2.7	0.261 ± 0.015	4.91 ± 0.62
05-Potter	900	29.9 ± 1.2	0.215 ± 0.016	1.50 ± 0.26			
	1,750	8.72 ± 0.35	0.515 ± 0.041	1.14 ± 0.12	38.6 ±1.3	0.283 ± 0.016	2.64 ± 0.29

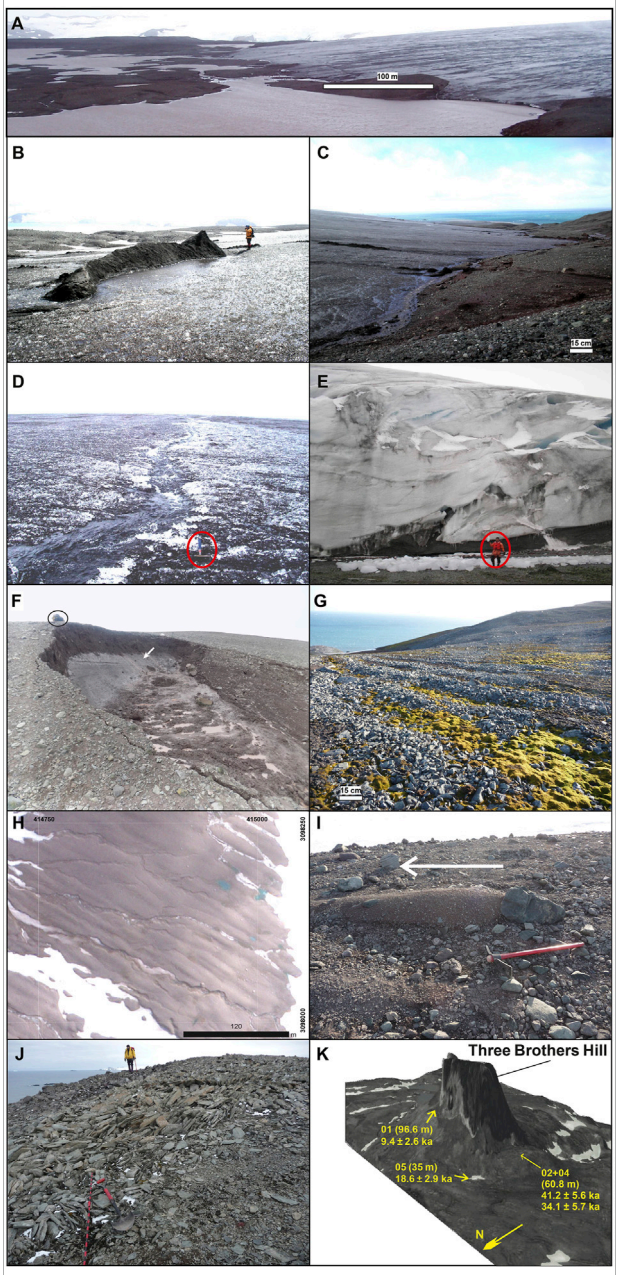

FIGURE 4
Examples of the active glacial landform assemblages of the Warszawa Icefield on Potter Peninsula: **(A)** Transverse structures and radial longitudinal foliation. **(B,C)** Transverse foliation related to englacial thrusts and longitudinal foliation associated with melt-out till on the ice surface on the Warszawa Icefield foreland. **(D)** A supraglacial meltwater channel. **(E)** Folded layers of subglacial debris in the snout of the icefield, toward the Fourcade Glacier. Components of the glacial and periglacial landform assemblages observed on Potter Peninsula. **(F)** Slump on glacial deposits showing the collapsing ice-cored moraine (white arrow) at the Warszawa Icefield foreland; bag on top as scale. **(G)** Vegetated large stone stripes above Stranger Point. **(H)** Satellite image showing flutings in recently deglaciated glacial deposits, being eroded by glaciofluvial activity. **(I)** Flutes at a smaller scale, indicating former ice movement direction. **(J)** Frost-shattered bedrock covered to some extent with lichens. **(K)** Summary of ^{3}He cosmogenic nuclide surface exposure ages from the Three Brothers Hill area superimposed on a satellite image drape on the KGI-DEM. See Tables 3–5 and Supplementary Material for details.

Wavelength Dispersive Spectroscopy, WDS-XRF, and dry subsample analysis (Kylander et al., 2011; Davies et al., 2015; Roberts et al., 2017; Dunlea et al., 2020). Data were filtered to remove the small number of downcore spectra with kcps less than the mean minus two-SD, caused mainly by small gaps in the core, and MSE values greater than mean plus four-SD, which represents a poor fit of the measured to theoretical energy spectra. "Measurable" elements were determined by autocorrelation, with significant zones, and their boundary positions, defined by constrained cluster analysis (CONISS) with broken stick analysis applied to square-root-transformed %TSN values of key elements using the R packages Vegan and Rioja (Juggins, 2012; Oksanen, 2014).

Hyperspectral image (HSI) scanning analysis, which measures reflected optical properties between wavelengths from 400 to 1,000 nm (Butz et al., 2015), was undertaken at the University of Bern using the Specim Ltd. single core scanner (PFD-CL-65-V10E line scan camera, 400–1,000 nm) following the protocol of Butz et al. (2015). The spatial resolution (pixel size) was set at 69 × 69 µm, and the spectral resolution is 2.8 nm sampled at an interval of 0.78 nm. Raw data were normalized with a BaSO4 reference, and spectral endmembers were calculated using the software ENVI 5.03. Quantitative estimates of pigments were obtained using the Relative Absorption Band Depth (RABD) method, which uses ratios and normalized reflectance data from distinct wavelengths. The spectral index RABD660;670 (RABD at 660–670 nm) was calculated from the continuum between 590 and 730 nm (Butz et al., 2015) with I-band wavelengths between 660 and 670 nm using equations RABD660;670 = (6*R590+7*R730)/13/Rmin(660;670) and RABD660;670 [I-Band] = (6*R590+7*R730)/13/Rmin(660;670)/Rmean (Rein and Sirocko, 2002). The spectral index RABD660;670 is proportional to the concentration of sedimentary chlorophyll-a, chlorophyll-b, and related colored diagenetic pheopigments (referred to as total chlorophylls TChl), which are generally interpreted as aquatic primary production indicators (Leavitt and Hodgson, 2001; Butz et al., 2017; Schneider et al., 2018; Makri et al., 2020).

3.4 Chronology and chronostratigraphy

3.4.1 Radiocarbon dating

Twenty-one accelerator mass spectrometry (AMS) radiocarbon (^{14}C) ages were obtained from seaweed, marine mollusc shells, penguin bones, bones from undetermined

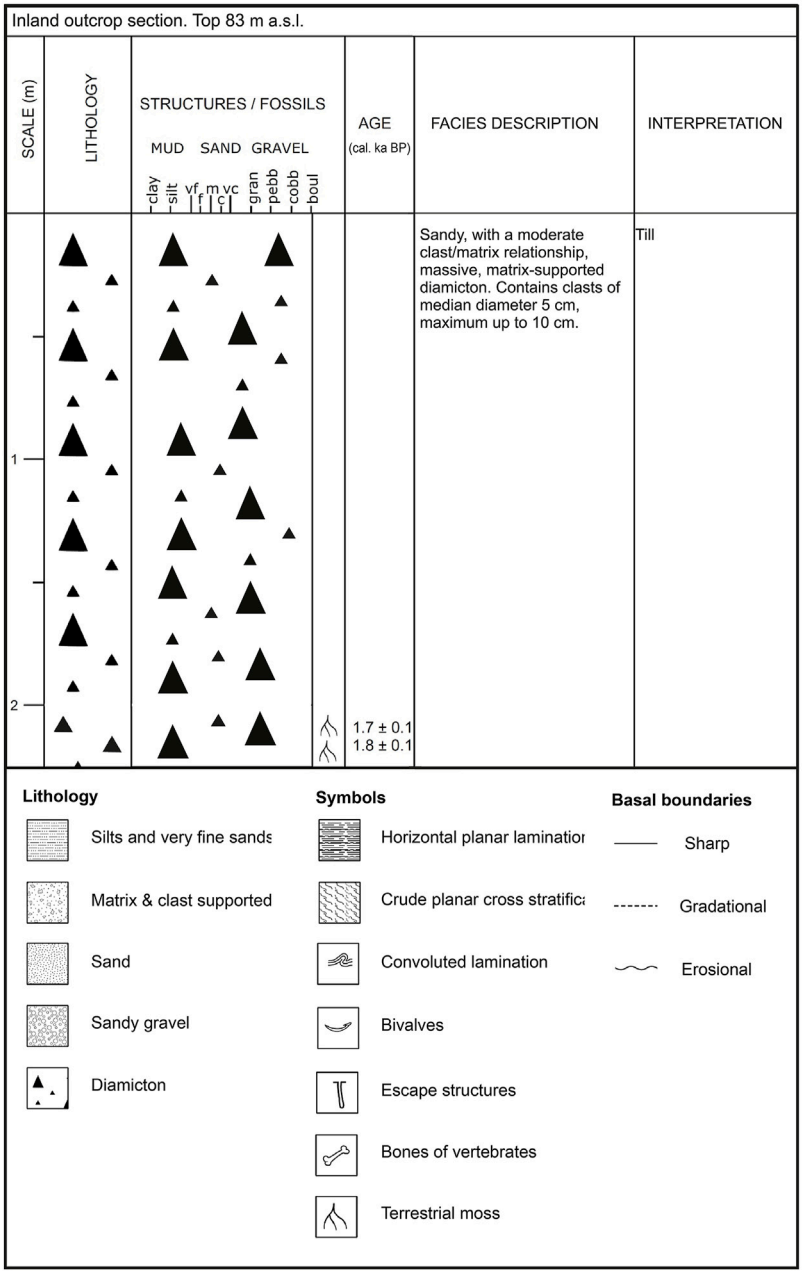

FIGURE 5
Stratigraphic profile of recently exposed (2013 CE) "Inland Outcrop" glacial deposits, location 3 in Figure 3.

species, remnants of terrestrial mosses embedded in marine coastal proximal and terrestrial moraine sediments, and freshwater subaquatic moss in the uppermost unit (0–6 cm depth) of the Lake L15-H16 (Figure 3E; Supplementary Figure S6; Table 2). In order to reduce the risk of contamination with modern material, samples for radiocarbon dating from the stratigraphic sections were taken from freshly cleaned outcrops and stored in zip-lock plastic bags at 4°C. Samples were prepared at the Alfred Wegener Institute Helmholtz Centre for Polar and Marine Research, Durham University, and the British Antarctic Survey. AMS and $^{13}C/^{12}C$ isotope ratio measurements undertaken at ETH Zürich, the NERC Radiocarbon Laboratory, East Kilbride, and by Beta Analytical, Miami, were used to calculate conventional radiocarbon ages following established procedures (^{14}C years; Table 2; Supplementary Material for details).

Calibration of marine sample radiocarbon ages (marine shells, penguin bones, bones from undetermined species, and

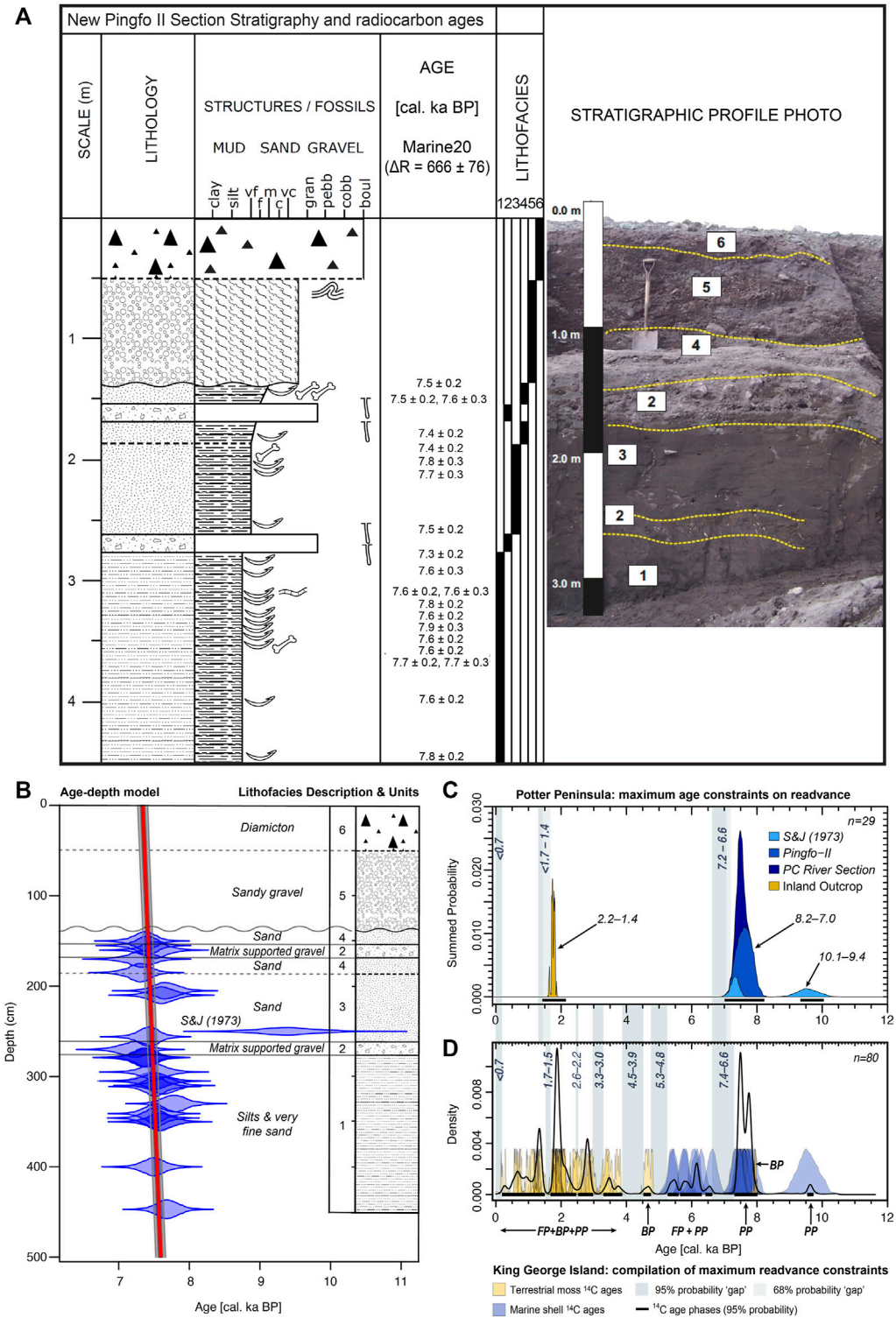

FIGURE 6
(A) Stratigraphic profile and photograph of the new Pingfo II section. Lithofacies units 1–6 shown in the photo are described in the main text. Legend is as shown in Figure 5. **(B)** Bayesian (BACON) age-depth model for the new Pingfo II and River Cut sections showing that new radiocarbon age data are broadly in stratigraphic order, with mean values clustering between 7.8 and 7.5 cal. ka BP (8.0–7.0 cal. ka BP 95% probability density age range). The older age range of 10.1–9.4 cal. ka BP (95% probability density age range) is based on ages reported by Sugden and John (1973) and is a clear outlier. Lithofacies units 1–6 are as shown in **(A)**. See Table 2 for radiocarbon data. **(C)** Summed probability profile of new radiocarbon age data from Potter Peninsula in this study compared with previously published data (S&J, Sugden and John, 1973) in Table 2. **(D)** Probability density phase model of maximum age constraints on glacier readvance on King George Island between 12 and 0 cal. ka BP. Dark and light grey shaded zones in **(C,D)** are 95% probability "gaps" when glacier readvances could have occurred. BP, Barton Peninsula; FP, Fildes Peninsula; PP, Potter Peninsula.

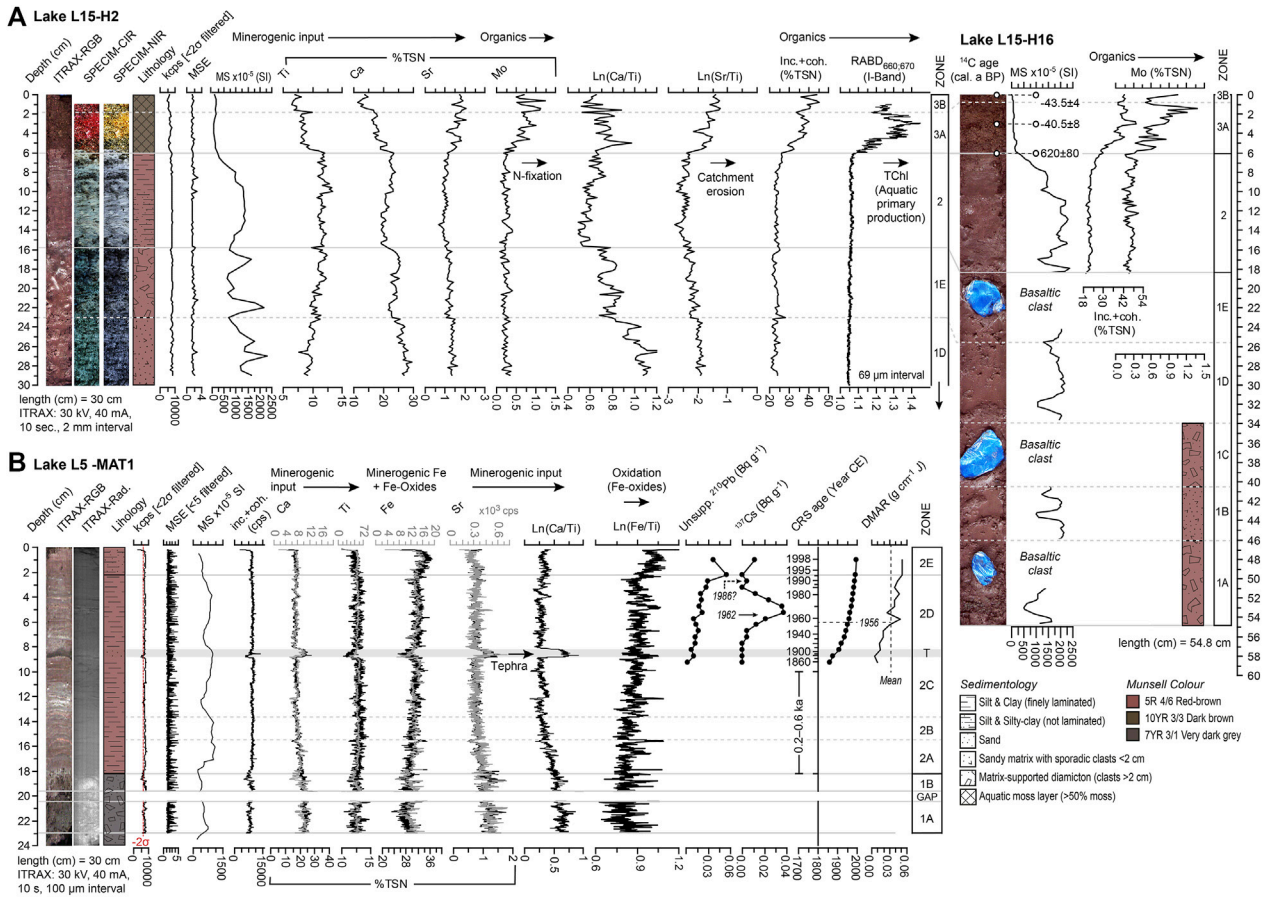

FIGURE 7
Summary lithological, ITRAX XRF-CS, SPECIM hyperspectral imagery and data, and chronological data from sediment records from **(A)** Lake L15 and **(B)** Matias Lake (ML; L5). A positive correlation between the RABD660;670 (reflecting increased organic productivity) and the XRF-CS molybdenum (Mo) and total scatter profiles in Lake L15 exists because Mo improves the efficiency of nitrogen fixation and the nitrogenase creation process by binding with organic ligands (e.g., tannins) in near-surface and sub-aquatic environments (including freshwater moss) and iron oxides and organic matter at depth, preventing it from leaching out of the sediment (Wichard et al., 2009). Conversely, Mo has very low concentrations in mineral-rich sediments as Mo attachment to mineral grains is an insignificant process. Total scatter (inc. + coh.) and scatter ratios (inc./coh.) are also elevated in organic matter as it is less dense and has a higher water content than minerogenic sediments (Davies et al., 2015).

seaweed) was undertaken in Oxcal v. 4.4 using the Marine20 calibration curve (Gordon and Harkness, 1992; Bronk Ramsey, 2009; Heaton et al., 2020, 2022). We used a newly recalculated local marine reservoir age offset (ΔR) of 666 ± 76 ^{14}C years that represents the weighted mean ΔR of the four closest and most applicable radiocarbon-dated marine samples collected before 1950 CE from the northern AP and Signy Island in the online Marine20 database (http://calib.org/marine/) (Table 2; Supplementary Material for details). Terrestrial and freshwater subaquatic moss samples were calibrated using the Southern Hemisphere SHCal20 (Hogg et al., 2020) calibration curve in Oxcal v. 4.4 (Bronk Ramsey, 2009). Post-bomb (>1950 CE) ages were corrected according to ^{13}C/^{12}C isotopic ratios from measured pMC with the "present day" pMC value defined as 107.5% (2010 CE) and calibrated using the SHCal13 SH Zone 1-2 Bomb curve in CALIBomb (Reimer and Reimer, 2004; Hua et al., 2013). Median and mean calibrated ages and their 2σ (95.4% confidence level) maximum to minimum error ranges are presented as thousands of years before the present (cal. ka BP). Calibrated ages have been rounded to the nearest 10 years in Table 2 and to the nearest hundred years in the text to reflect realistic total (i.e., all internal and external) uncertainties. Post-bomb ages are presented as year CE and have been rounded to the nearest year.

Bayesian age-depth models for the new Pingfo II sedimentary sequence and the lake sediment records were constructed using the Bacon R package (Blaauw and Christen, 2011) (Figure 6B; Supplementary Figure S5). Summed probability density analysis of the new Potter Peninsula radiocarbon data was undertaken using the Rcarbon package v. 1.4.2 (Bevan, 2021) and compared

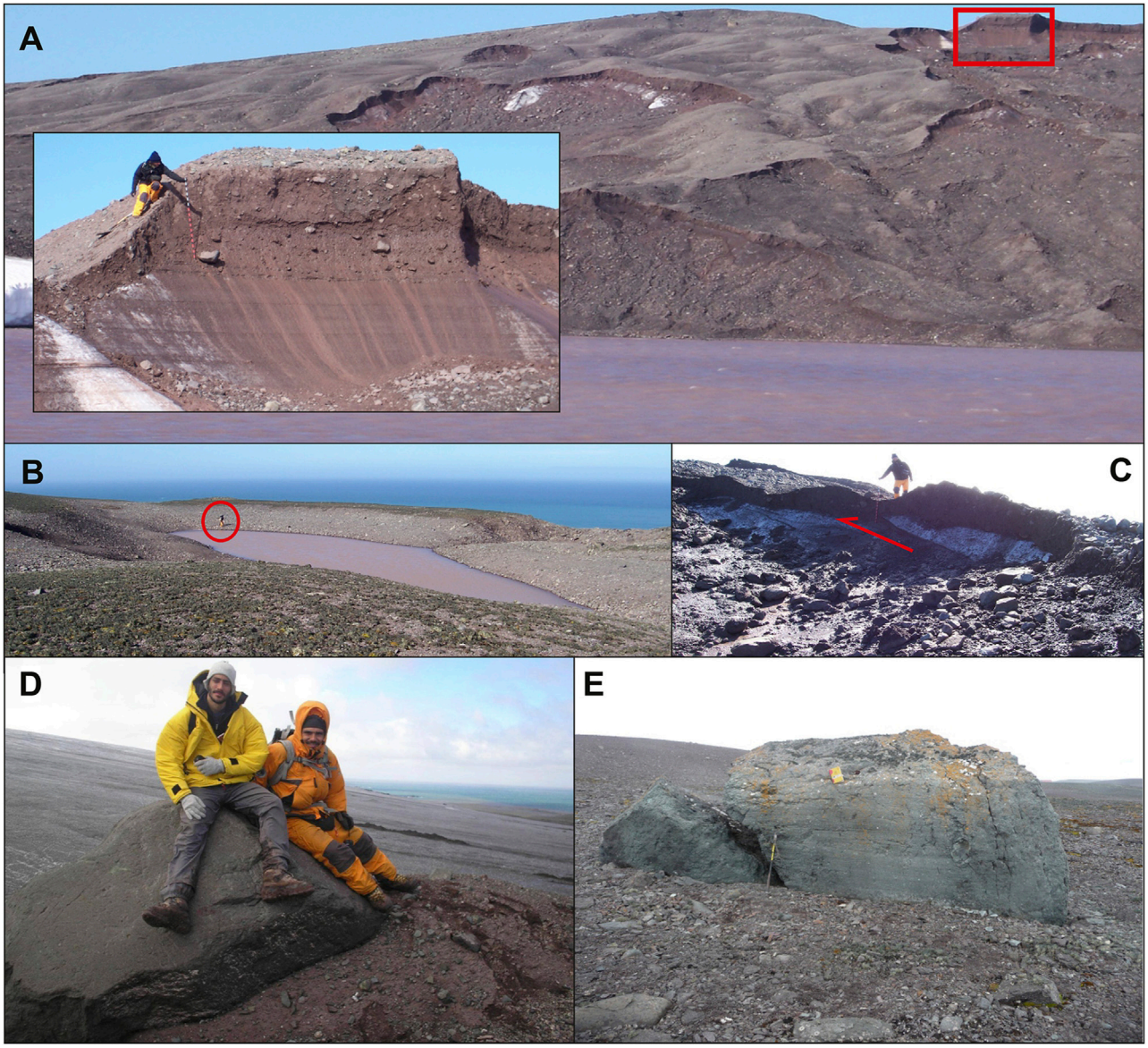

FIGURE 8
The Stranger Point and Three Brothers Hill moraine landform assemblage and inactive Holocene glacial landforms that have collapsed due to thermoerosion. **(A)** Debris flows and slumps are reworking the moraine, showing its ice core. **(B)** A pond bordered by prominent moraine ridges. **(C)** A moraine thrust in the direction of the red arrow and mudflows at the foot of the ice-cored moraine. **(D)** Striated and polished basaltic boulder on the moraine, deposited by thrusting. **(E)** Polished and striated block in the surroundings of Three Brothers Hill.

to non-parametric phase modeling (i.e., a probabilistic version of the Oxcal SUM command) using the Bchron v. 4.7.6 R package (Haslett and Parnell, 2008; Parnell, 2021). New radiocarbon data from Potter Peninsula were then incorporated into a new compilation of existing maximum age constraints on glacier readvance from across KGI, and non-parametric phase modeling was undertaken (Figures 6C, D).

3.4.2 Lead-210 (^{210}Pb), caesium-137 (^{137}Cs), and americium-241 (^{241}Am) analysis

^{210}Pb 137Cs and ^{241}Am dating of the uppermost 10 cm of the lake sediment records was undertaken using ~4 g of homogenized dried sediment, added into tubes to a predefined level and sealed gas tight. After at least 21 days of storage to obtain radioactive equilibrium between ^{226}Ra and ^{222}Rn, activities

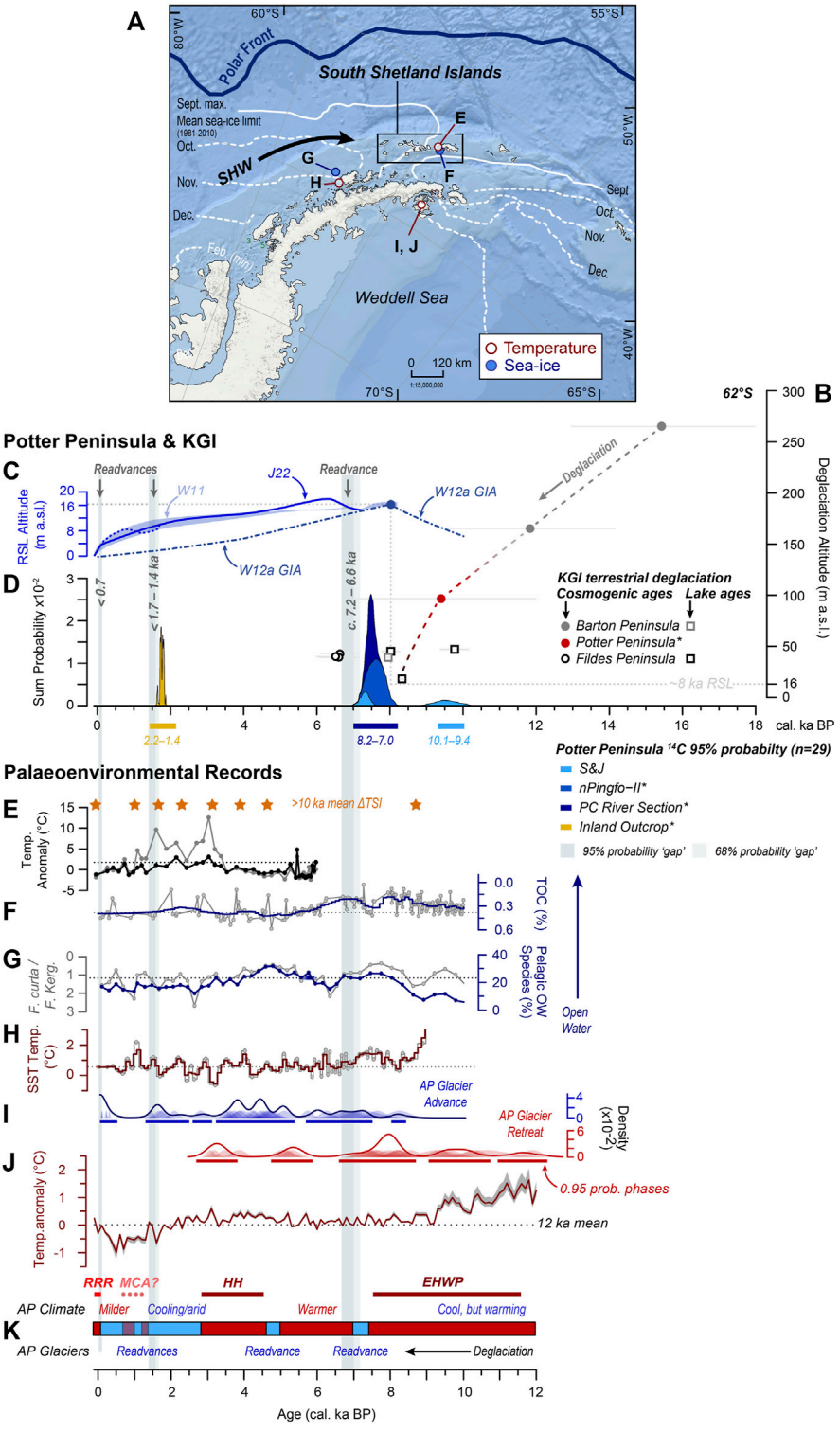

FIGURE 9
(A) Location map for palaeoenvironmental records in this figure. SHW, Southern Hemisphere Westerly winds. Letters correspond to the records shown below. Dashed white lines are mean modern-day sea ice data (NSIDC 1981–2010 CE; 20% sea ice coverage from https://nsidc.org/data/seaice_index/) Austral summer minimum (February or Feb.) and winter maximum (September or Sept.) sea ice limits (solid white lines). The minimum (Feb.) sea ice extent on the western side of the AP is located off-image further south of the December (Dec.) sea ice extent. **(B)** Cosmogenic nuclide exposure ages and key lake basal ages constraining deglaciation on KGI at different altitudes from Barton Peninsula (Seong et al., 2008; Oliva et al., 2019), Potter Peninsula (this study), and Fildes Peninsula (Watcham et al., 2011); *, new data (this study). Basal lakes ages constraining early
(*Continued*)

FIGURE 9 (Continued)
Holocene deglaciation were not obtained from lakes cored on Potter Peninsula as they contained an impenetrable diamicton layer likely due to mid-late Holocene readvances on Potter Peninsula. **(C)** Summarized relative sea level (RSL) envelope for the SSI (W11, light blue shading; Watcham et al., 2011) compared with the RSL curve by Johnson et al. (2022) (J22, dark solid and dotted blue lines) and the W12a GIA model (Whitehouse et al., 2012a, b); see original references for further details and data. **(D)** Summed probability profiles and phases (bars) derived from new radiocarbon ages from Potter Peninsula in this study compared with previously published radiocarbon data (S&J, Sugden and John, 1973); readvances shown as vertical grey shaded zones are constrained by data in this plot and Figures 6C, D). **(E)** Glycerol dialkyl glycerol tetraether (GDGT)—mean summer air temperature (MSAT) anomaly reconstruction (dark grey line) from the Yanou Lake sediment record, Fildes Peninsula (Foster et al., 2016; Roberts et al., 2017); the black line and data points represent a revised MSAT anomaly reconstruction for Yanou Lake based on combining the Pearson et al. (2011) and Foster et al., 2016) datasets (RMSE = 1.65°C). These new values and their 6 kyr mean ± 1σ MSAT anomaly of 0.06 ± 1.50°C are more realistic than previous values (Roberts et al. (2017): dark grey line and data points); orange stars are ΔTSI peaks greater than the mean Holocene ΔTSI values, see Figure 10A; the dotted line is the 6 ka mean MSAT anomaly for the dataset published in Roberts et al. (2017). **(F)** Maxwell Bay TOC (total organic carbon; grey data points and line; dark blue line is a 100-year interval LOESS regression) with lower values interpreted by Milliken et al. (2009) as reduced sea ice concentration and more open water. **(G)** Anvers Shelf diatom-based sea ice reconstruction. Lower ratio values represent reduced sea ice concentration and higher pelagic percentage values reflect increased open water (OW) (Roberts et al., 2017). **(H)** SST reconstruction from the Palmer Deep (Shevenell, et al., 2011; Etourneau et al., 2013). **(I)** Probability density phase analysis applied to glacier advance (blue) and retreat (red) data in Kaplan et al. (2020) from the northern Antarctic Peninsula. **(J)** Temperature anomaly data from the James Ross Island (JRI) ice core record, NE Antarctic Peninsula (Mulvaney et al., 2012; errors <±10% not shown for clarity). **(K)** Summary climate syntheses for the Antarctic Peninsula (based on Ingólfsson et al., 2003; Bentley et al., 2009; see Supplementary Figure S7 for an extended version). EHWP, Early Holocene Warm Period; HH, Holocene Hypsithermal; MCA, Medieval Climate Anomaly; RRR, Recent Rapid Regional warming (after Bentley et al., 2009).

of radionuclides were measured by well-type gamma spectrometry (Ge-detector, GWC 2522-7500 SL, Canberra Industries Inc., United States) and processed with GENIE 2000 3.0 (Canberra Industries Inc., United States). Data analysis and dating model calculations followed standard procedures defined by Appleby and Oldfield (1978). Lead-210 age estimates were derived using the constant rate of supply (CRS) method (Appleby and Oldfield, 1978) and incorporated into Bayesian age-depth models (Figure 6B; Supplementary Figure S5) (Supplementary Material for details).

3.4.3 Cosmogenic helium-3 (^{3}He) nuclide surface exposure dating

Stable cosmogenic ^{3}He accumulates in pyroxene and olivine phenocrysts in the upper few cm of basaltic boulders on the Three Brothers Hill moraine system, recording the total time that the rock surface has been exposed to cosmic rays. Using a hammer and chisel to remove the upper few centimeters of exposed surfaces, we collected five samples from boulders perched on moraines between 35 and 100 m a.s.l. (Supplementary Figure S1). The sampled boulders were >50 cm in diameter and the most suited for cosmogenic dating analysis as they showed no signs of sediment cover or significant erosion. Their size and shape meant it was very unlikely they had been overturned, and post-depositional movement was minimized by sampling boulders on locally flat and stable surfaces, away from steep slopes and cliffs (Supplementary Figure S1). Differential GPS (dGPS) measurements were undertaken using a Trimble Pathfinder ProXH to determine the precise location and altitude of boulders in relation to the DALL 66019M002 (S62°14′16.335″, W58°39′52.364″, ellipsoidal height 39.376 m) triangulation station located on the Argentine Carlini base, a few hundred meters away from the sampled erratics (Table 3). dGPS precision is better than 10 cm in all axes, but ellipsoid correction errors are larger.

Sampling and processing methods are described in Tables 3–5 and in detail in the Supplementary Material. Exposure ages were calculated using the CRONUScalc calculator (Version 2.0; Marrero et al., 2016) with the time-dependent Lal (1991)/Stone (2000) scaling model (Lm) for altitude at Antarctic pressure conditions and the primary calibration dataset for ^{3}He in pyroxene, which yields a long term sea-level high latitude (SLHL) scaled production rate of 122 ± 13 at g^{-1} a^{-1} (Borchers et al., 2016). We report internal and external uncertainties in Table 4. External age uncertainties include production rate uncertainties, and exposure ages determined with other scaling models (e.g., Lifton et al., 2014) vary by up to ~6%. Following Balco et al. (2008), external uncertainties are used for comparison with calibrated AMS radiocarbon ages and error ranges.

All statistical analysis was undertaken, and figures were constructed using R v. 4.1.0/RStudio v. 1.4.1717 and packages Tidyverse, ggplot2, Vegan, Rioja, Ggally v. 2.1.2, RBacon, Rcarbon, Bchron, and Sigmaplot v. 14.0, C2 (Juggins, 2007), with final figure layouts achieved in Adobe Illustrator v. 26.2.1 or CorelDRAW v. 2020.

4 Results

We identified four distinct altitudinal and glacially impacted environments on Potter Peninsula: 0–15 m a.s.l. (Holocene-age and active beaches); 15–50 m a.s.l. (vegetated (perma)frost-affected bedrock plateaus); 50–100 m a.s.l. (fresh-looking, recent glacial deposits); >100 m a.s.l. (Three Brothers Hill) (Figure 2).

To provide a process-oriented, land systems-based assessment, we divided our new geomorphological map of the Potter Peninsula in Figure 2 into the following four sediment-landform assemblages (LA):

LA-1: glacier ice and snow, active glacial sediment landforms.
LA-2: glacial assemblage of inactive glacial landforms and deposits.
LA-3: paraglacial and proglacial assemblage, marine/alluvial landforms, and deposits.
LA-4: periglacial assemblage, hillslope, and structural landforms and deposits.

The main features of these landform assemblages are summarized and interpreted in Table 1 and illustrated in Figures 3–5. In the following sections, we have organized results obtained from the stratigraphic sections, lake records, and chronological analysis according to the landform assemblages described above.

4.1 Landform assemblage LA-1: Active glacial sediment landforms

4.1.1 Inland Outcrop on the recently deglaciated inner Warszawa Icefield foreland

The contact between the Warszawa Icefield and its proglacial area is shallow and contains many active glacial sedimentary landforms (Figure 4A; Table 1; Section 1 for further details). In 2013, we discovered a new exposure ~700 m away from the present-day glacier limit (62.2473°S, 58.6466°W). This "Inland Outcrop" is a partly degraded, non-vegetated, 2.3 m thick massive matrix-supported sandy diamicton. Two radiocarbon ages from basal moss fragments incorporated into the base of a diamicton have mean ± 2σ ages of 1.7 ± 0.1 and 1.8 ± 0.1 cal. ka BP, with a density phase model 95% probability range of 2.2–1.4 cal. ka BP (Figures 5, 6; Table 2, nos. 26, 27). This section represents glacier bulldozing of moss that grew on previously glacier-free areas, and the youngest of the moss radiocarbon ages provides a maximum age constraint on glacier readvance across the mid-upper glacier foreland.

4.2 Landform assemblage LA-2: Inactive glacial assemblage

4.2.1 Stratigraphic river sections from northern mid-outer Potter Peninsula

The new Pingfo II (nPII) section (62.2389°S, 58.6729°W; Figure 2A and Location 1 in Figure 3) and "Potter Cove" (PC) river sections (62.23895°S, 58.67113°W; Figure 2 and Location 2 in Figure 3) are part of a small lateral moraine ridge running obliquely to the southern coastline of Potter Cove.

The nPII section is composed of five units of shell-bearing marine sand, and terrestrial sand, sand gravel and gravel (Lithofacies 1–5 in Figure 6A) overlain by a sandy diamicton unit composed of matrix-supported pebble to cobble-sized clasts (Lithofacies 6; Figure 6A) as follows: Lithofacies 1 is a laminated silt/very fine sand with remnants of shells of bivalve *Laternula elliptica* and algae; Lithofacies 2 are composed of beds of massive, matrix to clast supported gravels, ~10–15 cm thick, with subangular to angular clasts up to 5 cm embedded in a sandy matrix; Lithofacies 3 is composed of horizontally laminated very fine to silty sand, with brownish-to-orange algae and shelly remains with sporadic subangular clasts up to 7 cm; Lithofacies 4 is composed of horizontally laminated fine-to-medium sand, with silty-clay and sporadic sub-angular clasts up to 10 cm, shells of *Laternula elliptica*, penguin bones, and a distinctively compacted brownish (algae) deposit at 1.60 m covering fine pebbles; Lithofacies 5 is a stratified matrix and clast-supported gravel intercalated with sand and laminated silt, subrounded and subangular clasts up to 10 cm and larger "dropstones" up to 30 cm diameter and has a contorted upper boundary; Lithofacies 6, which is a sandy-clay, matrix-supported, clast rich, massive to weakly laminated diamicton, with striated angular to sub-angular clasts up to 50 cm. The upper surface of the nPII and PC sections is a flat terrace at 6 m a.s.l. littered with larger clasts on the surface facing Potter Cove and forms part of the inactive vegetated glacial assemblage (Figures 3, 6A; Table 1).

Twenty-one samples analyzed for AMS radiocarbon dating included remains of different marine organisms, seaweed, with *Laternula elliptica* shells and bones (Figure 6A; Table 2, nos. 1–21). Their mean and median calibrated radiocarbon ages cluster between 7.7 and 7.2 cal. ka BP, with a density phase model 95% probability range of 8.2–7.0 cal. ka BP. Shells in the lowermost sand unit are small fragments and unlikely to be *in situ* but also imply that the intertidal sand was accumulating in the range of c. 8.2–6.9 cal. ka BP (2σ calibrated age range). All new ages obtained from the nPII section are distinct (at 95% probability) from older radiocarbon ages of similar marine shells measured by Sugden and John (1973) with a density phase model 95% probability range of 10.1–9.4 cal. ka BP (Figure 6C; Table 2). Bayesian age-depth modeling shows that deposition of Lithofacies 1–4 was broadly in stratigraphic order, with a homogenous sedimentation rate of ~10 mm a-1 (Figure 6B).

Four new AMS radiocarbon ages from marine shells, and a ~2–10 mm thick filamentous seaweed (brown algae) layer collected from between the marine sand unit and the overlying diamicton in the nearby PC river section (Table 2, nos. 22–25; Figure 6C), were dated independently and had mean calibrated ages of c. 7.5 ± 0.2 cal. ka BP, respectively (2σ range 7.7–7.0 cal. ka BP) (Table 2). Their density phase model 95% probability age range is in close agreement with new ages from the nPII section (Figures 6B, C).

4.2.2 Lake sediment records from the central mid-outer area of Potter Peninsula

Lake L5 (Matias Lake): we extracted 13 short cores from the depocentre in Matias Lake and along a surface transect toward Rudy Lake. Sediment recovery depth ranged 20–60 cm before encountering an impenetrable diamicton layer. Cores MAT1

(L5-H1) (27 cm) and MAT2 (L5-H2) (29 cm) in Figure 7 were extracted from the deepest part of Matias Lake (5.8 m; 62° 14′ 42.054″S, 58° 39′ 53.82″W; Figure 2; Supplementary Figure S2). Two lithological zones were present across all cores. The basal zone 1 diamicton was predominantly matrix-supported, largely impenetrable, and only retained in some cores. The overlying sediments in zone 2 are composed of fine (mm scale) grey silty clay and Fe-rich orange clay laminations, probably reflecting periodic (possibly even seasonal) overturning and/or oxidation processes within the lake and glaciolacustrine deposition following the retreat of the Warszawa Icefield landward from Matias Lake and Rudy Lake (Figure 7B).

Obtaining basal radiocarbon ages from basal and bulk minerogenic sediments in the Matias Lake cores proved challenging due to a general lack of organic carbon (Figure 7; Supplementary Figures S5, S6; Table 2). The ^{210}Pb CRS age model shows that the uppermost 10 cm have been deposited since c. 1850 CE, and the well-defined ^{137}Cs peak at 5 cm depth is coherent with the ^{210}Pb age model (Figure 7B; Supplementary Table S2). A 0.5 cm thick tephra deposit between 8 and 9 cm depth (1908 ± 10 CE) is characterized by elevated Ca and Sr and most likely represents an early C20th eruption from Deception Island, 120 km southwest of Potter Peninsula.

Lake L15 (GPS Lake): we extracted eight cores from a grid of 25 (~1 m spaced) holes drilled through the ~75–100 cm thick lake ice above the deepest accessible point (~2 m) at Lake L15. Core L15-H2 (62° 14′ 26.052″S, 58° 40′ 39.36″W) in Figure 7A contained 30 cm of sediment, L15-H4 11 cm, L15-H9 39 cm, L15-H16 55 cm (62° 14′ 26.016″S, 58° 40′ 39.252″W; Figure 7A), L15-H17 45 cm, L15-H19 34 cm, L15-H20 61 cm, and L15-H22 49 cm. The same three lithological zones exist in all records. Zone 1 is a fine silt/clay matrix-supported diamicton, zone 2 is a fine silt/clay laminated sediment, and zone 3 is a freshwater subaquatic moss. Hyperspectral and XRF-CS profiles show that zones 1 and 2 have very low primary productivity (Figure 7A), with the transition to elevated RABD660; 670 values into zone 3 reflecting increased active photosynthesis by subaquatic moss and higher subaquatic primary production. zone 3A shows a maximum concentration of TChl, which remains high in zone 3B, but with relatively lower TChl concentrations. This relative decrease might also be related to higher lithogenic sedimentation rates and/or greater porosity.

Radiocarbon ages of freshwater moss and macrophytic material from the uppermost lithological Unit 3 in Lake L15 range from post-1950 CE to c. 0.6 cal. ka BP and are statistically distinct from ages obtained from terrestrial moss layers embedded in the "Inland Outcrop" (Figures 2A, 3B, 7; Supplementary Figure S6; Table 2). The Lake L15 ^{210}Pb Constant Rate of Supply (CRS) age model has a low sedimentation rate in the top 10 cm, and the sample at ~4–5 cm is at least 150 years old (Supplementary Table S3). Although the prerequisite for the CRS model was not fulfilled because the flux of ^{210}Pb has changed through time and is not constant, the ^{210}Pb data are consistent with the radiocarbon ages that show sediment between 6 and 6.5 cm dates to 620 ± 80 cal. a BP, and 3–3.5 cm and 0–0.5 cm depth were deposited in the "post-bomb" (post-1950 CE) era, most likely between −40 and −44 cal yr BP (1990–1994 CE) (Figure 7; Table 2; Supplementary Table S5). The ^{137}Cs data are inconsistent with the ^{210}Pb CRS age model (Supplementary Table S3), and the steep increase in ^{137}Cs in the upper 2 cm may relate to a ^{137}Cs "soil reservoir," which is leaching ^{137}Cs from the catchment into the lake from snow or lake-ice melting.

4.3 Landform assemblages LA-2, LA-3, and LA-4

4.3.1 Stranger point and three brothers hill moraine systems and associated proglacial/periglacial landforms and deposits

Well-preserved morainic crests and glacial erratics are rare in the Three Brothers Hill moraine system mainly because the moraines have been heavily degraded into debris flows and are now covered in talus rock accumulations (Table 1; Figure 8; Supplementary Figure S1).

We sampled erratics firmly embedded on the moraine for He-3 cosmogenic nuclide exposure dating to minimize the effect of post-depositional movement. In summary, ages are scattered between 9.4 ± 2.6 ka and 41.2 ± 5.6 ka (Figure 4K; Supplementary Figure S1; Table 4) and have external uncertainties up to 28% (e.g., sample 01-Potter, Table 4). The two youngest ages from boulders 01-Potter (9.4 ± 2.6 ka) and 05-Potter (18.6 ± 2.9 ka) had striated surfaces indicative of glacial transport and *in situ* preservation (Table 4). The large age scatter in the ^{3}He cosmogenic nuclide exposure ages and the large individual age errors are due to the low concentration of cosmogenic helium and/or the poorly known ^{3}He/^{4}He ratio of the non-cosmogenic component. The possibility of previous exposure and complex and poorly understood nuclide inheritance processes cannot be excluded either. Therefore, we consider the ^{3}He cosmogenic nuclide exposure results to be promising but tentative.

5 Discussion

Based on our new geomorphological map and our assessment of the landform assemblages on Potter Peninsula, we propose the following five-stage deglaciation landscape evolution model for Potter Peninsula during the Holocene:

(1) Early Holocene terrestrial deglaciation began, and a glacier-free environment existed at a low altitude in the mouth of Potter Cove before 8.2 cal. ka BP;
(2) Deglaciation was interrupted by a readvance that reached outer Potter Cove, at or shortly after, c. 7.0 ka;

(3) Mid-late Holocene glacier retreat to, or within, present-day limits after c. 7.0 ka;
(4) At least three late Holocene "neoglacial" readvances to the inner central area of Potter Peninsula between c. 1.7 and 1.4 ka and small readvances <1 cal. ka BP, similar in extent to the 1956 CE readvance;
(5) Recent deglaciation (post-1956 CE) and active glacial processes.

We examine the new evidence for these stages in detail in the following sections (Sections 5.1–Sections 5.5) in the context of regional environmental change across the SSI and northern AP during the Holocene and suggest possible mechanisms for deglaciation and glacier readvances (Section 5.6).

5.1 Early Holocene terrestrial deglaciation

Ice retreat on land after deglaciation from offshore LGM limits across the SSI occurred c. 11–8 cal. ka BP, constrained by ages obtained from glacially polished bedrock surfaces on the Barton and Weaver peninsulas, cosmogenic nuclide exposure ages, and the onset of lake sedimentation on Barton Peninsula, Fildes Peninsulas (KGI), and Byers Peninsula (Livingston Island) (Björck et al., 1996; Seong et al., 2008; Watcham et al., 2011; Toro et al., 2013; Oliva et al., 2016a, b; Nývlt et al., 2020).

Our tentative minimum ^{3}He cosmogenic nuclide exposure deglaciation age of 9.4 ± 2.6 ka from Three Brothers Hill on Potter Peninsula (Figure 4K) is broadly consistent with the high-altitude deglaciation history of KGI (Seong et al., 2008), and only one of the radiocarbon ages was obtained by Sugden and John (1973) (S&J Birm-48a in Table 2: 9,670 ± 230 ^{14}C years; 9,570 ± 650 cal. a BP), which is clearly an outlier (Figures 6B–D, 9B, D).

The interpretation of lithofacies assemblages in the nPII and PC stratigraphic sections underpins our revised deglaciation history for Potter Peninsula. Both sections have a lithofacies association typical of polythermal tidewater glaciers (Stewart et al., 1991; Bennett et al., 1999). Lithofacies 1, 3, and 4 were deposited in a distal glaciomarine environment isolated from wave action, with the occasional release of ice-rafted debris. Lithofacies 2 is a dense debris flow entering the glaciomarine environment. Escape structures made by *Laternula elliptica* cut across debris flow beds deposited between the glaciomarine sediments suggest that the high sedimentation rate caused by the proximity of a glacier likely forced the bivalves to the surface (Figure 6A) (del Valle et al., 2007; Strelin et al., 2014).

Our oldest sample from a depth of 3.30 m in the nPII and PC sections has a calibrated age of 7,910 ± 260 cal. a BP and a 2σ age range of 8,170–7,660 cal. a BP (Table 2, no. 15), in agreement with more recent studies (Strelin et al., 2014). Similar ages from a further 25 samples from Lithofacies 1–4 convincingly show that a glacier-free environment existed at a low altitude in the mouth of Potter Cove before 8.2 cal. ka BP (Figures 6A–C; Table 2). This new minimum deglaciation age is younger than, but consistent with, previous ages from these deposits (cf. Sugden and John, 1973) and our new minimum ^{3}He cosmogenic nuclide exposure age from Three Brothers Hill of 9.4 ± 2.6 ka.

Our paleoenvironmental interpretations for the nPII and PC sections are in broad agreement with previous studies. However, we could not replicate older chronologies even though the nPII is 2.5 m deeper than the nearby sections dated by Sugden and John (1973) and del Valle et al. (2007). Our Bayesian age-depth and probability density phase modeling (Figure 6B) reinforces that the older Sugden and John (1973) ages from Lithofacies units 1–5 represent the reworking of an older phase of glacier-free conditions in the outer peninsula or they are statistical outliers, possibly related to improvements in AMS radiocarbon dating since the 1970s.

Our revised early Holocene terrestrial deglaciation history for Potter Peninsula is consistent with evidence for enhanced glacier retreat from Maxwell Bay and sustained deglaciation on the nearby Barton and Fildes peninsulas at low altitude by c. 8.0 cal. ka BP (Figure 9B) (Seong et al., 2008; Milliken et al., 2009; Oliva et al., 2019), and glacier retreat on Livingston Island, c. 8.3–7.5 cal. ka BP (Oliva et al., 2016b). These events followed a period of sustained early Holocene warming across the northern AP region (Figures 9J,K) (Ingólfsson et al., 2003; Strelin et al., 2006; Bentley et al., 2009; Mulvaney et al., 2012).

5.2 A c. 7 ka glacier readvance

Radiocarbon ages from the marine shell-bearing horizons of Unit 5 in the nPII section provide a maximum age constraint of c. 7.0 cal. ka BP for a readvance of the former tidewater Fourcade Glacier to the outer mouth of Potter Cove. Glaciodeltaic facies on the surficial morainal bank terrace imply subaqueous discharge close to the calving zone, with contorted deformation structures near the top of Unit 5 most likely resulting from glaciotectonic push and shear (cf. Hambrey and McKelvey, 2000) indicative of subglacial deformation. Lithofacies 6 represents a period of intertidal sand accumulation, and the massive matrix-supported, clast-rich diamicton deposited on top of both sections is interpreted as a subglacial till formed by a readvance at or shortly after c. 7.0 cal. ka BP (Figures 6A, D, 9D).

Changes in RSL recorded in raised beaches and isolation basins of the SSI provide the most reliable evidence of deglaciation, ice loading, and readvance (e.g., Johnson et al., 2022). As isolation basins are less prone to reworking and remobilization than raised beaches, we attempted to corroborate evidence for a < c. 7 ka readvance in the nPII profile from isolation basins on Potter Peninsula (Figure 2C) below the 8 ka SSI Holocene marine limit at ~16 m a.s.l. (Fretwell et al., 2010; Watcham et al., 2011) (Figure 9C) by looking for sediment records with marine to terrestrial transitions, but most have unsuitable gravel (or boulder-strewn) lake beds.

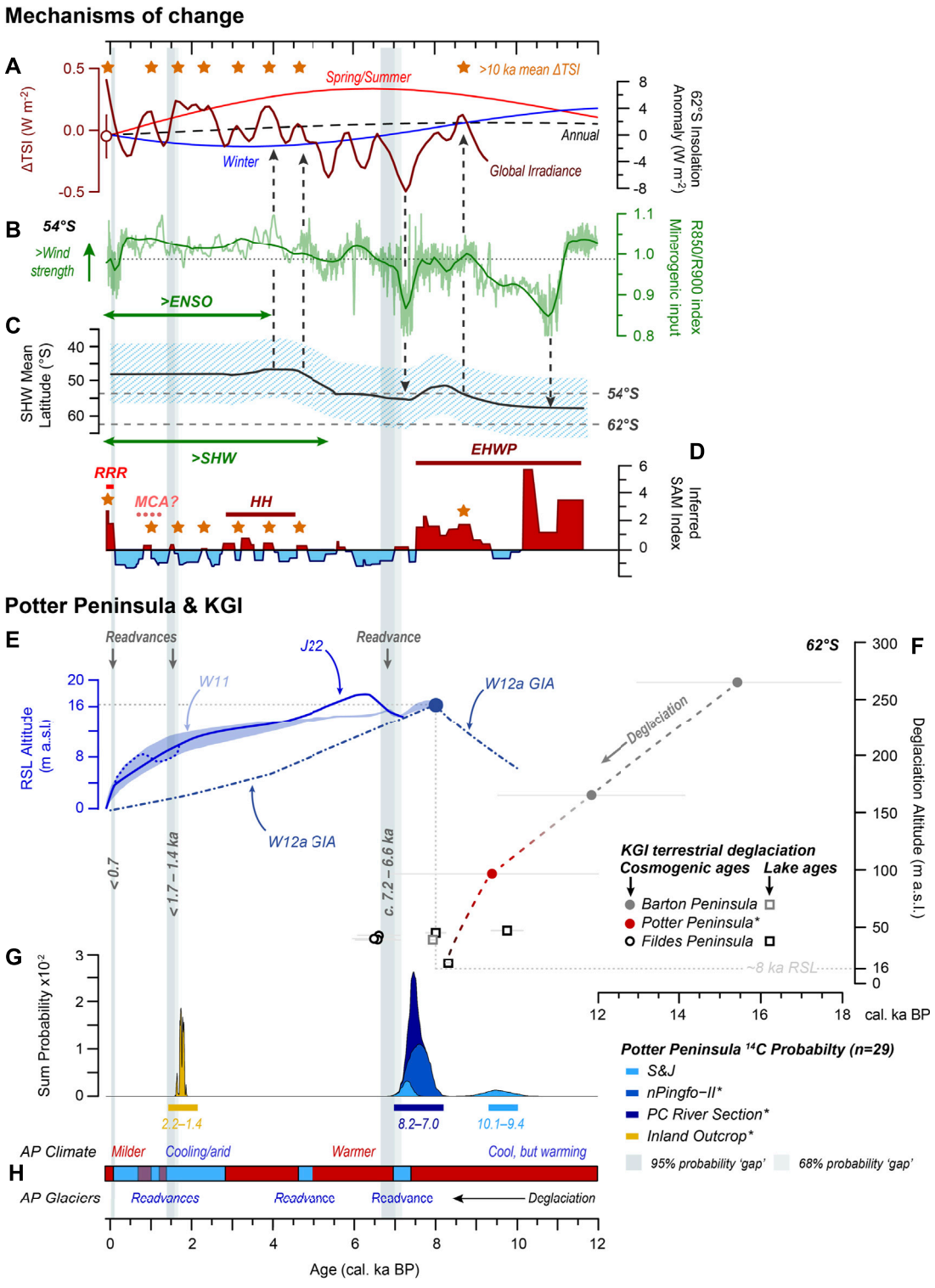

FIGURE 10
Mechanisms of deglaciation and glacier fluctuations on Potter Peninsula. **(A)** Total Solar Irradiance, as ΔTSI, which represents the deviation from present-day value (Steinhilber et al., 2009), compared with annual (dashed black line), austral spring/summer (SONDJF) (red line), and winter (JJA) (blue line) solar insolation received at 62°S during the Holocene (Laskar et al., 2004). The open red circle is the mean ± 1σ ΔTSI value for the last 10 ka; orange stars mark ΔTSI peaks greater than the 10 ka mean value. **(B)** Ultra-high resolution (69 μm) hyperspectral (SPECIM) R850/R900 data, a proxy for mineral input into the Emerald Lake, Macquarie Island at 54°S (Saunders et al., 2018), which reflects changes in the Southern Hemisphere Westerly wind (SHW) strength during the mid-late Holocene; the dark grey horizontal dotted line is the R850/R900 dataset mean; dark green line is
(*Continued*)

FIGURE 10 (Continued)
100-year interval LOESS regression of the R850/R900. **(C)** Hypothetical representation of changes in the mean annual latitudinal position of the core SHW intensity belt (dark grey line) and approximate 1σ latitudinal range of enhanced precipitation (light blue stipple) (Ariztegui et al., 2010; Quade and Kaplan, 2017). In reality, the SHW are more intense and focused during positive (warmer) phases of the SAM, but weaker, latitudinally broader, and less focused during negative (colder) phases of the SAM, shown in **(D)**. The light grey horizontal dashes are 54°S (Macquarie Island) and 62°S (South Shetland Islands); vertical dashed lines and arrows highlight the key hypothesized latitudinal shifts of the Holocene and their relationship to the global irradiance profile shown in A; ENSO, El Niño Southern Oscillation. **(D)** Inferred Holocene SAM-index variability between positive (red) to negative (blue) SAM-like states based on Northern Arboreal Pollen data from Southern Chile (Moreno et al., 2018; Reynhout et al., 2019) (sub-figure adapted from Kaplan et al. (2020); abbreviations are as defined in Figure 9K. **(E)** Summarized relative sea level (RSL) envelope for the SSI (W11, light blue shading; Watcham et al., 2011) compared with the RSL curve in Johnson et al. (2022) (J22, dark solid and dotted blue lines) and the W12a GIA model (Whitehouse et al., 2012a, b); see original references for further details and data. **(F)** Cosmogenic nuclide exposure ages and key lake basal age constraints on the deglaciation of KGI at different altitudes from Barton Peninsula (Seong et al., 2008), Potter Peninsula (this study), and Fildes Peninsula (secondary plot); *, new data (this study). **(G)** Summed probability profiles and phases (bars) derived from new radiocarbon age data from Potter Peninsula in this study compared with previously published radiocarbon data (S&J, Sugden and John, 1973). **(H)** Summary climate syntheses for the Antarctic Peninsula (based on Ingólfsson et al., 2003; Bentley et al., 2009; see Supplementary Figure S7 for an extended version).

RSL curves for the AP and SSI exhibit a regionally coherent shift from rising to falling RSL focused on c. 8.0–7.5 ka, reflecting ice retreat across the northern AP and SSI and isostatic uplift outpacing sea level rise (Roberts et al., 2011; Watcham et al., 2011; Johnson et al., 2022), which possibly prevented further marine-upwelling induced retreat of the Potter Cove glacier. The new c. 7 ka maximum age constraint on glacier readvance for Potter Cove/Peninsula from the nPII section is coeval with a phase of renewed, but comparatively minor, uplift at c. 7.2–7.0 cal. ka BP associated with a standstill or readvance (and/or thickening) of the BIC first determined from isolation basin studies on Fildes Peninsula (Watcham et al., 2011).

A c. 7 ka readvance is also in broad agreement with surface exposure ages of c. 7.0 cal. ka BP from moraine boulders, which represent a glacier advance on Hurd Peninsula, Livingston Island (Hall, 2007), and land-based glacier readvances on James Ross Island, northeast AP, between 7.3 and 7.1 cal. ka BP (Figure 9I) (Strelin et al., 2006; Kaplan et al., 2020). Terrestrial and marine proxies in records from the northern AP indicate extensive glacial melt and open waters without sea ice in Maxwell Bay, and generally warmer than Holocene average conditions, similar to the present-day shortly after c. 7 ka BP (Figures 9A, F, G) (Milliken et al., 2009; Watcham et al., 2011; Mulvaney et al., 2012; Peck et al., 2015; Roberts et al., 2017). Therefore, a precise climate connection between these records and glacier readvance at c. 7 ka on Potter Peninsula remains unclear and is discussed further in Section 5.6.

5.3 Mid-late Holocene deglaciation

Radiocarbon ages from basal lake sediments suggest that glaciers across the SSI and northern AP had receded to within or close to their present-day limits by c. 6 cal. ka BP (Mäusbacher et al., 1989; Watcham et al., 2011; Roberts et al., 2017; Giralt et al., 2020; Gomez et al., 2020). Marine sediment records from Maxwell Bay show decreasing sea surface temperatures (SST) and increasing sea ice cover between c. 5.9 and 2.6 cal. ka BP (Milliken et al., 2009), but we found no evidence for glacier readvance on Potter Peninsula in this period (Figures 6C, 9D).

Hall (2010) and Watcham et al. (2011) suggested that RSL fall was broadly continuous after 6 cal. ka BP (Figure 9C). Although del Valle et al. (2002) considered abandoned elevated coastal sediments at 17.1–14.4 m a.s.l. at Stranger Point with radiocarbon ages of 5.5–5.4 cal. ka BP to provide a minimum age for beach formation and the onset of the deglaciation on Potter Peninsula, it seems more likely that these deposits relate to continued uplift following early Holocene deglaciation and retreat after the c. 7 ka readvance. The latter interpretation is consistent with a maximum age of 4.3 cal. ka BP for glacier sediments that overlie the highest continuous raised beach at Stranger Point at ~12 m a.s.l. and RSL curves for the SSI (Fretwell et al., 2010; Watcham et al., 2011; Lindhorst and Schutter, 2014; Johnson et al., 2022).

Jeong (2006) proposed that the diameter of sorted vegetated polygons on KGI is directly related to formation age, with the largest polygon (3.23 m) dated at 5.4 ± 0.1 cal. ka BP. Polygons ~2.5 m in diameter were measured in this study and are tentatively assigned ages >2.6 ka using this method. Deglaciation ages derived using this method have obvious limitations but provide the only available age estimate for the periglacial landform assemblage (LA-4) on Potter Peninsula. Nevertheless, this age is consistent with ages of 4.5 to 2.8 cal. ka BP for a period of sustained mid-to-late Holocene warming, termed the Mid-Holocene Hypsithermal (MHH) in Bentley et al. (2009). Now referred to as the Holocene Hypsithermal (HH in Figures 9K, 10D), it has been identified in lake sediments from across the northern AP and (sub) Antarctic islands when glaciers were mostly situated close to, or landward of, their present-day limits (Björck et al., 1991a; Björck, 1991b; Ingólfsson et al., 2003; Sun et al., 2005; Bentley et al., 2009; Strother et al., 2015; Foster et al., 2016; Roberts et al., 2017).

5.4 Neoglaciation in the last 2,000 years

New geomorphological mapping and chronological evidence presented in this study show the Warszawa Icefield/Fourcade Glacier advanced beyond present-day limits on at least three occasions during the late Holocene: after c. 1.7–1.4 ka, following the return to "neoglacial" conditions (cf. Ingólfsson et al., 2003; Bentley et al., 2009), after c. 0.7 ka and at 1956 CE.

5.4.1 <1.7–1.4 ka readvances

The "Inland Outcrop," a massive matrix-supported sandy diamicton sequence, ~700 m from the present glacier front, was revealed in 2013 following at least ~60 years of retreat of the Warszawa Icefield across the inner Potter Peninsula (Figure 2A). This diamicton was probably derived from the foliation of entrained subglacial debris at the glacier front, forming unstable ridges of till with sedimentary characteristics of re-sedimentation from a primary subglacial till by melt-out. During melt seasons, its foliation likely collapsed, and any orientation has now been lost (cf. Hambrey et al., 2015).

Warmer and/or more humid conditions that existed before c. 2.2 cal. ka BP, implied by the presence of moss within the "Inland Outcrop" (Figures 6C, 9D), are consistent with similar conditions implied by the first of the two closely-spaced phases of freshwater subaquatic moss deposition in lake records from Fildes Peninsula at c. 2.2–1.9 cal. ka BP and 1.5–1.3 cal. ka BP (Roberts et al., 2017). Remnants of moss layers scattered randomly at its base have median calibrated ages of 1.8 and 1.7 cal. ka BP and a 95% summed probability range of 2.2–1.4 cal. ka BP (Table 2), meaning they were most likely emplaced when the Warszawa Icefield had readvanced further landward by c. 1.7–1.4 cal. ka BP (Figures 6C, 9D).

We link the "Inland Outcrop" to the ice-cored Stranger Point moraine system based on their relative positions to the present glacier margin and the degree of degradation and extent of mass-wasting processes (e.g., landslides and weathering) within the diamicton (Figures 2, 8A–D, F; Table 1). As these sequences are in front of a former theoretical limit of the Warszawa Icefield and form part of the inactive glacial landform assemblage (LA-2) (Figure 2; Table 1), we propose that both sequences were formed by the same glacier advance and subsequent melt-out processes that produced thrusting and deformation of subglacial till at the glacier margin of the Warszawa Icefield (Figures 2, 8C; Table 2).

A readvance sometime after 2.2 cal. ka BP and by c. 1.7–1.4 cal. ka BP in the central foreland of Potter Peninsula is consistent with ages of c. 1.9 cal. ka BP obtained from raised beaches up to 7.3 m a.s.l. overlying volcanic bedrock and till on the south side of Potter Peninsula that imply increased late Holocene ice loading (Lindhorst and Schutter, 2014). The timing is also consistent with offshore evidence of a glacier readvance dated to c. 2.6–1.6 cal. ka BP from the outermost marine moraine complex, M1, in Potter Cove (Figure 1C; Wölfl et al., 2016) and marine diamictons deposited by ice rafting in Maxwell Bay between c. 1.4 and 1.1 cal. ka BP (Ingólfsson et al., 2003; Yoon et al., 2004). The M1 moraine represents the furthest preserved maximum position of the Fourcade Glacier in the late Holocene (Wölfl et al., 2016).

Although late Holocene ice loading and readvances on Potter Peninsula are too small to be modeled by regional-scale ice sheet and glacio-isostatic adjustment models (e.g., Whitehouse et al., 2012a, b), the most recent RSL curve for the SSI (Johnson et al., 2022) (Figure 9C) hypothesizes that the continuous decline from the Holocene marine limit between 8 and 6 ka was interrupted by increased isostatic uplift between 1.5 and 0.5 ka BP. Rebound at this time relates to the "most significant" readvance event of the mid-late Holocene (Hall, 2010) and is consistent with published raised beach data and evidence for a post c. 2 ka "neoglacial" readvance on Potter Peninsula.

Colder "neoglacial" conditions persisted on the SSI and northern AP from c. 2 ka (2070 ± 50 cal a BP in Čejka et al. (2020)) onward (Ingólfsson et al., 2003; Bentley et al., 2009; Mulvaney et al., 2012; Roberts et al., 2017; Palacios et al., 2020; Čejka et al., 2020). However, readvance of the BIC on Fildes Peninsula remained restricted close to, or within, present-day limits (Hall, 2003; Hall, 2007; Hass et al., 2010), whereas on the Barton Peninsula (KGI) and the Byers Peninsula (Livingston Island), radiocarbon dating of basal lake sediments and exposure ages from bedrock outcrops show that no substantial glacier readvances have occurred in the last 2.4 cal. ka BP (Seong et al., 2008; Oliva et al., 2016a; Oliva et al., 2016b; Oliva et al., 2019). There is also some evidence for short-lived warmer phases in terrestrial records from the northern AP and the sub-Antarctic islands between c. 1.8 and 0.7 cal. ka BP (Bentley et al., 2007, 2009; Hall, 2007; Hall, 2010; Foster et al., 2016; Guglielmin et al., 2016; van der Bilt et al., 2017) and generally warmer SST on the western AP between c. 2 and 0.8 cal. ka BP (Shevenell et al., 2011; Etourneau et al., 2013).

5.4.2 <0.7 ka readvances

Our new geomorphological mapping revealed vegetated protalus ramparts between 30 and 60 m a.s.l. on Potter Peninsula, approximately 200 m below the current ELA, implying that cooler and drier environmental conditions existed when they were formed. By examining their cross-cutting relationships with raised beaches on Livingston Island, Serrano and López-Martı´nez (2000) and Kääb (2007) linked their formation to that of low altitude protalus landforms and rock glaciers which advanced between c. 0.8 and 0.3 ka. Applying a similar principle, the Stranger Point moraine system crosscuts raised beaches at 6 m a.s.l., implying a maximum age of 0.7 cal. ka BP for a readvance at this location (Heredia Barión et al., 2019). This age estimate is consistent with coastal gravel deposits at 6 m a.s.l. that were deposited on top of a till deposit at the west and north coast of Potter Peninsula sometime after 0.65 cal. ka BP (Sugden and John, 1973; Curl, 1980; Clapperton and Sugden, 1988; Lindhorst and Schutter, 2014; Heredia Barión et al., 2019).

Supporting evidence for a readvance after c. 0.7 ka and subsequent retreat also exists in the lake sediment records on Potter Peninsula. 1) The first evidence is the modeled age for the contact between the basal diamicton unit and the uppermost laminated sediments in the Matias Lake record of c. 0.3 cal. ka BP (Supplementary Figure S5). Del Valle et al. (2004) considered similar laminated sediments in adjacent Rudy Lake to be annual couplets (varves) with sedimentation rates of 1.2–1.7 mm yr^{-1}. This rate is similar to that obtained by ^{210}Pb and ^{137}Cs dating of the uppermost unit of laminated sediments in Matias Lake. The presence of basal gravels with large clasts grading into the uppermost unit of fine "varves" in our new cores from Matias Lake implies the lake was seasonally free of lake ice but with the glacier front nearby. Lead-210 dating of the uppermost laminated sediments of Matias Lake shows that glaciers had retreated from the Matias-Rudy Lake area by the mid-1850s. 2) The second is a minimum age of 0.5 ka from Rudy Lake, based on its relationships with adjacent moraines and varve counting of lake sediments above a diamicton deposit (Birkenmajer, 1998; del Valle et al., 2004). 3) The third is the shift to higher productivity and reduced erosion of sediment between zones 2 and 3 in Lake L15, evident in the higher TChl content and lower magnetic susceptibility (MS), Ti and Ca values in zone 3. This is indicative of ice retreat from the outer Potter Peninsula and the establishment of persistent seasonally lake-ice-free conditions sometime after 0.6 cal. ka BP (Figure 7A).

Data from marine sediment cores and the submerged moraine complexes M2 and M3 in Potter Cove show that the Fourcade Glacier was located forward of its present position in the inner cove between 0.5 and 0.1 cal. ka BP (Figure 1C) (Hass et al., 2010; Majewski et al., 2012; Wölfl et al., 2016; Munoz and Wellner, 2018). On Fildes Peninsula, ice-cored moraines composed of till, ice-proximal meltwater fan deposits and ice-marginal pond sediments were forming adjacent to present-day glacial margins by thrusting processes, incorporating remnants of mosses dated to c. 0.83–0.65 cal. ka BP (Hall, 2007). These mosses represent warmer/milder conditions before a <0.7 ka readvance, and their ages are coeval with the timing of the Mediaeval Climate Anomaly (MCA; Figure 9K) c. 1–0.7 cal ka BP, 950–1250 CE (Mann et al., 2009; Kaufman et al., 2020).

More widely, using radiocarbon and optically stimulated luminescence dating of raised beaches, Simms et al. (2012; 2021) showed that the last glacier readvances occurred across the SSI and the AP between c. 0.45 and 0.25 ka BP and that increased ice loading is consistent with increasing rates of post-MCA RSL decline on KGI in the last 500 years (Bentley et al., 2005; Hall, 2010; Watcham et al., 2011; Johnson et al., 2022) (Figures 9C, K). After this readvance, a short-term and rapid acceleration in rebound occurred between 1700 and 1840 CE (0.2–0.1 cal. ka BP), with a modeled peak uplift rate of 12.5 mm a-1 (Simms et al., 2012). Simms et al. (2012) also showed that RSL curves for the SSI showed accelerated fall rates in the last 500 years, indicative of prior increased ice loading, whereas those from western and north-eastern AP exhibit a gradually decreasing uplift rate, implying continuous deglaciation, despite extensive geomorphological evidence of mid-late Holocene glacier readvance (Bentley et al., 2005; Hall, 2010; Roberts et al., 2011; Watcham et al., 2011; Hodgson et al., 2013; Kaplan et al., 2020).

Evidence for a <0.7 ka readvance on Potter Peninsula is also broadly coeval with: 1) more persistently colder conditions on or around the SSI and the AP (Figure 9E) (Yoon et al., 2004; Liu et al., 2005; Hall, 2007; Hass et al., 2010; Monien et al., 2011; Angiel and Dąbski, 2012; Majewski et al., 2012; Hu et al., 2013; Roberts et al., 2017; Simms et al., 2021); 2) generally increased sea ice in Maxwell Bay and colder conditions in Bransfield Basin between c. 1.4 and 0.1 cal. ka BP (Heroy et al., 2008; Milliken et al., 2009; Mulvaney et al., 2012; Abram et al., 2013); 3) consistently colder reconstructed SST in proxy records from the western AP between c. 0.5 and 0.2 cal. ka BP (Figure 9H) (Shevenell et al., 2011; Etourneau et al., 2013); 4) evidence of a post "MCA" readvance elsewhere on the AP and some sub-Antarctic Islands (Bentley et al., 2007; Hall, 2007; Bentley et al., 2009; Hall, 2010; Roberts et al., 2010; Davies et al., 2014; Guglielmin et al., 2016; van der Bilt et al., 2017; Verfaillie et al., 2021), at a broadly similar time to the Northern Hemisphere "Little Ice Age" (0.55–0.25 cal. ka BP, 1400–1700 CE) (Mann et al., 2009; Kaufman et al., 2020).

5.5 Recent (post-1956 CE) deglaciation and active geomorphological processes

Aerial photographs show that the Warszawa Icefield was also in an advanced position close to the "Inland Outcrop" in 1956 CE (Figure 3). In 1956 CE, the front of the Fourcade (tidewater) glacier was located 1,200 m away from the mouth of Potter Cove (Figures 1, 2) and has since experienced a net retreat of more than 1,000 m along the flow line. Aerial and satellite imageries show that the Warszawa Icefield and the Fourcade Glacier then retreated rapidly to their present-day position between 1956 and 2013 CE (Figure 3B), and since 2016 CE, satellite imagery has shown that it has terminated on land (Jerosch et al., 2018).

After deglaciation, periglacial/frost action and mass movement became widespread on Potter Peninsula (Figures 3D, 4J). Rapid mass movements and rockfalls have transferred the sedimentary products of the periglacial processes down-slope, creating talus accumulation at the foot of bedrock plateaus and around Three Brothers Hill (Figure 2; Table 1). Cryoturbated sorted circles and polygons form on gentle slopes above 50 m a.s.l. and where surficial sediments are saturated with water due to the presence of a permafrost table that inhibits drainage. Repeated freeze-thaw processes, rather than permafrost (Matsuoka, 2001), most likely led to the formation of cryoturbated stone stripes on steeper slopes and gelifluction lobes at the base of the bedrock plateaus.

The inactive Stranger Point moraine system has been actively degraded by mudflows, solifluction, and thermokarst processes (Figures 2, 4G, 8A,C) (cf. López-Martínez et al., 2012; Oliva and Ruiz-Fernández, 2017). Meanwhile, thermokarst processes are prevalent in active ice-cored moraines close to the glacier margin at Stranger Point and across Potter Peninsula (Figures 4F, 8A, C) (John and Sugden, 1971; Sugden and John, 1973; Hochschild, 1995; Lukas, 2011). The large, suspended sediment load produced by intense glaciofluvial processes at the glacier front and the incision of relict moraines (Figures 4A, H) forms active glaciofluvial fans and deltas that prograde toward and into Potter Cove (Figure 2). Meltwater and suspended sediment change the physical and chemical properties of Potter Cove (Henkel et al., 2013; Monien et al., 2017; Henkel et al., 2018), impacting the local biological communities and, ultimately, the biogeochemical cycle of the Southern Ocean (Quartino et al., 2013; Pasotti et al., 2015a, b; Sahade et al., 2015; Monien et al., 2017; Falk et al., 2018; Henkel et al., 2018).

The uppermost 6.5 cm of Lake L15 and its surrounding environment at the base of Three Brothers Hill is dominated by freshwater subaquatic, littoral, and terrestrial mosses and cyanobacterial mats with post-1950 CE ages (Supplementary Figure S2; see Supplementary Material for further details). Elsewhere on KGI, increased primary productivity and moss colonization of the lake-water interface is commonplace in seasonally lake-ice-free and stable lacustrine environments undisturbed by glaciofluvial inputs and indicative of warmer and more favorable climatic conditions (Björck et al., 1991c; Roberts et al., 2017).

5.6 Mechanisms of change

After ice retreat from offshore LGM limits (Termination I), early Holocene deglaciation and subsequent glacier fluctuations on Potter Peninsula primarily reflect interactions between changes in climate and RSL (Bentley et al., 2009). It seems likely that a c. 7 ka glacier readvance was driven by a combination of changes in glacier stability associated with increased precipitation, regional glacio-isostatic adjustment, and/or local relative sea-level variations (Figures 10E–G) rather than major thickening of the glacier front, fjord geometry, and fjord depth (Mercer, 1961; Van der Veen, 1995).

Subsequent changes in Holocene glacier mass balance across the SSI were controlled by hemispheric to global scale climate processes and long-term (millennial-scale) trends in solar insolation at 62°S (i.e., increasing to c. 5 ka maximum, declining after c. 5 ka) (Bentley et al., 2009). Centennial–millennial-scale fluctuations in solar irradiance and interannual to decadal-scale changes in the SHW and SAM modulate long-term trends in insolation, driving centennial–millennial changes in temperature, precipitation, wind, sea ice formation, and glacier advance and retreat on the northern AP, the SSI, and southern South America (Figures 9, 10) (Bentley et al., 2009; Lamy et al., 2010; Varma et al., 2012; Charman et al., 2018; Moreno et al., 2018; Baggenstos et al., 2019; Reynhout et al., 2019; Kaplan et al., 2020; Verfaillie et al., 2021). The interannual relationship between insolation, temperature ENSO, and the SAM is also thought to operate across decadal-to-millennial timescales during the Holocene (Perren et al., 2020) (Figures 10B–D), impacting the AP (e.g., Dickens et al., 2019).

Deglaciation of the SSI before c. 8.2 ka coincided with a sustained phase of positive SAM-like conditions, increased global irradiance, increasing spring/summer insolation at 62°S, warmth and sustained glacier retreat, and more open water on and around the northern AP (Figures 9F–K, 10A and references therein). A c. 7 ka readvance on Potter Peninsula was initiated during a short-lived period of lower than Holocene average global solar irradiance (Figure 10A) that would have lowered the ELA across the SSI and negative (colder/more humid) SAM-like conditions (Figure 10D), likely leading to increases in year-round precipitation as snowfall (Kaplan et al., 2020).

In contrast, after c. 5 ka, a steadily declining trend in insolation at 62°S coupled with more persistently colder/wetter and more negative SAM-like conditions, stronger SHW, and an enhanced ENSO (especially during the last 4 ka) likely drove late Holocene readvances after c. 1.7–1.4 cal. ka BP, <0.7 cal. ka BP and by 1956 CE (Figures 10A, D, G) (Charman et al., 2018; Saunders et al., 2018; Yang et al., 2019; Perren et al., 2020).

More recently, the longer-term pattern of interannual variability in the SAM has been altered by the ozone hole over Antarctica, which, combined with increases in greenhouse gases and global temperature, is forcing a more positive trend in the SAM and further enhancing the ENSO (Marshall, 2007). The regionally synchronous retreat of most land-terminating glaciers across the northern AP and SSI since the mid-20th Century provides strong evidence that glacier retreat on KGI was initiated by increasing air temperatures (Braun and Gossmann, 2002; Bentley et al., 2009; Kaplan et al., 2020). Recent (post-1956 CE) deglaciation has exposed new onshore areas on Potter Peninsula to intense sediment reworking and redistribution, producing characteristic paraglacial, proglacial, and periglacial landforms on the glacier foreland of Potter Peninsula.

6 Conclusion

Using a glacial landsystems approach, we have produced a new geomorphological map for Potter Peninsula. Based on this and a detailed chronostratigraphic analysis of two new stratigraphic profiles and two new lake records on the glacier foreland, we propose the following five-stage deglaciation and readvance model for Potter Peninsula:

(1) Sustained low altitude deglaciation began before 8.2 cal. ka BP.
(2) Deglaciation was interrupted by a readvance that reached outer Potter Cove around, or shortly after, c. 7.0 cal. ka BP.
(3) Glacier retreat to or within present-day limits likely occurred between 6 and 2 ka. We found no new terrestrial evidence for readvances across Potter Peninsula in this interval.
(4) Evidence of up to three readvances on Potter Peninsula in the last 2000 years includes the following: i) radiocarbon ages from mosses embedded in glacial deposits of a recently exposed "Inland Outcrop" close to the modern glacier front implying a readvance had most likely occurred by c. 1.7–1.4 cal. ka BP; ii) geomorphic and lake stratigraphic (varve, ^{210}Pb dating) evidence for a <0.7 cal. ka BP readvance, most likely between 0.5 and 0.1 cal. ka BP; iii) aerial images showing the Warszawa Icefield ~700 m in front of its present-day limit by 1956 CE.
(5) Recent warming and deglaciation have exposed the glacier foreland to periglacial, paraglacial, mass wasting, and glaciofluvial processes.

- The timing of Holocene deglaciation and readvances on Potter Peninsula is broadly coeval with sites elsewhere on KGI, the SSI, and the northern AP.
- Early Holocene deglaciation occurred during phases of increased solar irradiance and increasing spring/summer insolation and during a sustained phase of more positive SAM-like conditions that have been associated with increased warmth and glacier retreat across the northern AP.
- Mid-late Holocene glacier readvances occurred during phases of reduced solar irradiance and when more negative (colder) SAM-like conditions existed.
- Field evidence for increased local late Holocene ice loading and readvances on Potter Peninsula is not well-represented in the regional-scale ice sheet and glacio-isostatic adjustment models.

Data availability statement

The datasets presented in this study can be found in the following NERC Polar Data Centre online repositories: *Chronological and sedimentological data:* https://doi.org/10.5285/4671A42F-7A2E-4883-948C-EF6B26DD41C9; *Lake L5 data:* https://doi.org/10.5285/6575CD7A-CFBA-4820-9FA6-257161B4D24B; *Lake L15 data:* https://doi.org/10.5285/2031310D-1E35-4EA1-A1CC-CD318E82D394; *Glacier advance/retreat data:* https://doi.org/10.5285/9337F8F4-1A8F-4156-8F79-7A249F733117. The names of the repository/repositories and accession number(s) can also be found in the Supplementary Material. The satellite images used in this paper and its Supplementary Material are Maxar products © 2022 Maxar technologies and have been reproduced at low resolution under license to BAS.

Author contributions

PB, JS, SR, and GK conceived the research questions, obtained funding, wrote the manuscript, and constructed figures and tables; PB, JS, SR, MB, EP, and NC undertook fieldwork and collected samples; PB made the geomorphological map and analyzed the landscape assemblages; PB, CS, LW, SN, SR MB, NC, and BS undertook cosmogenic and chronological sampling and analysis; SR, SD, MG, SA, and BP undertook lake sediment analysis. All authors undertook the data analysis and edited the final manuscript.

Funding

This study was funded by Centro de Investigaciones en Ciencias de la Tierra (CICTERRA), the Dirección Nacional del Antártico/Instituto Antártico Argentino (DNA/IAA), in the framework of the Project PICTA, 2011 – 0102, IAA "Geomorfología y Geología Glaciar del Archipiélago James Ross e Islas Shetland del Sur, Sector Norte de la Península Antártica," and the Alfred Wegener Institute (AWI) research program Polar Regions and Coasts in a Changing Earth System (PACES II). PHB, GK, JS, SR, EP, and TMC were funded IMCONet (FP7 IRSES, action no. 318718) led by Doris Abele (AWI). EP and SR received additional funding from the Natural Environment Research Council (NERC/BAS-CGS Grant no.81). SR and MB were funded by the NERC/BAS science programmes CACHE-PEP: Natural climate variability—extending the Americas palaeoclimate transect through the Antarctic Peninsula to the pole and GRADES-QWAD: Quaternary West Antarctic Deglaciations.

Acknowledgments

The authors thank the crews of the Argentine research station "Carlini" and the adjoined German Dallmann (AWI) Laboratory, the Uruguayan research station "Artigas," the Russian Bellingshausen Station, the Chinese Great Wall Station, Base Presidente Eduardo Frei Montalva, the Brazilian Navy Almirante Maximiano, the UK Navy (HMS Endurance), and NERC/BAS James Clark Ross for their cordial hospitality and invaluable logistical support during the 2006, 2011, 2014, and 2015 field seasons. Fieldwork assistance by M. Barrionuevo, M. Makeschin, M. Argota, D. Mengedoht, I. Schutter, and B. Maltman was greatly appreciated, as were field pictures provided by M. Martini. They also thank S. Wiebe and R. Fröhlking for their support with textural analyses; C. Schott, A. Toltz, M. Medina, and E. Schnabel for sample processing, mineralogy determination, and noble gas analysis for ^{3}He exposure dating; and Mari Whitelaw from the UKRI Polar Data Centre. They thank Tim

Heaton (Marine20 radiocarbon calibration) and Bethan Davies (geomorphology/landsystems) for discussions and suggestions, and Daniel Nývlt and Yuribia Munoz for constructive review comments which helped improve the original manuscript. This article is dedicated to the memory of Doris Abele and Christian Haas, inspirational scientists and good friends who made the IMCONet Exchange Program possible and very enjoyable.

Conflict of interest

The authors declare that the research was conducted in the absence of any commercial or financial relationships that could be construed as a potential conflict of interest.

Publisher's note

Supplementary material

The Supplementary Material for this article can be found online at: https://www.frontiersin.org/articles/10.3389/feart.2022.1073075/full#supplementary-material

References

Abram, N. J., Wolff, E. W., and Curran, M. A. J. (2013). A review of sea ice proxy information from polar ice cores. *Quat. Sci. Rev.* 79, 168–183. doi:10.1016/j.quascirev.2013.01.011

Angiel, P. J., and Dąbski, M. (2012). Lichenometric ages of the little ice age moraines on king George island and of the last volcanic activity on penguin island (west Antarctica). *Geogr. Ann. Ser. A, Phys. Geogr.* 94, 395–412. doi:10.1111/j.1468-0459.2012.00460.x

Appleby, P. G., and Oldfield, F. (1978). The calculation of lead-210 dates assuming a constant rate of supply of unsupported 210Pb to the sediment. *CATENA* 5, 1–8. doi:10.1016/s0341-8162(78)80002-2

Ariztegui, D., Gilli, A., Anselmetti, F. S., Goñi, R. A., Belardi, J. B., and Espinosa, S. (2010). Lake-level changes in central Patagonia (Argentina): Crossing environmental thresholds for lateglacial and Holocene human occupation. *J. Quat. Sci.* 25, 1092–1099. doi:10.1002/jqs.1352

Baggenstos, D., Häberli, M., Schmitt, J., Shackleton, S. A., Birner, B., Severinghaus, J. P., et al. (2019). Earth's radiative imbalance from the Last Glacial Maximum to the present. *Proc. Natl. Acad. Sci. U. S. A.* 116, 14881–14886. doi:10.1073/pnas.1905447116

Balco, G., Stone, J. O., Lifton, N. A., and Dunai, T. J. (2008). A complete and easily accessible means of calculating surface exposure ages or erosion rates from 10Be and 26Al measurements. *Quat. Geochronol.* 3, 174–195. doi:10.1016/j.quageo.2007.12.001

Ballantyne, C. K. (2002). Paraglacial geomorphology. *Quat. Sci. Rev.* 21, 1935–2017. doi:10.1016/s0277-3791(02)00005-7

Benn, D. I., and Evans, D. J. A. (2010). *Glaciers and glaciation*. London, England, United Kingdom: Hodder Education.

Bennett, M. R., Hambrey, M. J., Huddart, D., Glasser, N. F., and Crawford, K. (1999). The landform and sediment assemblage produced by a tidewater glacier surge in Kongsfjorden, Svalbard. *Quat. Sci. Rev.* 18, 1213–1246. doi:10.1016/s0277-3791(98)90041-5

Bentley, M. J., Evans, D. J. A., Fogwill, C. J., Hansom, J., Sugden, D., and Kubik, P. (2007). Glacial geomorphology and chronology of deglaciation, South Georgia, sub-Antarctic. *Quat. Sci. Rev.* 26, 644–677. doi:10.1016/j.quascirev.2006.11.019

Bentley, M. J., Hodgson, D. A., Smith, J. A., Cofaigh, C., Domack, E., Larter, R., et al. (2009). Mechanisms of Holocene palaeoenvironmental change in the antarctic peninsula region. *Holocene* 19, 51–69. doi:10.1177/0959683608096603

Bentley, M. J., Hodgson, D. A., Smith, J. A., and Cox, N. (2005). Relative sea level curves for the South Shetland islands and marguerite Bay, antarctic peninsula. *Quat. Sci. Rev.* 24, 1203–1216. doi:10.1016/j.quascirev.2004.10.004

Bentley, M. J., Ó Cofaigh, C., Anderson, J. B., Conway, H., Davies, B., Graham, A. G., et al. (2014). A community-based geological reconstruction of antarctic ice sheet deglaciation since the last glacial maximum. *Quat. Sci. Rev.* 100, 1–9. doi:10.1016/j.quascirev.2014.06.025

Bevan, A. (2021). rcarbon: Calibration and analysis of radiocarbon dates. https://github.com/ahb108/rcarbon/.

Birkenmajer, K. (1998). Quaternary geology at potter peninsula, king George island (South Shetland islands, west Antarctica). *Bull. Pol. Acad. Sci. Earth Sci.* 46, 9–20.

Björck, S., Håkansson, H., Zale, R., Karlen, W., and Jonsson, B. L. (1991a). A late Holocene lake sediment sequence from Livingston Island, South Shetland Islands, with palaeoclimatic implications. *Antartic. Sci.* 3, 61–72. doi:10.1017/s095410209100010x

Björck, S., Hjort, C., Ingolfsson, O., and Skog, G. (1991c). "Radiocarbon dates from the Antarctic peninsula region — Problems and potential,". Radiocarbon dating: recent applications and future potential. Editor J. J. Lowe, 55–65.*Quat. Proc.*, 24.

Björck, S., Hjort, C., Ingólfsson, Ó., Zale, R., and Ising, J. (1996). "Holocene deglaciation chronology from lake sediments," in *Geomorphological map of Byers peninsula, Livingston island. BAS GEOMAP series, sheet 5-A*. Editor J. López-Martínez, et al. (Cambridge: British Antarctic Survey), 49–51.

Björck, S., Malmer, N., Hjort, C., Sandgren, P., Ingólfsson, Ó., Wallén, B., et al. (1991b). Per sandgren, ólafur Ingólfsson, bo wallén, ronald ian lewis smith, and bodil liedberg JónssonStratigraphic and paleoclimatic studies of a 5500-year-old moss bank on elephant island, Antarctica. *Arct. Alp. Res.* 23, 361–374. doi:10.2307/1551679

Blaauw, M., and Christen, J. A. (2011). Flexible paleoclimate age-depth models using an autoregressive gamma process. *Bayesian Anal.* 6, 457–474. doi:10.1214/11-ba618

Blindow, N., Suckro, S. K., Rückamp, M., Braun, M., Schindler, M., Breuer, B., et al. (2010). Geometry and thermal regime of the King George Island ice cap, Antarctica, from GPR and GPS. *Ann. Glaciol.* 51, 103–109. doi:10.3189/172756410791392691

Bockheim, J., Vieira, G., Ramos, M., Lopez-Martinez, J., Serrano, E., Guglielmin, M., et al. (2013). Climate warming and permafrost dynamics in the Antarctic Peninsula region. *Glob. Planet. Change* 100, 215–223. doi:10.1016/j.gloplacha.2012.10.018

Borchers, B., Marrero, S., Balco, G., Caffee, M., Goehring, B., Lifton, N., et al. (2016). Geological calibration of spallation production rates in the CRONUS-Earth project. *Quat. Geochronol.* 31, 188–198. doi:10.1016/j.quageo.2015.01.009

Braun, M., and Gossmann, H. (2002). "Glacial changes in the areas of admiralty Bay and potter cove, king George island, maritime Antarctica," in *Geoecology of antarctic ice-free coastal landscapes*. Editors L. Beyer and M. Bölter (Berlin, Heidelberg: Springer Berlin Heidelberg), 75–89.

Bronk Ramsey, C. (2009). Bayesian analysis of radiocarbon dates. *Radiocarbon* 51, 337–360. doi:10.1017/s0033822200033865

Butz, C., Grosjean, M., Fischer, D., Wunderle, S., Tylmann, W., and Rein, B. (2015). Hyperspectral imaging spectroscopy: A promising method for the biogeochemical analysis of lake sediments. *J. Appl. Remote Sens.* 9, 096031. doi:10.1117/1.jrs.9.096031

Butz, C., Grosjean, M., Goslar, T., and Tylmann, W. (2017). Hyperspectral imaging of sedimentary bacterial pigments: A 1700-year history of meromixis from varved lake jaczno, northeast Poland. *J. Paleolimnol.* 58, 57–72. doi:10.1007/s10933-017-9955-1

Čejka, T., Nývlt, D., Kopalová, K., Bulínová, M., Kavan, J., Lirio, J. M., et al. (2020). Timing of the neoglacial onset on the north-eastern antarctic peninsula based on

lacustrine archive from lake anónima, vega island. *Glob. Planet. Change* 184, 103050. doi:10.1016/j.gloplacha.2019.103050

Charman, D. J., Roland, T. P., Amesbury, M. J., Royles, J., Hodgson, D. A., Convey, P., et al. (2018). Spatially coherent late Holocene Antarctic Peninsula surface air temperature variability. *Geology* 46, 1071–1074. doi:10.1130/g45347.1

Clapperton, C. M., and Sugden, D. E. (1988). Holocene glacier fluctuations in South America and Antarctica. *Quat. Sci. Rev.* 7, 185–198. doi:10.1016/0277-3791(88)90005-4

Curl, J. E. (1980). *A glacial history of the South Shetland islands, Antarctica*. Columbus, OH 43210, USA: Institute of Polar Studies The Ohio State University, 129.

Davies, B. J., Glasser, N. F., Carrivick, J. L., Hambrey, M. J., Smellie, J. L., and Nyvlt, D. (2013). Landscape evolution and ice-sheet behaviour in a semi-arid polar environment: James Ross Island, NE Antarctic Peninsula. *Geol. Soc. Lond. Spec. Publ.* 381, 353–395. doi:10.1144/sp381.1

Davies, B. J., Golledge, N. R., Glasser, N. F., Carrivick, J. L., Ligtenberg, S. R. M., Barrand, N. E., et al. (2014). Modelled glacier response to centennial temperature and precipitation trends on the Antarctic Peninsula. *Nat. Clim. Change* 4, 993–998. doi:10.1038/nclimate2369

Davies, S. J., Lamb, H. F., and Roberts, S. J. (2015). "Micro-XRF core scanning in palaeolimnology: Recent developments," in *Micro-XRF studies of sediment cores: Applications of a non-destructive tool for the environmental sciences*. Editors I. W. Croudace and R. G. Rothwell (Dordrecht: Springer Netherlands), 189–226.

de Pablo, M. A., Blanco, J. J., Molina, A., Ramos, M., Quesada, A., and Vieira, G. (2013). Interannual active layer variability at the limnopolar Lake CALM site on Byers peninsula, Livingston island, Antarctica. *Antarct. Sci.* 25, 167–180. doi:10.1017/s0954102012000818

del Valle, R. A., Montalti, D., Inbar, M., and Boaretto, E. (2007). Holoceno marino en la península Potter, Isla 25 de Mayo, Antártida. *Rev. Asoc. Geol. Argent.* 62, 35–43.

del Valle, R. A., Montalti, D., and Inbar, M. (2002). Mid-holocene macrofossil-bearing raised marine beaches at potter peninsula, king George island, South Shetland islands. *Antarct. Sci.* 14, 263–269. doi:10.1017/S0954102002000081

del Valle, R. A., Tatur, A., Lusky, J., and Gómez Izquierdo, D. (2004). Cambios morfológicos recientes en lagos de la península Potter, isla 25 de Mayo, islas Shetland del Sur. *Antártida. Rev. Asoc. Geol. Argent.* 59, 443–450. (

Deregibus, D., Scharf, F. K., Pasotti, F., Ruiz Barlett, E., Servetto, N., and Abele, D. (2015). IMCONet research areas map of potter cove, king-george island (I. 25 de Mayo), with links to maps. *Inst. Antártico Argent. Buenos Aires, Argent.* doi:10.1594/PANGAEA.853859

Dickens, W. A., Kuhn, G., Leng, M. J., Graham, A. G. C., Dowdeswell, J. A., Meredith, M. P., et al. (2019). Enhanced glacial discharge from the eastern antarctic peninsula since the 1700s associated with a positive southern annular mode. *Sci. Rep.* 9, 14606. doi:10.1038/s41598-019-50897-4

Dunlea, A. G., Murray, R. W., Tada, R., Alvarez-Zarikian, C. A., Anderson, C. H., Gilli, A., et al. (2020). Intercomparison of XRF core scanning results from seven labs and approaches to practical calibration. *Geochem. Geophys. Geosyst.* 21, e2020GC009248. doi:10.1029/2020gc009248

Etourneau, J., Collins, L. G., Willmott, V., Kim, J. H., Barbara, L., Leventer, A., et al. (2013). Holocene climate variations in the Western antarctic peninsula: Evidence for sea ice extent predominantly controlled by changes in insolation and ENSO variability. *Clim. Past.* 9, 1431–1446. doi:10.5194/cp-9-1431-2013

Evans, D. J. A., and Hiemstra, J. F. (2005). Till deposition by glacier submarginal, incremental thickening. *Earth Surf. Process. Landforms* 30, 1633–1662. doi:10.1002/esp.1224

Falk, U., López, D. A., and Silva-Busso, A. (2018). Multi-year analysis of distributed glacier mass balance modelling and equilibrium line altitude on King George Island, Antarctic Peninsula. *Cryosphere* 12, 1211–1232. doi:10.5194/tc-12-1211-2018

Falk, U., and Silva-Busso, A. (2020). Discharge of groundwater flow to the potter cove on king George island, antarctic peninsula. *Hydrol. Earth Syst. Sci. Discuss.* 2020, 1–24.

Foster, L. C., Pearson, E. J., Juggins, S., Hodgson, D. A., Saunders, K. M., Verleyen, E., et al. (2016). Development of a regional glycerol dialkyl glycerol tetraether (GDGT)–temperature calibration for Antarctic and sub-Antarctic lakes. *Earth Planet. Sci. Lett.* 433, 370–379. doi:10.1016/j.epsl.2015.11.018

Fourcade, N. H. (1960). Estudio geológico-petrográfico de Caleta Potter, Isla 25 de Mayo, Islas Shetland del Sur. *Inst. Antártico Argent. Publicación, (8)Instituto Antártico Argent. Publicación* 8, 119.

Fretwell, P. T., Hodgson, D. A., Watcham, E. P., Bentley, M., and Roberts, S. (2010). Holocene isostatic uplift of the South Shetland islands, antarctic peninsula, modelled from raised beaches. *Quat. Sci. Rev.* 29, 1880–1893. doi:10.1016/j.quascirev.2010.04.006

Gibbard, P. L., and Head, M. J. (2020). "Chapter 30 - the quaternary period,". Editors F. M. Gradstein, J. G. Ogg, M. D. Schmitz, and G. M. Ogg (Elsevier), 1, 1217–1255.*Geol. Time Scale 2020*

Giralt, S., Hernández, A., Pla-Rabes, S., Antoniades, D., Toro, M., and Granados, I. (2020). "Chapter 3 - Holocene environmental changes inferred from Antarctic lake sediments," in *Past Antarctica*. Editors M. Oliva and J. Ruiz-Fernández (Academic Press), 51–66. doi:10.1016/B978-0-12-817925-3.00003-3

Glasser, N. F., and Bennett, M. R. (2004). Glacial erosional landforms: Origins and significance for palaeoglaciology. *Prog. Phys. Geogr. Earth Environ.* 28, 43–75. doi:10.1191/0309133304pp401ra

Gomez, N., Weber, M. E., Clark, P. U., Mitrovica, J. X., and Han, H. K. (2020). Antarctic ice dynamics amplified by Northern Hemisphere sea-level forcing. *Nature* 587, 600–604. doi:10.1038/s41586-020-2916-2

González-Ferrán, O., and Katsui, Y. (1970). *Estud. integral del volcanismo cenozoico Super. las Islas Shetl. del Antártida* 1, 123–174. Santiago de Chile.

Goodwin, B. P., Mosley-Thompson, E., Wilson, A. B., Porter, S. E., and Sierra-Hernandez, M. R. (2016). Accumulation variability in the antarctic peninsula: The role of large-scale atmospheric oscillations and their interactions. *J. Clim.* 29, 2579–2596. doi:10.1175/jcli-d-15-0354.1

Gordon, J. E., and Harkness, D. D. (1992). Magnitude and geographic variation of the radiocarbon content in Antarctic marine life: Implications for reservoir corrections in radiocarbon dating. *Quat. Sci. Rev.* 11, 697–708. doi:10.1016/0277-3791(92)90078-m

Guglielmin, M., Convey, P., Malfasi, F., and Cannone, N. (2016). Glacial fluctuations since the 'medieval Warm Period' at rothera point (Western antarctic peninsula). *Holocene* 26, 154–158. doi:10.1177/0959683615596827

Gunn, D. E., and Best, A. I. (1998). A new automated nondestructive system for high resolution multi-sensor core logging of open sediment cores. *Geo-Marine Lett.* 18, 70–77. doi:10.1007/s003670050054

Hall, B. L. (2003). An overview of late pleistocene glaciation in the South Shetland islands. *Hist. Paleoenviron. Perspect.* 79, 103–113. doi:10.1029/AR079p0103

Hall, B. L. (2010). Holocene relative sea-level changes and ice fluctuations in the South Shetland Islands. *Glob. Planet. Change* 74, 15–26. doi:10.1016/j.gloplacha.2010.07.007

Hall, B. L. (2007). Late-holocene advance of the collins ice cap, king George island, South Shetland islands. *Holocene* 17, 1253–1258. doi:10.1177/0959683607085132

Hambrey, M. J., Davies, B. J., Glasser, N. F., Holt, T. O., Smellie, J. L., and Carrivick, J. L. (2015). Structure and sedimentology of George VI ice shelf, antarctic peninsula: Implications for ice-sheet dynamics and landform development. *J. Geol. Soc.* 172, 599–613. doi:10.1144/jgs2014-134

Hambrey, M. J., and Glasser, N. F. (2012). Discriminating glacier thermal and dynamic regimes in the sedimentary record. *Sediment. Geol.* 251, 1–33. doi:10.1016/j.sedgeo.2012.01.008

Hambrey, M. J., and McKelvey, B. (2000). Major neogene fluctuations of the East Antarctic ice sheet: Stratigraphic evidence from the lambert glacier region. *Geol.* 28, 887–890. doi:10.1130/0091-7613(2000)28<887:mnfote>2.0.co;2

Haslett, J., and Parnell, A. (2008). A simple monotone process with application to radiocarbon-dated depth chronologies. *J. R. Stat. Soc. Ser. C Appl. Statistics)* 57, 399–418. doi:10.1111/j.1467-9876.2008.00623.x

Hass, H. C., Kuhn, G., Monien, P., Brumsack, H. J., and Forwick, M. (2010). Climate fluctuations during the past two millennia as recorded in sediments from Maxwell Bay, South Shetland islands, west Antarctica. *Geol. Soc. Lond. Spec. Publ.* 344, 243–260. doi:10.1144/sp344.17

Heaton, T. J., Köhler, P., Butzin, M., Bard, E., Reimer, R. W., Austin, W. E. N., et al. (2020). Marine20—the marine radiocarbon age calibration curve (0–55, 000 cal BP). *Radiocarbon* 62, 779–820. doi:10.1017/rdc.2020.68

Heaton, T. J., Bard, E., Bronk Ramsey, C., Butzin, M., Hatté, C., Hughen, K. A., et al. (2022). A response to community questions on the Marine20 radiocarbon age calibration curve: Marine reservoir ages and the calibration of 14C samples from the oceans. *Radiocarbon*, 1–27. doi:10.1017/RDC.2022.66

Henkel, S., Kasten, S., Hartmann, J. F., Silva-Busso, A., and Staubwasser, M. (2018). Iron cycling and stable Fe isotope fractionation in Antarctic shelf sediments, King George Island. *Geochimica Cosmochimica Acta* 237, 320–338. doi:10.1016/j.gca.2018.06.042

Henkel, S., Kasten, S., Sala, H., Busso, A. S., and Staubwasser, M. (2013). Effect of increased glacier melt on diagenetic Fe cycling in marine sediments at King George Island (Antarctica). *Mineral. Mag. - H. Goldschmidt Abstr.* 77, 1287.

Heredia Barión, P., Lindhorst, S., Schutter, I., Falk, U., and Kuhn, G. (2019). Reaction of a polar gravel-spit system to atmospheric warming and glacier retreat as reflected by morphology and internal sediment geometries (South Shetland Islands, Antarctica). *Earth Surf. Process. Landforms* 44 (5), 1148–1162. doi:10.1002/esp.4565

Heroy, D. C., Sjunneskog, C., and Anderson, J. B. (2008). Holocene climate change in the Bransfield Basin, antarctic peninsula: Evidence from sediment and diatom analysis. *Antarct. Sci.* 20, 69–87. doi:10.1017/s0954102007000788

Hochschild, V. (1995). *Geomorphologische Kartierung und Untersuchung der Auftaudynamik mit ERS-1-SAR-Daten im Bereich der Antarktischen Halbinsel*. Bremen: Universität Bremen: Vertrieb, Universitätsbuchhandlung Bremen.

Hodgson, D. A., Roberts, S. J., Smith, J. A., Verleyen, E., Sterken, M., Labarque, M., et al. (2013). Late Quaternary environmental changes in Marguerite Bay, Antarctic Peninsula, inferred from lake sediments and raised beaches. *Quat. Sci. Rev.* 68, 216–236. doi:10.1016/j.quascirev.2013.02.002

Hogg, A. G., Heaton, T. J., Hua, Q., Palmer, J. G., Turney, C. S. M., Southon, J., et al. (2020). SHCal20 southern Hemisphere calibration, 0–55, 000 Years cal BP. *Radiocarbon* 62, 759–778. doi:10.1017/rdc.2020.59

Hu, Q-H., Sun, L-G., Xie, Z-Q., Emslie, S. D., and Liu, X. D. (2013). Increase in penguin populations during the little ice age in the Ross sea, Antarctica. *Sci. Rep.* 3, 2472. doi:10.1038/srep02472

Hua, Q., Barbetti, M., and Rakowski, A. Z. (2013). Atmospheric radiocarbon for the period 1950-2010. *Radiocarbon* 55, 2059–2072. doi:10.2458/azu_js_rc.v55i2.16177

Hughes, P. D., Gibbard, P. L., and Ehlers, J. (2013). Timing of glaciation during the last glacial cycle: Evaluating the concept of a global 'last glacial maximum' (LGM). *Earth-Science Rev.* 125, 171–198. doi:10.1016/j.earscirev.2013.07.003

Ingólfsson, Ó., Hjort, C., and Humlum, O. (2003). Glacial and climate history of the antarctic peninsula since the last glacial maximum. *Arct. Antarct. Alp. Res.* 35, 175–186. doi:10.1657/1523-0430(2003)035[0175:gachot]2.0.co;2

Jeong, G. Y. (2006). Radiocarbon ages of sorted circles on king George island, South Shetland islands, west Antarctica. *Antartic. Sci.* 18, 265–270. doi:10.1017/s0954102006000307

Jerosch, K., Pehlke, H., Monien, P., Scharf, F., Weber, L., Kuhn, G., et al. (2018). Benthic meltwater fjord habitats formed by rapid glacier recession on King George Island, Antarctica. *Phil. Trans. R. Soc. A* 376, 20170178. doi:10.1098/rsta.2017.0178

John, B. S., and Sugden, D. E. (1971). Raised marine features and phases of glaciation in the South Shetland Islands. *Br. Antarct. Surv. Bull.* 24, 45–111.

Johnson, J. S., Venturelli, R. A., Balco, G., Allen, C. S., Braddock, S., Campbell, S., et al. (2022). Review article: Existing and potential evidence for Holocene grounding line retreat and readvance in Antarctica. *Cryosphere* 16, 1543–1562. doi:10.5194/tc-16-1543-2022

Juggins, S. (2007). *C2 Version 1.5 User Guide. Software for ecological and palaeoecological data analysis and visualisation*. Newcastle UK: Newcastle University.

Juggins, S. (2012) Rioja: Analysis of quaternary science data, R package version .

Kääb, A. (2007). "Rock glaciers and protalus forms," in *Encyclopedia of Quaternary Science*. Editor S. Elias (Amsterdam : Elsevier), 2236–2242.

Kaplan, M. R., Strelin, J. A., Schaefer, J. M., Peltier, C., Martini, M., Flores, E., et al. (2020). Holocene glacier behavior around the northern Antarctic Peninsula and possible causes. *Earth Planet. Sci. Lett.* 534, 116077. doi:10.1016/j.epsl.2020.116077

Kaplan, M. R., Schaefer, J. M., Strelin, J. A., Denton, G. H., Anderson, R. F., Vandergoes, M. J., et al. (2016). Patagonian and southern South atlantic view of Holocene climate. *Quat. Sci. Rev.* 141, 112–125. doi:10.1016/j.quascirev.2016.03.014

Kaufman, D., McKay, N., Routson, C., Erb, M., Datwyler, C., Sommer, P. S., et al. (2020). Holocene global mean surface temperature, a multi-method reconstruction approach. *Sci. Data* 7, 201. doi:10.1038/s41597-020-0530-7

Kejna, M., Araźny, A., and Sobota, I. (2013). Climatic change on king George island in the years 1948–2011. *Pol. Polar Res.* 34, 213–235. doi:10.2478/popore-2013-0004

Klages, J. P., Kuhn, G., Hillenbrand, C. D., Graham, A., Smith, J., Larter, R., et al. (2013). First geomorphological record and glacial history of an inter-ice stream ridge on the West Antarctic continental shelf. *Quat. Sci. Rev.* 61, 47–61. doi:10.1016/j.quascirev.2012.11.007

Kraus, S., and del Valle, R. (2008a). "Geology, tectonics and Ar–Ar ages of the magmatic dykes from potter peninsula (king George island, South Shetland islands)," in *The antarctic ecosystem of potter cove, King– George island (isla 25 de Mayo): Synopsis of research performed*. C. Wiencke, G. A. Ferreyra, D. Abele, et al. (Bremerhaven, Germany: Alfred Wegener Institut für Polar- und Meeresforschung), 20–30.

Kraus, S., and del Valle, R. (2008b). *Geological map of potter peninsula (king George island, South Shetland islands, antarctic peninsula)*. Buenos Aires, Argentina: Instituto Antártico Chileno, Punta Arenas, Chile & Instituto Antártico Argentino.

Kylander, M. E., Ampel, L., Wohlfarth, B., and Veres, D. (2011). High-resolution X-ray fluorescence core scanning analysis of les echets (France) sedimentary sequence: New insights from chemical proxies. *J. Quat. Sci.* 26, 109–117. doi:10.1002/jqs.1438

Lal, D. (1991). Cosmic ray labeling of erosion surfaces: *In situ* nuclide production rates and erosion models. *Earth Planet. Sci. Lett.* 104, 424–439. doi:10.1016/0012-821x(91)90220-c

Lamy, F., Kilian, R., Arz, H. W., Francois, J. P., Kaiser, J., Prange, M., et al. (2010). Holocene changes in the position and intensity of the southern westerly wind belt. *Nat. Geosci.* 3, 695–699. doi:10.1038/ngeo959

Laskar, J., Robutel, P., Joutel, F., Gastineau, M., Correia, A. C. M., and Levrard, B. (2004). A long-term numerical solution for the insolation quantities of the Earth. *A&A* 428, 261–285. doi:10.1051/0004-6361:20041335

Leavitt, P. R., and Hodgson, D. A. (2001). "Sedimentary pigments," in *Tracking environmental change using lake sediments: Terrestrial, algal, and siliceous indicators*. J. P. Smol, H. J. B. Birks, W. M. Last, et al. (Dordrecht: Springer Netherlands), 295–325.

Lifton, N., Sato, T., and Dunai, T. J. (2014). Scaling *in situ* cosmogenic nuclide production rates using analytical approximations to atmospheric cosmic-ray fluxes. *Earth Planet. Sci. Lett.* 386, 149–160. doi:10.1016/j.epsl.2013.10.052

Lindhorst, S., and Schutter, I. (2014). Polar gravel beach-ridge systems: Sedimentary architecture, Genesis, and implications for climate reconstructions (South Shetland Islands/Western Antarctic Peninsula). *Geomorphology* 221, 187–203. doi:10.1016/j.geomorph.2014.06.013

Liu, X. D., Sun, L. G., Xie, Z. Q., Yin, X., and Wang, Y. (2005). A 1300-year record of penguin populations at Ardley Island in the Antarctic, as deduced from the geochemical data in the ornithogenic lake sediments. *Arct. Antarct. Alp. Res.* 37, 490–498. doi:10.1657/1523-0430(2005)037[0490:ayropp]2.0.co;2

López-Martínez, J., Serrano, E., Schmid, T., Mink, S., and Lines, C. (2012). Periglacial processes and landforms in the South Shetland islands (northern antarctic peninsula region). *Geomorphology* 155–156, 62–79. doi:10.1016/j.geomorph.2011.12.018

Lukas, S. (2011). "Ice-cored moraines," in *Encyclopedia of snow, ice and glaciers*. Editors V. P. Singh, P. Singh, and U. K. Haritashya (Dordrecht: Springer Netherlands), 616–619.

Majewski, W., Wellner, J. S., Szczuciński, W., and Anderson, J. B. (2012). Holocene oceanographic and glacial changes recorded in Maxwell Bay, West Antarctica. *Mar. Geol.* 326–328, 67–79. doi:10.1016/j.margeo.2012.08.009

Makri, S., Rey, F., Gobet, E., Gilli, A., Tinner, W., and Grosjean, M. (2020). Early human impact in a 15, 000-year high-resolution hyperspectral imaging record of paleoproduction and anoxia from a varved lake in Switzerland. *Quat. Sci. Rev.* 239, 106335. doi:10.1016/j.quascirev.2020.106335

Mann, M. E., Zhang, Z., Rutherford, S., Bradley, R. S., Hughes, M. K., Shindell, D., et al. (2009). Global signatures and dynamical origins of the little ice age and medieval climate anomaly. *Science* 326, 1256–1260. doi:10.1126/science.1177303

Marrero, S. M., Phillips, F. M., Borchers, B., Lifton, N., Aumer, R., and Balco, G. (2016). Cosmogenic nuclide systematics and the CRONUScalc program. *Quat. Geochronol.* 31, 160–187. doi:10.1016/j.quageo.2015.09.005

Marshall, G. J., Thompson, D. W. J., and van den Broeke, M. R. (2017). The signature of southern Hemisphere atmospheric circulation patterns in antarctic precipitation. *Geophys. Res. Lett.* 44, 11580–11589. doi:10.1002/2017gl075998

Marshall, G. J. (2007). Half-century seasonal relationships between the Southern Annular mode and Antarctic temperatures. *Int. J. Climatol.* 27, 373–383. doi:10.1002/joc.1407

Matsuoka, N. (2001). Solifluction rates, processes and landforms: A global review. *Earth-Science Rev.* 55, 107–134. doi:10.1016/s0012-8252(01)00057-5

Mäusbacher, R., Müller, J., and Schmidt, R. (1989). Evolution of postglacial sedimentation in antarctic lakes (king George island). *zfg.* 33, 219–234. doi:10.1127/zfg/33/1989/219

Mercer, J. H. (1961). The response of fjord glaciers to changes in the firn limit. *J. Glaciol.* 3, 850–858. doi:10.1017/s0022143000027222

Meredith, M. P., and King, J. C. (2005). Rapid climate change in the ocean west of the Antarctic Peninsula during the second half of the 20th century. *Geophys. Res. Lett.* 32, L19604. doi:10.1029/2005gl024042

Milliken, K. T., Anderson, J. B., Wellner, J. S., Bohaty, S., and Manley, P. (2009). High-resolution Holocene climate record from Maxwell Bay, South Shetland islands, Antarctica. *Geol. Soc. Am. Bull.* 121, 1711–1725. doi:10.1130/b26478.1

Monien, D., Monien, P., Brünjes, R., Widmer, T., Kappenberg, A., Silva Busso, A. A., et al. (2017). Meltwater as a source of potentially bioavailable iron to Antarctica waters. *Antarct. Sci.* 29, 277–291. doi:10.1017/s095410201600064x

Monien, P., Schnetger, B., Brumsack, H-J., Hass, H. C., and Kuhn, G. (2011). A geochemical record of late Holocene palaeoenvironmental changes at King George

Island (maritime Antarctica). *Antartic. Sci.* 23, 255–267. doi:10.1017/s095410201100006x

Moreno, P. I., Vilanova, I., Villa-Martínez, R., Dunbar, R. B., Mucciarone, D. A., Kaplan, M. R., et al. (2018). Onset and evolution of southern annular mode-like changes at centennial timescale. *Sci. Rep.* 8, 3458. doi:10.1038/s41598-018-21836-6

Mulvaney, R., Abram, N. J., Hindmarsh, R. C. A., Arrowsmith, C., Fleet, L., Triest, J., et al. (2012). Recent Antarctic Peninsula warming relative to Holocene climate and ice-shelf history. *Nature* 489, 141–144. doi:10.1038/nature11391

Munoz, Y. P., and Wellner, J. S. (2018). Seafloor geomorphology of Western antarctic peninsula bays: A signature of ice flow behaviour. *Cryosphere* 12, 205–225. doi:10.5194/tc-12-205-2018

Nývlt, D., Glasser, N. F., Hocking, E., Oliva, M., Roberts, S. J., Roman, M., et al. (2020). "Chapter 5 - Tracing the deglaciation since the Last Glacial Maximum," in *Past Antarctica*. Editors M. Oliva and J. Ruiz-Fernández (Academic Press), 89–107.

Ó Cofaigh, C., Davies, B. J., Livingstone, S. J., Smith, J. A., Johnson, J. S., Hocking, E. P., et al. (2014). Reconstruction of ice-sheet changes in the antarctic peninsula since the last glacial maximum. *Quat. Sci. Rev.* 100, 87–110. doi:10.1016/j.quascirev.2014.06.023

Oksanen, J. (2014). Vegan: Community ecology package. R package version 2.3-0. http://cran.r-project.org/web/packages/vegan/index.html.

Oliva, M., Antoniades, D., Giralt, S., Granados, I., Pla Rabes, S., Toro, M., et al. (2016a). La deglaciación de las áreas libres de hielo de las islas Shetland del Sur (Antártida). Ejemplos de Byers (Livingston) y Barton (King George). *CyG.* 14, 105–118. doi:10.17735/cyg.v30i1-2.48665

Oliva, M., Antoniades, D., Giralt, S., Granados, I., Pla-Rabes, S., Toro, M., et al. (2016b). The Holocene deglaciation of the Byers Peninsula (Livingston Island, Antarctica) based on the dating of lake sedimentary records. *Geomorphology* 261, 89–102. doi:10.1016/j.geomorph.2016.02.029

Oliva, M., Antoniades, D., Serrano, E., Giralt, S., Liu, E. J., Granados, I., et al. (2019). The deglaciation of Barton peninsula (king George island, South Shetland islands, Antarctica) based on geomorphological evidence and lacustrine records. *Polar Rec.* 55, 177–188. doi:10.1017/s0032247419000469

Oliva, M., Mercier, D., Ruiz-Fernández, J., and McColl, S. (2020). Paraglacial processes in recently deglaciated environments. *Land Degrad. Dev.* 31, 1871–1876. doi:10.1002/ldr.3283

Oliva, M., Navarro, F., Hrbáček, F., Hernandez, A., Nyvlt, D., Pereira, P., et al. (2017). Recent regional climate cooling on the Antarctic Peninsula and associated impacts on the cryosphere. *Sci. Total Environ.* 580, 210–223. doi:10.1016/j.scitotenv.2016.12.030

Oliva, M., and Ruiz-Fernández, J. (2017). Geomorphological processes and frozen ground conditions in elephant point (Livingston island, South Shetland islands, Antarctica). *Geomorphology* 293, 368–379. doi:10.1016/j.geomorph.2016.01.020

Osmanoğlu, B., Braun, M., Hock, R., and Navarro, F. (2013). Surface velocity and ice discharge of the ice cap on King George Island, Antarctica. *Ann. Glaciol.* 54, 111–119. doi:10.3189/2013aog63a517

Palacios, D., Ruiz-Fernández, J., Oliva, M., Andrés, N., Fernández-Fernández, J. M., Schimmelpfennig, I., et al. (2020). Timing of formation of neoglacial landforms in the South Shetland islands (antarctic peninsula): Regional and global implications. *Quat. Sci. Rev.* 234, 106248. doi:10.1016/j.quascirev.2020.106248

Pallàs, R., James, T., Sàbat, F., Vilaplana, J., Grant, D., and Ricci, C. (1997). "Holocene uplift in the South Shetland islands: Evaluation of tectonics and glacio-isostasy," in *The antarctic region: Geological evolution and processes*. Editor C. Ricci (Siena, Italy: Terra Antarctica Publication). 861–868.

Parnell, A. C. (2021). Bchron: Radiocarbon dating, age-depth modelling, relative sea level rate estimation, and non-parametric phase modelling. https://github.com/andrewcparnell/Bchron/.

Pasotti, F., Manini, E., Giovannelli, D., Wolfl, A., Monien, D., Verleyen, E., et al. (2015a). Antarctic shallow water benthos in an area of recent rapid glacier retreat. *Mar. Ecol.* 36, 716–733. doi:10.1111/maec.12179

Pasotti, F., Saravia, L. A., De Troch, M., Tarantelli, M. S., Sahade, R., and Vanreusel, A. (2015b). Benthic trophic interactions in an antarctic shallow water ecosystem affected by recent Glacier Retreat. *PLoS ONE* 10, e0141742. doi:10.1371/journal.pone.0141742

Pearson, E. J., Juggins, S., Talbot, H. M., Weckström, J., Rosén, P., Ryves, D. B., et al. (2011). A lacustrine GDGT-temperature calibration from the Scandinavian Arctic to Antarctic: Renewed potential for the application of GDGT-paleothermometry in lakes. *Geochimica Cosmochimica Acta* 75, 6225–6238. doi:10.1016/j.gca.2011.07.042

Peck, V. L., Allen, C. S., Kender, S., McClymont, E. L., and Hodgson, D. A. (2015). Oceanographic variability on the West Antarctic Peninsula during the Holocene and the influence of upper circumpolar deep water. *Quat. Sci. Rev.* 119, 54–65. doi:10.1016/j.quascirev.2015.04.002

Perren, B., Hodgson, D. A., Roberts, S. J., Sime, L., Van Nieuwenhuyze, W., Verleyen, E., et al. (2020). Southward migration of the Southern Hemisphere westerly winds corresponds with warming climate over centennial timescales. *Commun. Earth Environ.* 1 (1), 58. doi:10.1038/s43247-020-00059-6

Quade, J., and Kaplan, M. R. (2017). Lake-level stratigraphy and geochronology revisited at lago (lake) cardiel, Argentina, and changes in the southern hemispheric westerlies over the last 25 ka. *Quat. Sci. Rev.* 177, 173–188. doi:10.1016/j.quascirev.2017.10.006

Quartino, M. L., Deregibus, D., Campana, G. L., Latorre, G. E. J., and Momo, F. R. (2013). Evidence of macroalgal colonization on newly ice-free areas following glacial retreat in Potter Cove (South Shetland Islands), Antarctica. *PLoS ONE* 8, e58223. doi:10.1371/journal.pone.0058223

Reimer, R. W., and Reimer, P. J. (2004). *CALIBomb - calibration of post-bomb C-14 data*. www.calib.org.

Rein, B., and Sirocko, F. (2002). *In-situ* reflectance spectroscopy – analysing techniques for high-resolution pigment logging in sediment cores. *Int. J. Earth Sci.* 91, 950–954. doi:10.1007/s00531-002-0264-0

Reynhout, S. A., Sagredo, E. A., Kaplan, M. R., Aravena, J. C., Martini, M. A., Moreno, P. I., et al. (2019). Holocene glacier fluctuations in Patagonia are modulated by summer insolation intensity and paced by Southern Annular Mode-like variability. *Quat. Sci. Rev.* 220, 178–187. doi:10.1016/j.quascirev.2019.05.029

Roberts, S. J., Hodgson, D. A., Shelley, S., Royles, J., Griffiths, H. J., Deen, T. J., et al. (2010). Establishing lichenometric ages for nineteenth- and twentieth-century glacier fluctuations on south Georgia (south atlantic). *Geogr. Ann. Ser. A Phys. Geogr.* 92A, 125–139. doi:10.1111/j.1468-0459.2010.00382.x

Roberts, S. J., Hodgson, D. A., Sterken, M., Whitehouse, P. L., Verleyen, E., Vyverman, W., et al. (2011). Geological constraints on glacio-isostatic adjustment models of relative sea-level change during deglaciation of Prince Gustav Channel, Antarctic Peninsula. *Quat. Sci. Rev.* 30, 3603–3617. doi:10.1016/j.quascirev.2011.09.009

Roberts, S. J., McCulloch, R. D., Emmings, J. F., Davies, S. J., Van Nieuwenhuyze, W., Sterken, M., et al. (2022). Late glacial and Holocene palaeolake history of the última esperanza region of southern Patagonia. *Front. Earth Sci.* 10. doi:10.3389/feart.2022.813396

Roberts, S. J., Monien, P., Foster, L. C., Loftfield, J., Hocking, E. P., Schnetger, B., et al. (2017). Author Correction: Past penguin colony responses to explosive volcanism on the Antarctic Peninsula. *Nat. Commun.* 8, 3266. doi:10.1038/s41467-022-30657-1

Rückamp, M., Blindow, N., Suckro, S., Braun, M., and Humbert, A. (2010). Dynamics of the ice cap on king George island, Antarctica: Field measurements and numerical simulations. *Ann. Glaciol.* 51, 80–90. doi:10.3189/172756410791392817

Rückamp, M., Braun, M., Suckro, S., and Blindow, N. (2011). Observed glacial changes on the King George Island ice cap, Antarctica, in the last decade. *Glob. Planet. Change* 79, 99–109. doi:10.1016/j.gloplacha.2011.06.009

Ruiz-Fernández, J., Oliva, M., Nývlt, D., Cannone, N., García-Hernández, C., Guglielmin, M., et al. (2019). Patterns of spatio-temporal paraglacial response in the Antarctic Peninsula region and associated ecological implications. *Earth-Science Rev.* 192, 379–402. doi:10.1016/j.earscirev.2019.03.014

Sahade, R., Lagger, C., Torre, L., Momo, F., Monien, P., Schloss, I., et al. (2015). Climate change and glacier retreat drive shifts in an Antarctic benthic ecosystem. *Sci. Adv.* 1, e1500050. doi:10.1126/sciadv.1500050

Sánchez-Lugo, A., Morice, C., Berrisford, P., and Argüez, A. (2018). "Global surface temperatures,". Editors J. Blunden, D. S. Arndt, and G. Hartfield, 99, 11–13.*State Clim. 2017. Bull. Am. Meteorological Soc.*8

Saunders, K. M., Roberts, S. J., Perren, B., Butz, C., Sime, L., Davies, S., et al. (2018). Holocene dynamics of the Southern Hemisphere westerly winds and possible links to CO2 outgassing. *Nat. Geosci.* 11, 650–655. doi:10.1038/s41561-018-0186-5

Schneider, T., Rimer, D., Butz, C., and Grosjean, M. (2018). A high-resolution pigment and productivity record from the varved ponte tresa basin (lake lugano, Switzerland) since 1919: Insight from an approach that combines hyperspectral imaging and high-performance liquid chromatography. *J. Paleolimnol.* 60, 381–398. doi:10.1007/s10933-018-0028-x

Seong, Y. B., Owen, L. A., Lim, H. S., Yoon, H. I., Kim, Y., Lee, Y. I., et al. (2008). Rate of late quaternary ice-cap thinning on king George island, South Shetland islands, west Antarctica defined by cosmogenic 36Cl surface exposure dating. *Boreas* 38, 207–213. doi:10.1111/j.1502-3885.2008.00069.x

Serrano, E., Giner, J., Gumiel, P., López-Martínez, J., et al. (2012). El glaciar rocoso de Hurd: Estructura e inserción en el sistema de transferencia de derrubios

Antártico Marítimo (Isla Livington, Islas Shetland de Sur, Antártida. *Cuaternario Geomorfol.* 18, 13–25.

Serrano, E., and López-Martınez, J. (2000). Rock glaciers in the South Shetland Islands, Western Antarctica. *Geomorphology* 35, 145–162. doi:10.1016/s0169-555x(00)00034-9

Shevenell, A. E., Ingalls, A. E., Domack, E. W., and Kelly, C. (2011). Holocene Southern Ocean surface temperature variability west of the antarctic peninsula. *Nature* 470, 250–254. doi:10.1038/nature09751

Simms, A. R., Bentley, M. J., Simkins, L. M., Zurbuchen, J., Reynolds, L. C., DeWitt, R., et al. (2021). Evidence for a "little ice age" glacial advance within the antarctic peninsula – examples from glacially-overrun raised beaches. *Quat. Sci. Rev.* 271, 107195. doi:10.1016/j.quascirev.2021.107195

Simms, A. R., Ivins, E. R., DeWitt, R., Kouremenos, P., and Simkins, L. M. (2012). Timing of the most recent neoglacial advance and retreat in the South Shetland islands, antarctic peninsula: Insights from raised beaches and Holocene uplift rates. *Quat. Sci. Rev.* 47, 41–55. doi:10.1016/j.quascirev.2012.05.013

Simms, A. R., Milliken, K. T., Anderson, J. B., and Wellner, J. S. (2011). The marine record of deglaciation of the South Shetland islands, Antarctica since the last glacial maximum. *Quat. Sci. Rev.* 30, 1583–1601. doi:10.1016/j.quascirev.2011.03.018

Smellie, J. L., Pankhurst, R., Thomson, M. R. A, and Davies, R. E. S. (1984). The geology of the South Shetland islands: VI. *Stratigr. Geochem. Evol. Br. Antarct. Surv.* 87.

Spada, G., Bamber, J. L., and Hurkmans, R. T. W. L. (2013). The gravitationally consistent sea-level fingerprint of future terrestrial ice loss. *Geophys. Res. Lett.* 40, 482–486. doi:10.1029/2012gl053000

Steig, E. J., Schneider, D. P., Rutherford, S. D., Mann, M. E., Comiso, J. C., and Shindell, D. T. (2009). Warming of the antarctic ice-sheet surface since the 1957 international geophysical year. *Nature* 457, 459–462. doi:10.1038/nature07669

Steinhilber, F., Beer, J., and Fröhlich, C. (2009). Total solar irradiance during the Holocene. *Geophys. Res. Lett.* 36, L19704. doi:10.1029/2009gl040142

Stewart, T. G., Anderson, J. B., and Ashley, G. M. (1991) Glacial marine sedimentation from tidewater glaciers in the Canadian High Arctic, *Glacial marine sedimentation: paleoclimatic significance. Geological Society of America, Special Papers*, 261: 95, 106, doi:10.1130/SPE261-p95

Stone, J. O. (2000). Air pressure and cosmogenic isotope production. *J. Geophys. Res.* 105, 23753–23759. doi:10.1029/2000jb900181

Strelin, J. A., Heredia Barión, P. A., Martini, M. A., Kaplan, M. M., and Kuhn, G. (2014). "The age of the first Holocene marine transgression in potter cove, isla 25 de Mayo (king George island), South Shetland islands," in *Contributions to the XIX congreso geológico Argentino martino RD. T1-51.* Editors R. Lira, A. Guereschi, E. Baldo, J. Franzese, D. Krohling, M. Manassero, et al. (Argentina: Córdoba), 455–459.

Strelin, J. A., Sone, T., Mori, J., Torielli, C. A., and Nakamura, T. (2006). "New data related to Holocene landform development and climatic change from James Ross island, antarctic peninsula," in *Antarctica: Contributions to global Earth sciences*. D. K. Fütterer, D. Damaske, G. Kleinschmidt, et al. (Berlin, Heidelberg: Springer Berlin Heidelberg), 455–459.

Strother, S. L., Salzmann, U., Roberts, S. J., Hodgson, D. A., Woodward, J., Van Nieuwenhuyze, W., et al. (2015). Changes in Holocene climate and the intensity of Southern Hemisphere Westerly Winds based on a high-resolution palynological record from sub-Antarctic South Georgia. *Holocene* 25, 263–279. doi:10.1177/0959683614557576

Sugden, D. E., and John, B. S. (1973). "The ages of glacier fluctuations in the South Shetland Islands, Antarctica," in *Palaeoecology of africa, the surrounding islands and Antarctica*. Editors van Zinderen and E. M. Bakker (Cape Town: Balkema), 141–159.

Sun, L. G., Liu, X. D., Yin, X. B., Xie, Z., and Zhao, J. (2005). Sediments in palaeo-notches: Potential proxy records for palaeoclimatic changes in Antarctica. *Palaeogeogr. Palaeoclimatol. Palaeoecol.* 218, 175–193. doi:10.1016/j.palaeo.2004.12.009

Thomas, E. R., Marshall, G. J., and McConnell, J. R. (2008). A doubling in snow accumulation in the Western Antarctic Peninsula since 1850. *Geophys. Res. Lett.* 35, L01706. doi:10.1029/2007GL032529

Toro, M., Granados, I., Pla, S., Giralt, S., Antoniades, D., Galán, L., et al. (2013). Chronostratigraphy of the sedimentary record of limnopolar lake, Byers peninsula, Livingston island, Antarctica. *Antarct. Sci.* 25, 198–212. doi:10.1017/s0954102012000788

Turner, J., Lachlan-Cope, T. A., Marshall, G. J., Morris, E. M., Mulvaney, R., and Winter, W. (2002). Spatial variability of Antarctic Peninsula net surface mass balance. *J. Geophys. Res.* 107, 4173. doi:10.1029/2001jd000755

Turner, J., Lu, H., White, I., King, J. C., Phillips, T., Hosking, J. S., et al. (2016). Absence of 21st century warming on Antarctic Peninsula consistent with natural variability. *Nature* 535, 411–415. doi:10.1038/nature18645

van der Bilt, W. G. M., Bakke, J., Werner, J. P., Paasche, O., Rosqvist, G., and Vatle, S. S. (2017). Late Holocene glacier reconstruction reveals retreat behind present limits and two-stage Little Ice Age on subantarctic South Georgia. *J. Quat. Sci.* 32, 888–901. doi:10.1002/jqs.2937

van der Veen, C. J. (1995). *Controls on calving rate and basal sliding: Observations from columbia glacier, Alaska, prior to and during its rapid retreat, 1976–1993*. Columbus USA: Byrd Polar Research Center Report 11.

Varma, V., Prange, M., Spangehl, T., Lamy, F., Cubasch, U., and Schulz, M. (2012). Impact of solar-induced stratospheric ozone decline on southern Hemisphere westerlies during the late maunder minimum. *Geophys. Res. Lett.* 39, L20704. doi:10.1029/2012gl053403

Vaughan, D. G., Comiso, J. C., Allison, I., Carrasco, J., Kaser, G., Kwok, R., et al. (2013). "Observations: Cryosphere,". T. F. Stocker, D. Qin, G-K. Plattner, et al. (Cambridge, United Kingdom and New York, NY, USA: Cambridge University Press), 317–382.*Climate change 2013: The physical science basis. Contribution of working group I to the fifth assessment report of the intergovernmental panel on climate change*.

Vaughan, D. G., Marshall, G. J., Connolley, W. M., Parkinson, C., Mulvaney, R., Hodgson, D. A., et al. (2003). Recent rapid regional climate warming on the antarctic peninsula. *Clim. Change* 60, 243–274. doi:10.1023/a:1026021217991

Verfaillie, D., Charton, J., Schimmelpfennig, I., Stroebele, Z., Jomelli, V., Betard, F., et al. (2021). Evolution of the Cook Ice Cap (Kerguelen Islands) between the last centuries and 2100 ce based on cosmogenic dating and glacio-climatic modelling. *Antarct. Sci.* 33, 301–317. doi:10.1017/s0954102021000080

Wang, G., and Cai, W. (2013). Climate-change impact on the 20th-century relationship between the Southern Annular Mode and global mean temperature. *Sci. Rep.* 3, 2039. doi:10.1038/srep02039

Watcham, E. P., Bentley, M. J., Hodgson, D. A., Roberts, S., Fretwell, P., Lloyd, J., et al. (2011). A new Holocene relative sea level curve for the South Shetland Islands, Antarctica. *Quat. Sci. Rev.* 30, 3152–3170. doi:10.1016/j.quascirev.2011.07.021

Weatherall, P., Marks, K. M., Jakobsson, M., Schmitt, T., Tani, S., Arndt, J. E., et al. (2015). A new digital bathymetric model of the world's oceans. *Earth Space Sci.* 2, 331–345. doi:10.1002/2015ea000107

Whitehouse, P. L., Bentley, M. J., and Le Brocq, A. M. (2012a). A deglacial model for Antarctica: Geological constraints and glaciological modelling as a basis for a new model of antarctic glacial isostatic adjustment. *Quat. Sci. Rev.* 32, 1–24. doi:10.1016/j.quascirev.2011.11.016

Whitehouse, P. L., Bentley, M. J., Milne, G. A., King, M. A., and Thomas, I. D. (2012b). A new glacial isostatic adjustment model for Antarctica: Calibrated and tested using observations of relative seasea-level change and present-day uplift rates. *Geophys. J. Int.* 190, 1464–1482. doi:10.1111/j.1365-246x.2012.05557.x

Wichard, T., Mishra, B., Myneni, S. C. B., Bellenger, J. P., and Kraepiel, A. M. L. (2009). Storage and bioavailability of molybdenum in soils increased by organic matter complexation. *Nat. Geosci.* 2, 625–629. doi:10.1038/ngeo589

Wölfl, A. C., Wittenberg, N., Feldens, P., Hass, H. C., Betzler, C., and Kuhn, G. (2016). Submarine landforms related to glacier retreat in a shallow Antarctic fjord. *Antarct. Sci.* 28, 475–486. doi:10.1017/s0954102016000262

Yang, L., Gao, Y., Sun, L., Xie, Z., Yang, W., Chu, Z., et al. (2019). Enhanced westerlies drove penguin movement at 1000 yr BP on Ardley Island, west Antarctic Peninsula. *Quat. Sci. Rev.* 214, 44–53. doi:10.1016/j.quascirev.2019.04.026

Yoon, H. I., Yoo, K-C., Park, B-K., Kim, Y., Khim, B. K., and Kang, C. Y. (2004). The origin of massive diamicton in marian and potter coves, king George island, west Antarctica. *Geosci. J.* 8, 1–10. doi:10.1007/bf02910274

Zervas, D., Nichols, G. J., Hall, R., Smyth, H. R., Luthje, C., and Murtagh, F. (2009). SedLog: A shareware program for drawing graphic logs and log data manipulation. *Comput. Geosciences* 35, 2151–2159. doi:10.1016/j.cageo.2009.02.009